**الجمهورية الجزائرية الديمقراطية الشعبية**
People's Democratic Republic of Algeria
وزارة التعليم العالي و البحث العلمي
Ministry of Higher Education and Scientific Research

**University Mohamed Khider of Biskra**
**Faculty of Sciences and Technology**
**Department**: Mechanical Engineering
Ref :……

جامعة محمد خيضر بسكـرة
كليـة العلـوم و التكنولوجيــا
قسم: الهندسة الميكانيكية
المرجع:……

Thesis submitted for obtaining the degree of

## Doctorate in: Mechanical Engineering

**Specialty (Option): Energetic**

# Effect of the artificial roughness dispositions on the thermal exchanges in a flat solar collector

Presented by:

## BENSACI Charaf Eddine

Thesis defended publicly on: 07/01/2021

## The jury members :

| | | | |
|---|---|---|---|
| **Dr. MOUMMI Noureddine** | **Professor** | **Chairman** | **University of Biskra** |
| **Dr. MOUMMI Abdelhafid** | **Professor** | **Supervisor** | **University of Biskra** |
| **Dr. BRIMA Abdelhafid** | **Professor** | **Examiner** | **University of Batna 1** |
| **Dr. AOUES Kamel** | **Associate Professor** | **Examiner** | **University of Biskra** |
| **Dr. HARNANE Yamina** | **Associate Professor** | **Examiner** | **University of Oum El Bouaghi** |
| **Dr. FRANCISCO J. S. de la Flor** | **Professor** | **Invited** | **University of Cadiz, Spain** |

**الجمهورية الجزائرية الديمقراطية الشعبية**
République Algérienne Démocratique et Populaire
وزارة التعليم العالي و البحث العلمي
Ministère de l'enseignement supérieur et de la recherche scientifique

**Université Mohamed Khider – Biskra**
**Faculté des Sciences et de la technologie**
**Département** : Génie Mécanique
Réf : ……

جامعة محمد خيضر بسكرة
كليـة العلـوم و التكنولوجيــا
قسم: الهندسة الميكانيكية
المرجع:……

Thèse présentée en vue de l'obtention
Du diplôme de

## Doctorat en : Génie Mécanique

**Spécialité (Option) : Energétique**

# Effet de la disposition des rugosités artificielles sur les échanges thermiques dans un capteur solaire plan

Présentée par :

## BENSACI Charaf Eddine

Soutenue publiquement le 07/01/2021

## Devant le jury composé de :

| | | | |
|---|---|---|---|
| **Dr. MOUMMI Noureddine** | **Professeur** | **Président** | **Université de Biskra** |
| **Dr. MOUMMI Abdelhafid** | **Professeur** | **Rapporteur** | **Université de Biskra** |
| **Dr. BRIMA Abdelhafid** | **Professeur** | **Examinateur** | **Université de Batna 1** |
| **Dr. AOUES Kamel** | **Maitre de Conférences 'A'** | **Examinateur** | **Université de Biskra** |
| **Dr. HARNANE Yamina** | **Maitre de Conférences 'A'** | **Examinateur** | **Université de Oum El Bouaghi** |
| **Dr. Francisco J. S. de la Flor** | **Professeur** | **Invité** | **Université de Cadiz, Espagne** |

## ABSTRACT

In this thesis, a numerical and experimental study of different position of the baffles in a solar air heater have been presented in order to improve its thermal and hydraulic performance. The numerical study was performed on four cases corresponding to different placements of baffles, where the experimental model of the solar air heater was designed, manufactured and used for the validation of the numerical model. The CFD simulations have been performed by ANSYS FLUENT 15.0. Based on the obtained results, the new baffle placements show that effective thermo-hydraulic performance is not just a function of the shape or changes in the geometric parameters of the baffles. The correct placement of baffles dramatically improves the thermo-hydraulic performance of solar air heaters. The effect of baffle positions on local convective heat transfer coefficients has been discussed.



**Keywords:** Solar air heater; Baffles; CFD simulation; Local convective heat transfer coefficient; Thermo-hydraulic performance.



## مـلـخص

في هذه الأطروحة ، تم تقديم دراسة عددية وتجريبية لمواضع مختلفة من الحواجز في سخان الهواء الشمسي من أجل تحسين الأداء الحراري والهيدروليكي. أجريت الدراسة العددية على أربع حالات لمواضع مختلفة من الحواجز، حيث تم تصميم و تصنيع النموذج التجريبي لسخان الهواء الشمسي وإستخدامه للتحقق من صحة النموذج العددي. تم إجراء المحاكاة العددية بواسطة ANSYS FLUENT 15.0. بناءً على النتائج المتحصل عليها، تُظهر المواضع الجديدة للحواجز أن الأداء الحراري الهيدروليكي الفعال غير متعلق فقط بشكل أو بتغيير في المعلمات الهندسية للحواجز. يعمل الموضع الصحيح للحواجز على تحسين الأداء الحراري الهيدروليكي لسخانات الهواء الشمسية بشكل كبير. تمت مناقشة تأثير مواضع الحواجز على معاملات إنتقال الحرارة بالحمل الموضعي.



**كلمات مفتاحية:** سخان الهواء الشمسي، حواجز، محاكاة عددية، معامل إنتقال الحرارة بالحمل الحراري، الأداء الحراري الهيدروليكي.

# RESUME

Dans cette thèse, une étude numérique et expérimentale de différentes positions des chicanes dans un capteur solaire plan à air a été présentée pour mettre en évidence l'amélioration de ses performances thermiques et hydrauliques. L'étude numérique a été réalisée sur quatre cas correspondant à différents emplacements de chicanes, où le modèle expérimental de capteur solaire a été conçu, fabriqué et utilisé pour la validation du modèle numérique. Les simulations numériques ont été réalisées par ANSYS FLUENT 15.0. Sur la base des résultats obtenus, les nouveaux emplacements de chicanes montrent que les meilleures performances thermo-hydrauliques ne sont pas seulement fonction de la forme ou des changements des paramètres géométriques des chicanes. Le placement correct des chicanes améliore considérablement les performances thermo-hydrauliques des capteurs solaires. L'effet des positions des chicanes sur les coefficients d'échange convectif locaux a été également discuté.

**Mots clé :** Capteur solaire à air ; chicanes ; simulation numérique ; les coefficients d'échanges convectif local ; performances thermo-hydraulique.

# TABLE OF CONTENTS

# LIST OF FIGURES

# LIST OF TABLES

# NOMENCLATURE

| | |
|---|---|
| $A_{abs}$ | *Absorber plate surface area, $m^2$* |
| $D_H$ | *Hydraulic diameter, m* |
| $f$ | *Friction factor* |
| $h_x$ | *Local convective heat transfer coefficient, $W.m^{-2}.K^{-1}$* |
| $I_T$ | *Solar radiation, $W.m^{-2}$* |
| $L$ | *Length of the air channel, m* |
| $\dot{m}$ | *Mass flow rate, $kg.s^{-1}$* |
| $Nu$ | *Nusselt number* |
| $\dot{Q}$ | *Heat flux, $W.m^{-2}$* |
| $Re$ | *Reynolds number* |
| $T$ | *Temperature, K* |
| $THPF$ | *Thermo-hydraulic performance factor* |
| $U$ | *Velocity, $m.s^{-1}$* |

***Greek symbols***

| | |
|---|---|
| $\Delta P$ | *Pressure drop, Pa* |
| $\Delta T$ | *Temperature difference, K* |
| $\eta_{th}$ | *Thermal efficiency* |
| $v$ | *Kinematic viscosity, $m^2.s^{-1}$* |
| $\rho$ | *Fluid density, $kg.m^{-3}$* |

***Subscripts***

| | |
|---|---|
| *abs* | *Absorber* |
| *bottom* | *Bottom plate* |
| *in* | *Inlet* |
| *out* | *Outlet* |
| *s* | *Smooth* |
| *upper* | *Upper plate* |

***Abbreviation***

| | |
|---|---|
| *SAH* | *Solar air heater* |
| *CFD* | *Computational fluid dynamics* |

# *GENERAL INTRODUCTION*

# GENERAL INTRODUCTION

Energy is a primary need to live our daily life at an expense of some valuable things such as environmental degradation by using fossil fuels. The basic ingredient for sustaining life and development is energy in its different forms. Solar energy is a clean, eco-friendly source of energy that is freely available in the long term. The most efficient and simplest way to benefit from solar energy, with no negative effects, is for collectors to convert it into thermal energy for a variety of applications [1,2].

There is a wide scope for using the available solar energy for thermal applications such as solar drying, crop drying, water heating, building heating and solar cooking. Solar air collectors (SAC) are the most common type of collector due to their enhanced capacity to absorb both diffuse and direct radiation simultaneously, in addition to being easy to maintain, reliable and easy to install in buildings. Where, the efficiency of this system is low because of the low convective heat transfer coefficient between the absorber plate and the flowing air. However, there are many ways to increase this, such as by using air impinging jets, replacing the single duct with double-pass or multipass ones and incorporating baffles.

According to the comprehensive details of research into the optimization of the solar air heaters performance, it is evident that insufficient research has been performed into the placement of baffles on the bottom plate within the air channel of solar air heaters. The current research work includes a 3D numerical simulation based on the experimental tests to evaluate the performance of cases with different baffle positions. Four different cases were analyzed depending on the position of the baffles in the device: in case 1, the baffles were located in the second half of the air channel; in case 2, in the first half of the air channel; in case 3, in the middle of the air channel; and in case 4, throughout the whole air channel.

The experimental model of the solar air heater was designed and manufactured from locally available materials at the technological hall of Mohamed Khider University of Biskra, Algeria. Measurements were taken of the local ambient conditions, the absorber and bottom surface temperatures, the mass flow rate and the temperature at different points of the air channel. In the experimental set-up, the baffles were located in the second half of the air channel, between the middle and the outlet section of the device. Consequently, two different regions can be distinguished: the smooth region without baffles and the region with baffles.

The CFD simulations have been performed by ANSYS FLUENT 15.0 at Reynolds numbers ranging from 2370-8340. The thermo-hydraulic performance, local convective heat transfer coefficient and thermal efficiency estimation of all the cases has been discussed and compared. The flow-diagram of Figure.1 shows the methodology followed in this work.

The main aim of this thesis of these new baffle placements is to be able to prove that effective thermo-hydraulic performance is not just a function of the shape or changes in the geometric parameters of the

baffles, but also that the correct placement of baffles can significantly enhance the thermo-hydraulic performance of solar air heaters. This thesis is structured into four main chapters as follows:

The first chapter is presented a background information and state of the art on solar air heaters starting by the different mechanisms and techniques to improve the performance of the solar air heaters, where the main categories of the artificial roughness to improve the solar air heaters performances are the ribs and the baffles where each category has many classifications based on the shapes, sizes, orientations and arrangements. Further, the parameters of thermohydraulic performance corresponding heat transfer and pressure drop of solar air heaters to evaluate the overall studied system.

The second chapter is presented the experimental study includes the descriptions of experimental model, studied cases, experimental procedure, measurement, the instruments of measurements with its uncertainties and heat transfer calculation. The experimental results performed from May to June 2018 have been presented. Where the examination of five configurations under climatic conditions of Biskra have been compared as well.

The third chapter is presented the numerical methodology which based on the geometry of the experimental test model under defined assumptions and diferent boundary conditions. The geometry creation, mesh generation, solver and turublance model are described. The solving steps have been described under defined assumptions and boundary conditions known. the accuracy of the numerical results are checked, where the suitability of different turbulence models for the present numerical problem is evaluated.

The fourth chapter is presented the comparison of the numerical results with the current experimental results, the numerical results of the heat transfer and hydraulic characteristics of five different cases of solar air heaters, where the effects of the placement of baffles and Reynolds number on heat transfer and hydraulics are obtained in terms of the Nusselt number, local heat transfer coefficient and friction factor are presented, the thermal efficiency is estimated based on the CFD results.

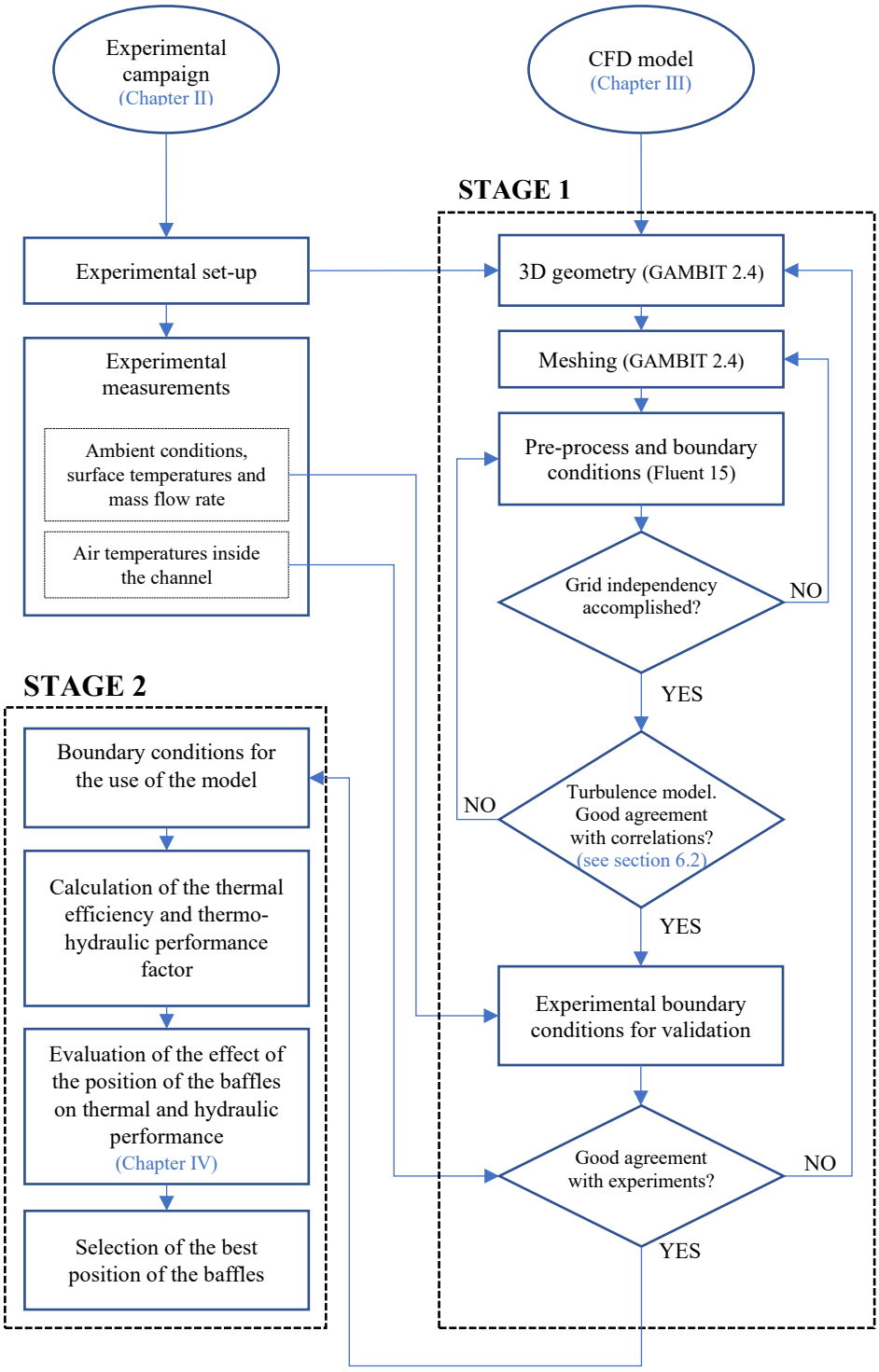


**Figure 1:** Methodology flow-diagram

# *CHAPTER I*

# *BACKGROUND AND LITERATURE REVIEW*

## I.1. INTRODUCTION

The easiest way to benefit solar energy is to convert it into thermal energy by using solar air heaters for applying in a variety of applications like drying of woods, drying of numerous agricultural products like grapes, onion, seeds, marine products, treatment of industrial products, spaces heating, textile and are also used for curing and drying of concrete and building components with reducing the energy consumption costs for the application concerned [1–7].

Solar air heaters have a poor convective coefficient between air flowing and absorber plate and the heat losses, which considered as the main disadvantage and led to lower thermal efficiency. According to the solar air heater performance enhancement, it can be classified into two main families; the first one is based on the air pass number and type of air flowing channel under the absorber plate.

The second is related to the used technology of flat absorber plate design. To improve the convection area and increase airflow turbulence with the blackened plate. Solar air heaters (See Figure I-1) consist mainly of airflow duct and absorber plate. To reduce heat losses from both bottom and sidewalls, thermal insulation with low thermal conductivity is used. The upper side of the heater is covered with a glass cover with low absorptivity and high transmissivity.

Solar air heaters (SAH) are the most common type of collector due to their enhanced capacity to absorb both diffuse and direct radiation simultaneously, in addition to being easy to maintain, reliable and easy to install in buildings.

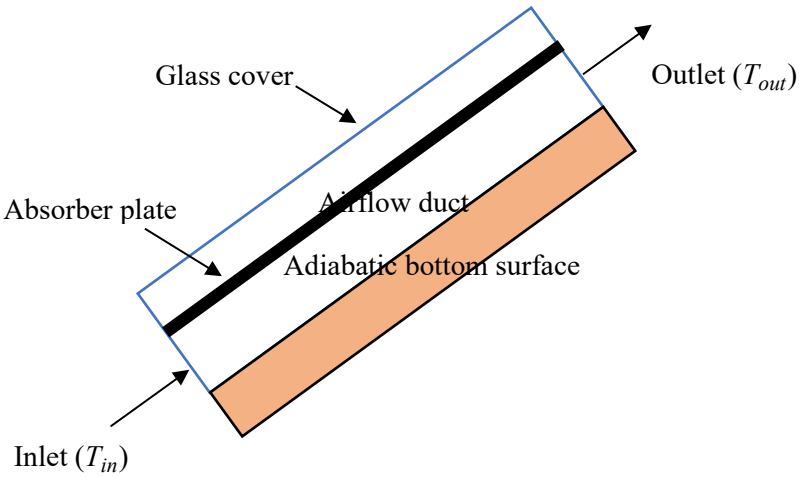


**Figure I-1:** Schematic view of the solar air heater components

However, the efficiency of this system is low because of the low convective heat transfer coefficient between the absorber plate and the flowing air. There are many mechanisms to enhance the heat transfer such as [8]:

- Use of a secondary heat transfer surface.
- Disruption of the laminar sub-layer in the turbulent boundary layer.
- Introducing secondary flows.
- Promoting flow attachment/reattachment.
- Enhancing effective thermal conductivity of the fluid under static or dynamic conditions.
- Delaying the boundary layer development.
- Redistribution of the flow.
- Increasing the difference between the surface and fluid temperatures.
- Increasing the thermal conductivity of the solid phase using special Nanotechnology fabrications.

Also, many techniques to improve heat transfer (See Figure I-2), are divided into three main categories as follow: active, passive, compound [8–10].

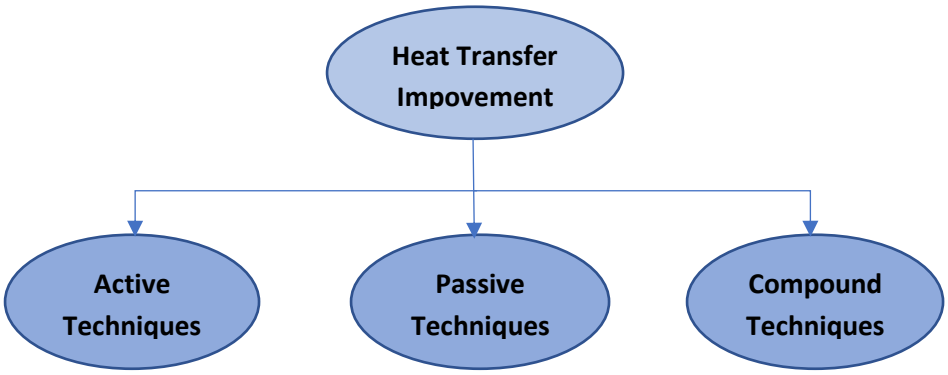


**Figure I-2:**Techniques of heat transfer improvement

### I.1.1. Active techniques

These techniques require external forces for moving the fluid inside the system, there are different methods to ensure the heat transfer augmentation such as [8–10]:

- Mechanical aids: Mechanical devices are integrated directly with the flow channels to move the fluid and improve heat exchange with the heated surface.
- Surface vibration: low or high-frequency vibrations have been used in single-phase flows to improve the heat transfer coefficients and to obtain its great values.
- Fluid vibration: Vibration is applied to the fluid using a flow switch or an electrical transducer by utilizing ultrasonic frequencies. It is used in single-phase flows, where is the most practical type of vibration enhancement technique.

- Electrostatic fields: These fields from continuous or alternating voltage sources, it can be magnetic or electric or the combination of both, which induces greater mass mixing around of the heat transfer surface to be mixed more and more.
- Jet impingement: This method is related to the direction of heating or cooling fluid perpendicularly or obliquely to the heat transfer surface, it is applied in one-phase and two-phase of the heat transfer processes.

### I.1.2. Passive techniques

These methods require special surface or geometries to the flow channel like integrate artificial roughness or external surface. they increase the heat transfer coefficients by changing the flow behavior. Where those techniques do not need any direct external power, which leads to an increase in fluid pressure drop, so, they can be achieved by utilizing [8–10]:

- Rough surfaces: They are created to promote turbulence in the flow field and near the wall region in the single-phase flow, rather increase the heat exchange surface in certain configurations. The realization of this kind of roughness is done by implantation of grains of sand or by discrete protuberances on the considered studied surface.
- Extended surfaces: They are used in several heat exchangers to provide an effective heat transfer augmentation, such as fusing integral parts inside or outside the duct, where known as fins or by changing the exchange surfaces by waving, by deformation or folding.
- Treated surfaces: The treatments are based on a precise modification on the exchange surface that by finishing or coating.
- Swirl flow devices: These devices can be integrated into the heat transfer surfaces, such as tube and plate exchangers, or fin tubes. Secondary flows due to this device increase the heat transfer coefficient, where this increase will be proportional to the increase in pressure drop.
- Additives: They are divided into two parts as follows, for liquids, these include in single-phase flows the addition of solid particles and gas bubbles which usually minimize the surface tension of the liquid for boiling systems. For gases, these integrate solid particles or liquid droplets, which are introduced either as a dilute phase or as a dense phase in single-phase gas flows.
- Coiled tubes: They creating secondary flows and vortices to enhance heat transfer coefficients.

### I.1.3. Compound techniques

A compound or hybrid techniques, because they are based on two or more of the active and passive techniques, where it can be used in combination simultaneously to ensure an enhancement of the thermo-hydraulic performance that is greater than the individual techniques applied separately [8–10].

The subject of our study will be based on the compound techniques, where, it is adopted to enhance the performance of the studied system "Solar Air Heater". One of the methods of enhancing the performance is by increasing the heat transfer coefficient between the fluid and absorber plate. Many investigators used artificial roughness of different materials, shapes, sizes, arrangements, and positions for increasing the heat transfer rate during forced airflow through a rectangular duct of the solar air heater.

## I.2. METHODOLOGY OF ARTIFICIAL ROUGHNESS GEOMETRY

As we know the conventional solar air heater system has low efficiency, so, there are many ways to increase it such as by increasing the absorbing area or by using the artificial roughness. Artificial roughness and different obstacles used in the channel of air passage in solar air heaters are used to increase the heat transfer rate either by breaking the laminar sub-layer or by creating the turbulence in the channel of air passage. The existence of a laminar sub-layer between the absorber plate and the flowing air is the main cause of the high thermal resistance for heat. Artificial geometry creates turbulence due to flow separation and reattachment between two consecutive roughness elements, which improves the heat transfer rate between the absorber plate and the flowing air, further, recirculation flow improves the convective heat transfer. Joule [11] was the first user the idea of artificial roughness in tube condensation of steam to improve the heat transfer coefficient and after that many researchers carried out studies on artificial roughness. Prasad and Saini [12] explained the effect of roughness height and thickness of laminar sub-layer on the behavior of roughness elements. They classified the roughened surfaces into three categories based on the height of artificial roughness (e) and thickness of laminar sublayer (δ) as shown in Figure I-3.

- If $e << \delta$: No effect on the heat transfer.
- If $e >> \delta$: More effect on fluid pressure as compared to heat transfer.
- If $e \geq \delta$: Noticeable augmentation in heat transfer and reasonable enhancement in pressure drop.

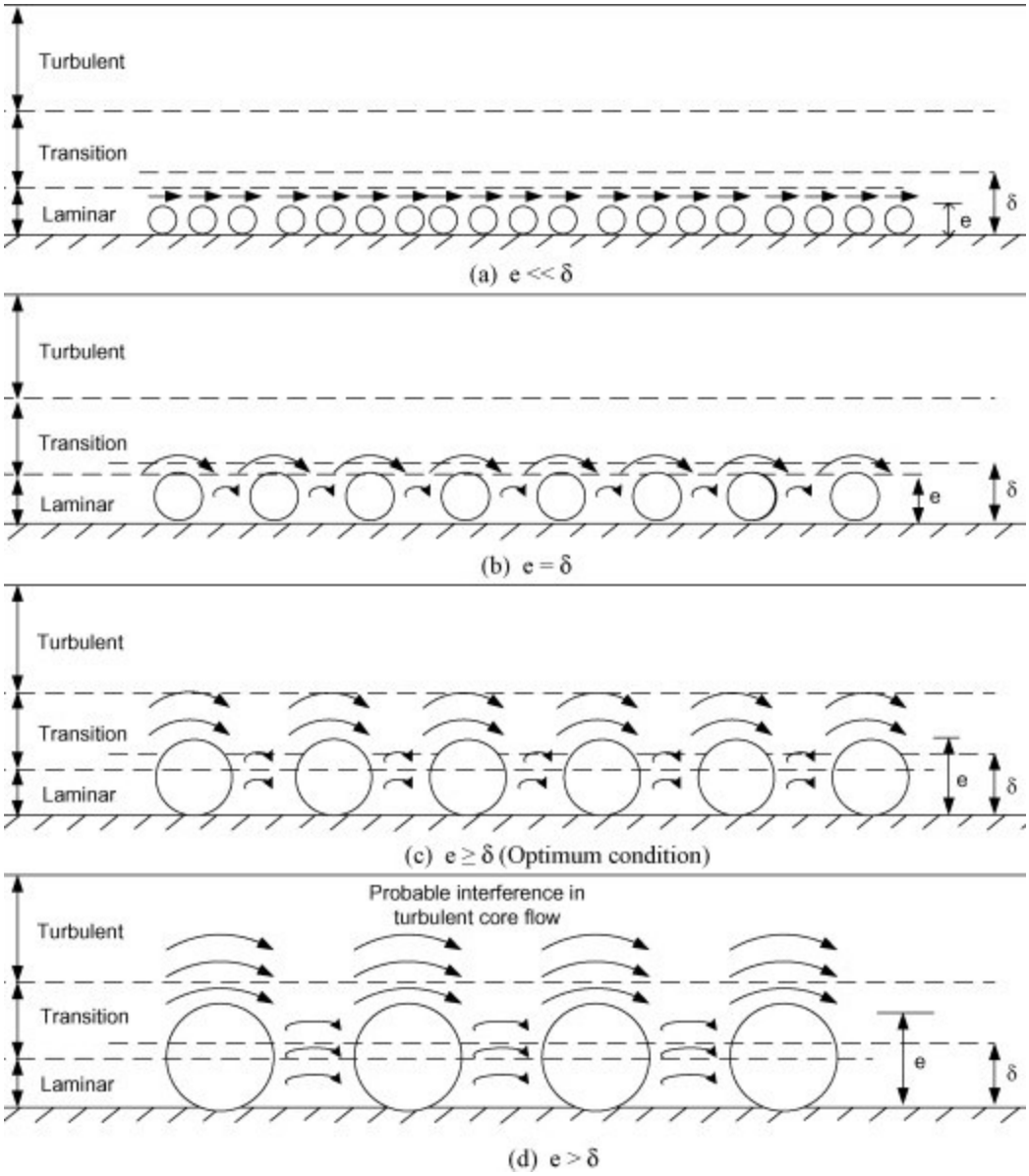


**Figure I-3:** Effect of artificial roughness height on laminar sub layer

## I.3. THE USED ARTIFICIAL ROUGHNESS IN SOLAR AIR HEATER

On the basis of the above, a general arrangement of the different artificial roughness configurations has been presented by different researchers such as ribs, protrusions, wire mesh, and baffles were considered as the most useful techniques available to enhance the solar air heaters performance. The most important parameters that describe the arrangement and shape of the roughness are the roughness element height (e) and pitch (p).

### I.3.1. The ribs

The different ribs geometries and orientations are extensively used for heat transfer improvement in solar air heater. The square ribs and circular shapes are used either in continuous or discretized form. The categorization and review the reported of the ribs are based on the various rib geometries studied and used by investigators and its effect on heat transfer coefficients and hydraulic performance which are presented below.

#### I.3.1.1. Transverse ribs

**a. Transverse continuous ribs**

From earliest investigations, Prasad and Mullick [13], the first to apply small diameter wire as roughness in solar air heater, under the studied parameters of relative roughness height of 0.019 and relative roughness pitch of 12.7. They reported application of wires led to improvement in plate efficiency factor from 0.63 to 0.72. After six years, the effect of small diameter wire transverse roughness on the thermal performance of solar air heater has been investigated by Prasad and Saini [14]. The studied roughness is shown in Figure I-4. It has been observed that the increase in relative roughness height results in a lower rate of heat transfer enhancement accompanied with the higher rate of friction factor enhancement. the decrease of the thermohydraulic performance results is related to the increase of the relative roughness pitch. The maximum improvement in Nusselt number and friction factor were 2.38 and 4.25 times than that of smooth duct, respectively.

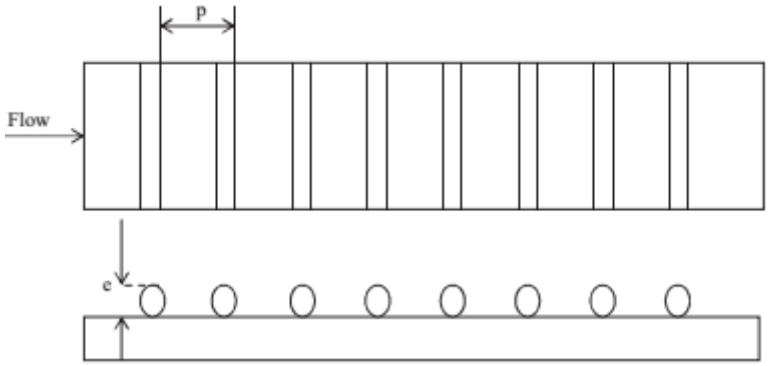


**Figure I-4:**Transverse small diameter wire

Gupta et al. [15] investigated experimentally the effect of rib roughness height on heat transfer and friction factor for Reynolds number ranges from 3000 to 18000 with a fixed value of relative roughness pitch, duct aspect ratio from 6.8 to11.5 and relative roughness height varied from 0.018 to 0.052. Stanton number increases up to the Reynolds number of 12000, and it decreases with further increase in Reynolds number. Another experimental study, Verma and Prasad [16] studied the heat transfer enhancement also

using transverse wire roughness for Reynolds number varied from 5000 to 20000. relative roughness pitch and relative roughness height ranges from 10 to 40, and from 0.01 to 0.03, respectively. The optimum value of thermo-hydraulic performance was found to be 71%corresponding to roughness Reynolds number of 24.

**b. Transverse broken ribs**

Sahu and Bhagoria [17] investigated transverse broken ribs on absorber plate of a solar air heater as shown in Figure I-5. Roughness geometry was having pitch (P) ranging from 10 to 30 mm, rib height (e) was 1.5 mm and duct aspect ratio was 8, the investigation was carried for Reynolds number as 3000–12000. Roughened absorber plate improved heat transfer coefficient by 1.25–1.4 times as compared to smooth duct operating under similar conditions. The maximum thermal efficiency of the order of 83.5% was obtained.

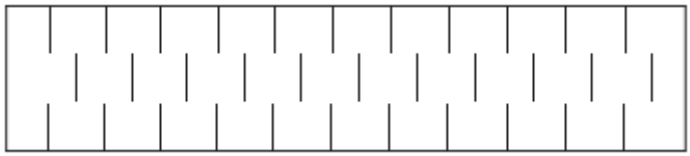

**Figure I-5** :Transverse small diameter wire

### I.3.1.2. Inclined ribs

**a. Continuous inclined ribs**

The proposition of the continuous inclined ribs has been investigated by Gupta et al. [18], as shown in Figure I-6. The effect of inclined ribs at an angle of 60° on heat transfer and friction factor also has been studied with fixed relative roughness pitch at 10 and relative rib height range from 0.023 to 0.50 for varying Reynolds number from 3000 to 18000. It has been reported enhancement in thermal efficiency by 1.16-1.25.

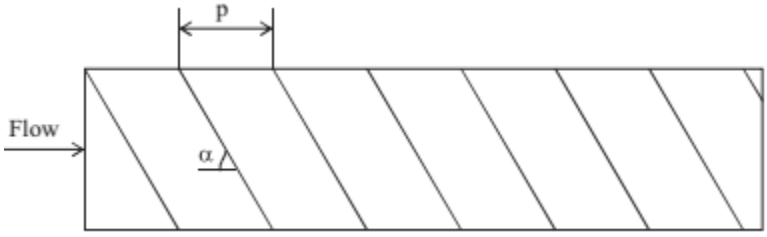


**Figure I-6 :** Continuous inclined rib

**b. Broken inclined ribs**

Aharwal et al. [19] investigated on inclined rib with a gap provision so as to allow release of secondary flow and main flow through the gap thereby creating local turbulence, where the gap width (g/e) and gap position (d/W) were in range of 0.5–2 and 0.1667–0.667 respectively as shown in Figure I-7. They found

enhancement in Nusselt number and friction factor to be 2.59 and 2.87 when compared to smooth solar air heater. The maximum thermo-hydraulic performance value was noted at relative gap width of 1.0 and relative gap position of 0.25.

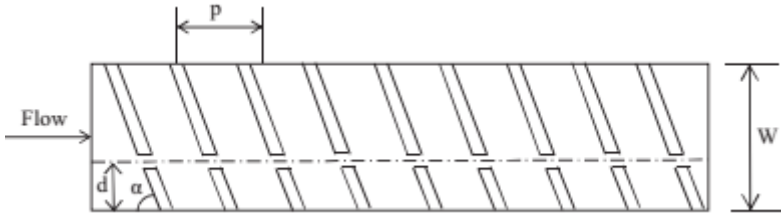


**Figure I-7:** Continuous inclined rib

### I.3.1.3. Wire mesh

Expanded metal mesh has been roughness used by Saini et al. [20] as shown in Figure I-8 (a). They investigated effect of relative long way length of mesh (l/e) and relative short way length of mesh (s/e) on thermo-hydraulic performance. They reported enhancement in heat transfer coefficient and friction factor of order of 4 and 5 times over smooth duct corresponding to angle of attack of 61.9° and 72° respectively.

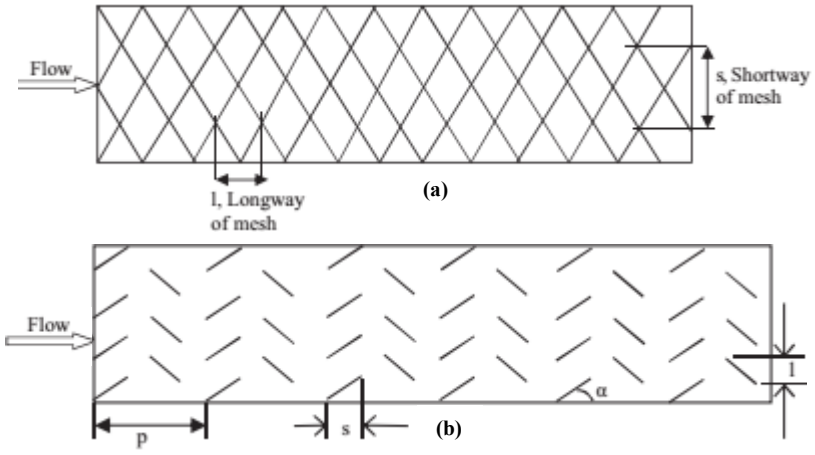


**Figure I-8: (a)** Expanded metal mesh, **(b)** Metal grit ribs

Karmare and Tikekar [21] used metal grit ribs to investigate heat transfer and friction factor as shown in Figure I-8(b). The investigation parameters were e/Dh as 0.035–0.044, p/e as 12.5–36 and l/s as 1.72–01 for Reynolds number range 4000–17000. They reported that the best roughness parameters are l/s as 1.72, e/Dh as 0.044 and p/e as 17.5 for the best performance.

### I.3.1.4. V-shaped ribs

#### a. Continuous V-ribs

Inclined rib, Gupta et al. [18] improved the performance than transverse ribs due to increase in secondary vortices. Momin et al. [22] increased the number of secondary vortices using V-shaping of angled rib which shown in Figure I-9 (a). They studied thermo-hydraulic performance of solar air heater for Reynolds number as 2500–18000, relative roughness height (e/d) ranges from 0.02 to 0.034 and angle of attack varied from 30° to 90°, for fixed relative roughness pitch (p/e) 10. Maximum enhancement of Nusselt number and friction factor was reported as 2.30 and 2.83 times that of smooth plate for angle of attack of 60°. The correlations for Nusselt number and friction factor as function of roughness and flow parameters for V- shaped ribs have also been developed.

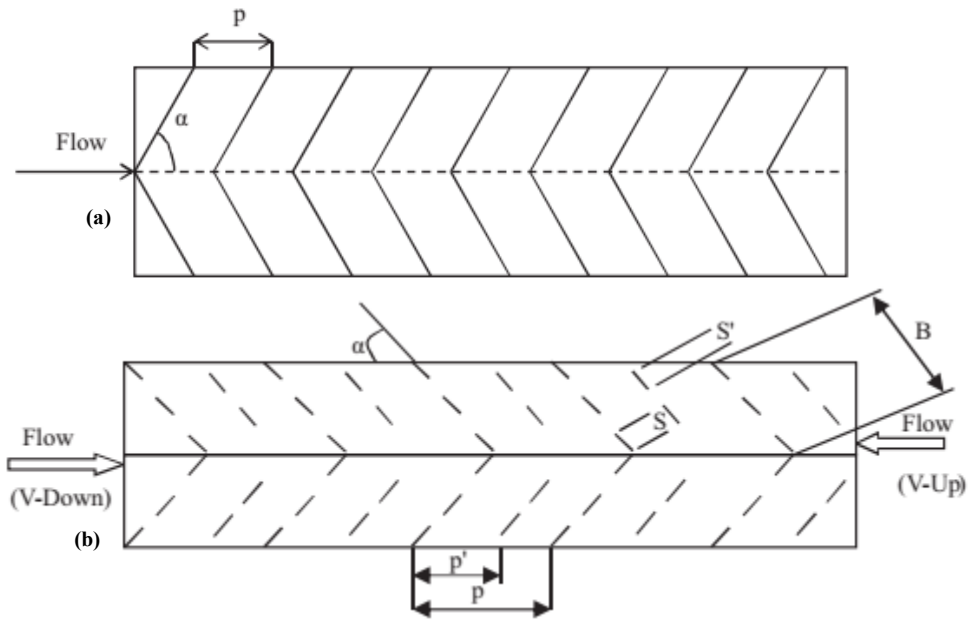


**Figure I-9: (a)** V-shaped ribs, **(b)** Discretized V-ribs

#### b. Discrete V-ribs

Karwa et al. [23] have investigated experimentally using v-discrete and v-discontinuous rib as presented in Figure I-9(b). The range of parameters was relative roughness length (B/S) as 3 and 6, relative roughness pitch as 10.63, angle of attack as 45° and 60° and Reynolds number as 2850–15500. They reported that discrete ribs perform better than discontinuous rib and angle of 60° better than 45°. Based on the comparison of Karwa [24] between transverse inclined, V-up continuous, V-down continuous, V-up discrete and V-down discrete, he reported that based on equal pumping criteria discrete V-down arrangement has best heat transfer performance.

### I.3.1.5. Multiple V-ribs

Hans et al. [25] investigated multiple V-ribs for Reynolds number from 2000 to 20000. Roughness geometry is shown in Figure I-10(a). The experiment based on relative roughness pitch as 6–12, relative roughness height as 0.019–0.043, angle of attack as 30° –75° and relative roughness width (W/w) range as 1–10.

Maximum heat transfer recorded for relative roughness width (W/w) of 6 while friction factor attained maximum value for relative roughness width (W/w) of 10. Nusselt number and friction factor attained maximum at attack angle of 60° and the maximum enhancement was 6 and 5 times respectively in comparison to smooth duct.

Concept of turbulence and acceleration of flow by providing gap has been used by Kumar et al. [26]. Roughness geometry is shown in Figure I-10(b). Range of parameter encompasses relative width ratio as 6, relative gap distance ratio as 0.24–0.8, relative gap width as 0.5–1.5, relative roughness height as 0.043 and angle of attack as 60°, Reynolds number from 2000 to 20000. They noted maximum enhancement in Nusselt number and friction factor as 6.32 and 6.12, respectively.

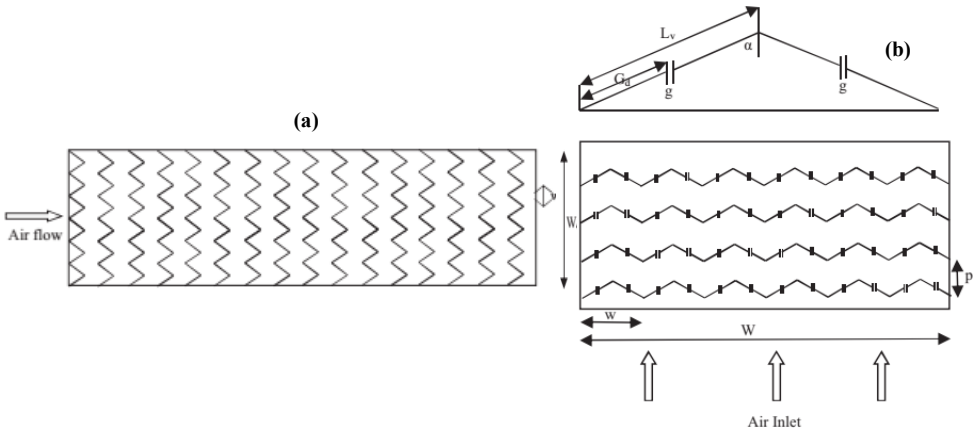


**Figure I-10 : (a)** Multiple V-ribs, **(b)** Multi V-shaped ribs with gap

### I.3.1.6. W-shape rib

#### a. Continuous W-ribs

Based on the role of increased number of secondary cells, Lanjewar et al. [27] experimentally investigated W-shape ribs as shown in Figure I-11(a). The considered parameters; angle of attack of 45°, relative roughness pitch of 10 and relative roughness height of 0.03375. W-ribs were tested in down and up arrangement.

W-ribs in down and up configuration provided the thermohydraulic performance parameters in the ranges of 1.46–1.95 and 1.21–1.73, respectively. The next study of Lanjewar et al. [28,29] also studied the

effect of angle of attack and rib roughness height were varied in the ranges of 30°–75° and 0.018–0.03375, respectively. The W-shaped rib roughness showed 2.36 and 2.01enhancement in the Nusselt number and friction factor with respect to a smooth duct while angle of attack was kept as 60°, respectively.

**b. Discrete W-ribs**

Kumar et al. [30] investigated discrete W-ribs with attack angle varied of 30° 75° and an aspect ratio (W/H) of 8 (see Figure I-11(b)) for Reynolds number from 3000 to 15000. They studied the effect of the relative roughness height (e/D) range of 0.0168-0.0338 at a fixed relative roughness pitch (p/e) of 10 on thermohydraulic.

The maximum Nusselt number and the friction factor were attained 2.16 times and 2.75 times, respectively higher than smooth duct at the relative roughness height (e/D) 0.0338, and angle of attack (a) 60°.

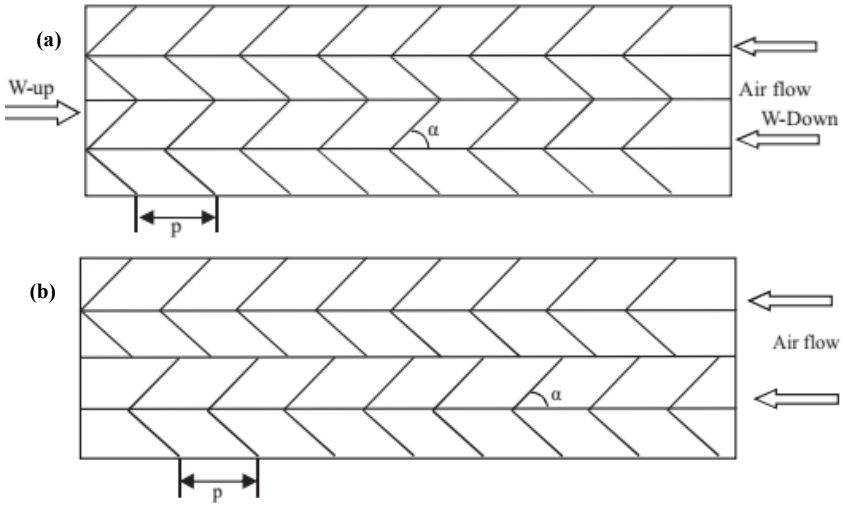


**Figure I-11:(a)** W-shaped rib roughness, **(b)** Discrete W-shaped ribs

**I.3.1.7. Arc shaped ribs**

Saini et al [31] carried out experimentally on arc-shaped rib roughened solar air heater for Reynolds number varied from 2000 to 17000, relative roughness height (e/D) (0.0213 to 0.0422) and relative arc angle (a) (0.3333 to 0.6666).

Enhancement of Nusselt number and friction factor was reported to be of order 3.6 and 1.75 times respectively over smooth duct for relative arc angle (a) value of 0.3333 and relative roughness height (e/D) value of 0.0422. Figure I-12 presents the roughness geometry used in this study.

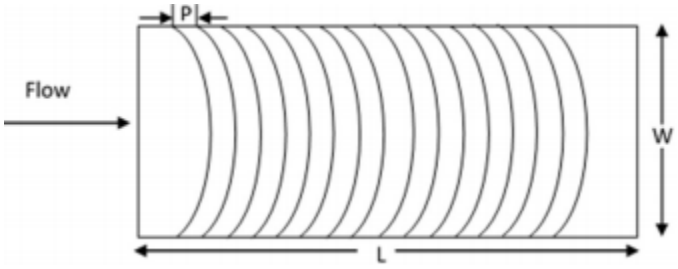


**Figure I-12 :** Arc shaped rib roughness

Various investigators [32–38] developed and studied the effect of multi and different arc ribs geometries on heat transfer and friction factor. The most studied roughness geometries have been shown in Figure I-13.

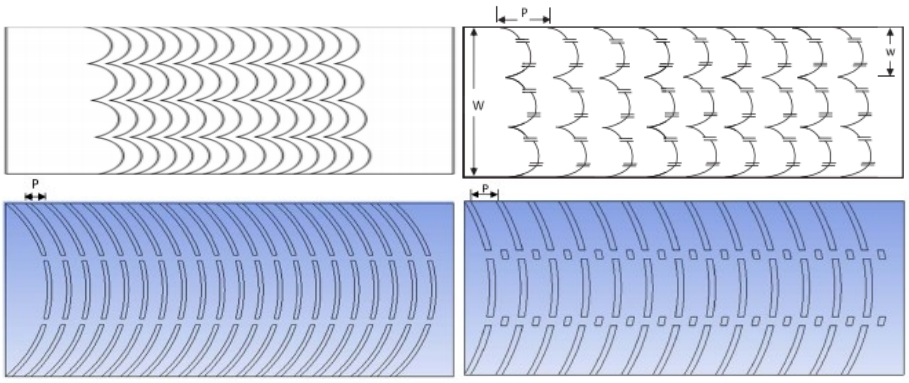


**Figure I-13 :** Different developed geometries of arc shaped rib roughness

### I.3.1.8. Chamfered ribs

Karwa et al. [39] conducted effect of chamfered rib as artificial roughness as shown in Figure I-14. Investigation was carried out for rectangular duct having aspect ratio of 4.8, 6.1, 7.8, 9.6 6 and 12 and rib chamfer angles of −15°, 0°, 5°, 10°, 15° and 18°, relative roughness height as 0.0141– 0.0328 and relative roughness pitch as 4.5–8.5, under Reynolds number as 3000–20000.

In comparison to smooth duct, they reported two and three times increase in Stanton number and friction factor respectively, also the best was chamfer angle of 15°.

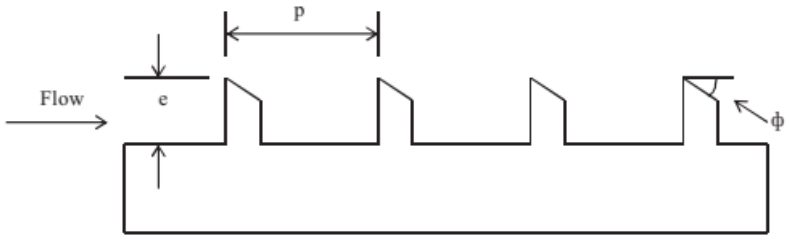


**Figure I-14 :** Chamfered ribs

### I.3.1.9. Wedge ribs

In a study by Bhagoria et al. [40], the heat transfer and friction of a transverse wedge shaped integral ribs of solar air heater have been conducted as shown in Figure I-15. The tests run based on Reynolds number variation, relative roughness pitch and relative roughness height. In comparison to smooth duct, the wedge shape rib roughness brought out 2.4 folds enhancement in Nusselt number while the friction factor was increased up to 5.3 times. The maximum enhancement in heat transfer corresponds to the wedge angle of 10°and relative roughness pitch of 7.57.

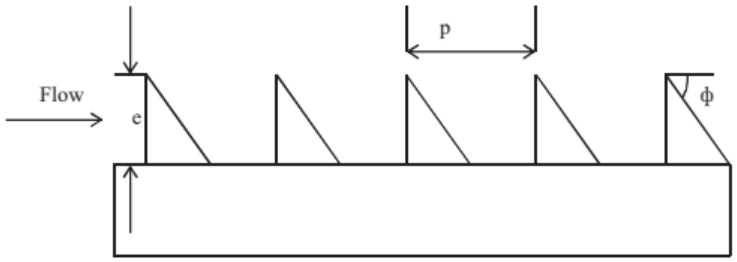


**Figure I-15 :**Wedge shaped transverse integral ribs

### I.3.1.10. Dimpled surfaces

A new concept of dimple shape artificial roughness (Figure I-16) was first employed by Saini et al. [41]. Investigation covered range of Reynolds number from 2000 to 12000, relative roughness pitch as 8–12 and relative roughness height as 0.018– 0.037. The dimple shape relative pitch of 10 and relative height of 0.0379 obtained maximum Nusselt number, however, combination of relative pitch of 10 and relative height of 0.0289 provided minimum friction factor.

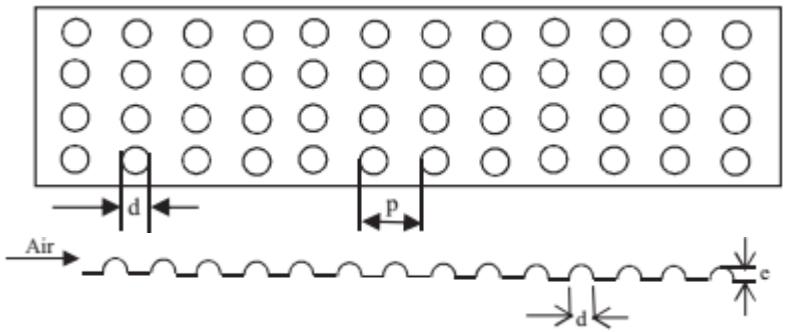


**Figure I-16 :** Dimple shape ribs

### I.3.1.11. Perforated ribs

An experimental investigation on the perorated ribs in an air channel by Buchlin [42]. He tested for Reynolds numbers from 30000 to 60000 five types of perforated ribs made in Plexiglas. The optimum design of ribs combines a rib pitch ratio of 5 with an open area ratio of 0.53. Nuntadusit et al. [43] studied

heat transfer and flow characteristics of six types of transverse perforated ribs as shown in Figure I-17using the thermochromic liquid crystal technique. the investigation based on geometry parameters, perforation inclination angles (q =0°, 15°, 30°), locations of hole on the rib (h = 0.2H, 0.5H, 0.8H). They noted that heat transfer increased immediately behind the rib by decreasing the height of perforation hole. The hole inclination of ribs (q = 15°, 30°) increases heat transfer. The enhancement was more significant for the one with large inclination angle (q = 30°).

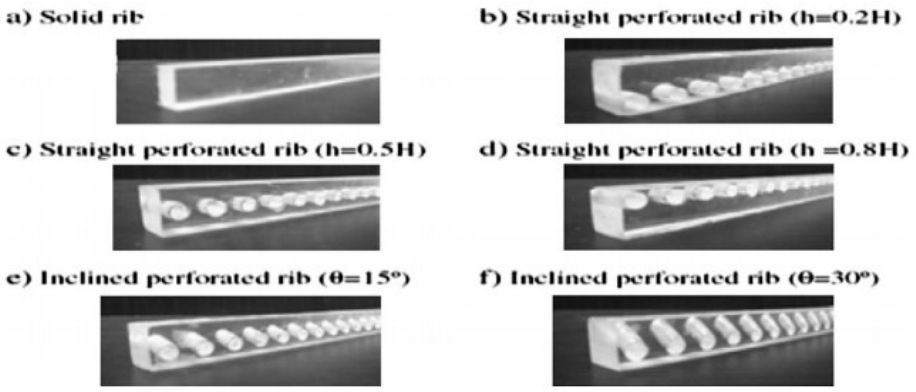


**Figure I-17:**Detail of ribs geometry

### I.3.1.12. Ribs combination

Many researchers [44–52] investigated the effect of different combined ribs geometries on the heat transfer and hydraulic performance. Figure I-18 shows the different combined ribs.

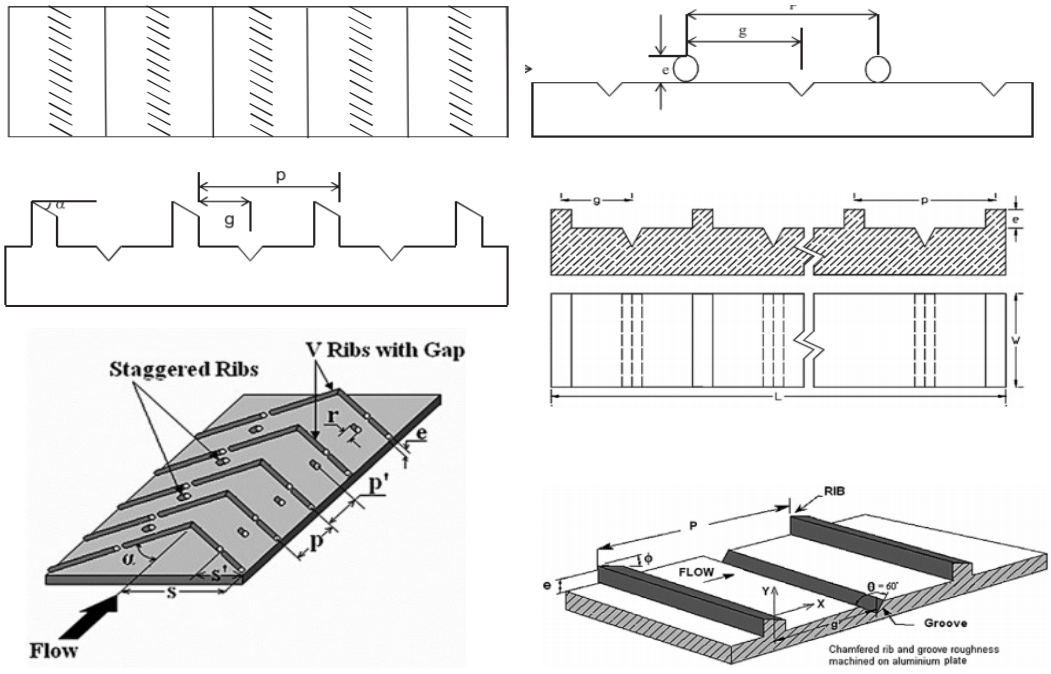


**Figure I-18 :**Different combined ribs

### I.3.2. The baffles

The different baffles geometries and orientations are extensively used to create a secondary flow, a rotary flow or turbulence for heat transfer improvement in solar air heater. Various baffles formed, including vortex generators, rectangular baffles, delta-shaped baffles, perforated and porous baffles can be attached and folded to create turbulence in the flow field.

The categorization and review the reported of the baffles are based on various studied geometries and the used by investigators and its effect on heat transfer coefficients and hydraulic performance which are presented below.

#### I.3.2.1. Solid baffles

##### I.3.2.1.1. Rectangular baffles

The increasing of the length of the air duct using transversal baffles has been carried by Biondi et al. [53] Figure I-19 (a) shows the partially transversal baffles fixed to the absorber play an aeraulic role, by obliging the air to take a meandering trajectory three times the length of the air duct itself.

The small longitudinal baffles have for role to restrict the flow of the air in touch with the internal surface of the absorber, as shown schematically in Figure I-19(b).

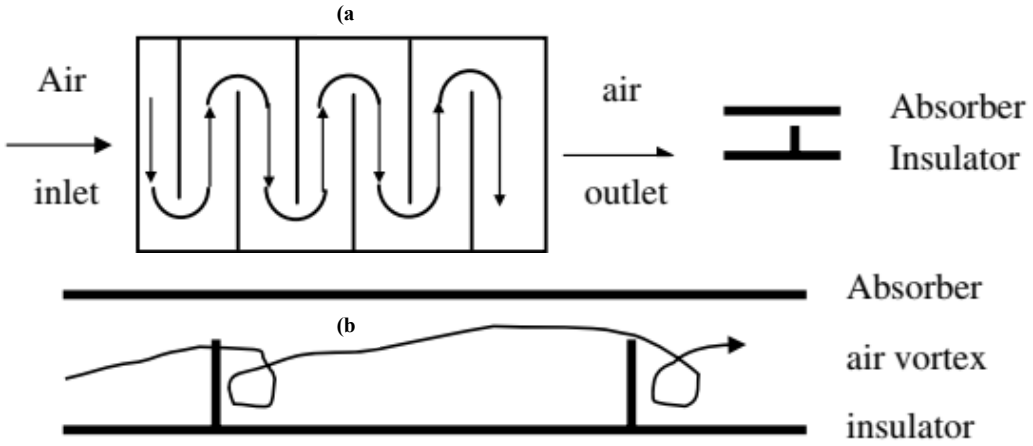


**Figure I-19: (a)**Transversal baffles, **(b)**The air restriction

Moummi et al. [54] carried out work to improve the thermal performances of the solar air collector for some applications. Their configuration is shown in Figure I-20. Initially, to improve the efficiency factor of these solar collectors, they created an increasingly turbulent flow between the absorber and the back wooden plate. For that, they used obstacles of various forms. In this study, they utilized rectangular plate fins inserted perpendicular to the flow. The results were compared with those obtained with a solar air collector without fins.

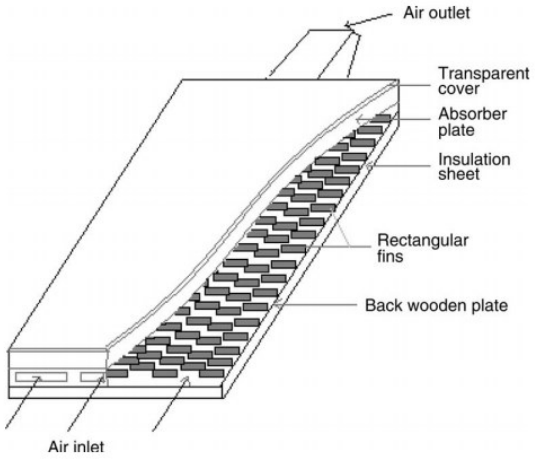


**Figure I-20 :** Collector with finned system on the back wooden plate

Promvonge et al. [55] carried out numerical study on periodic laminar flow and heat transfer behaviors in a three-dimensional isothermal wall square channel fitted with 30° angled baffles on one channel wall as shown in Figure I-21. The range of parameters used for the experiment were Reynolds number in the range of 100–2000, PR=1,1.5 and 2, BR=0.1–0.5. In this study, heat transfer enhancement was reported as 1.00–9.23 times for using baffle with BR=0.1–0.5. The pressure loss penalty was reported in the range of 1.09 to 45.31 times over the smooth duct. Maximum value of thermal enhancement factor was found to be 3.1 at BR=0.3 and PR=1.5.

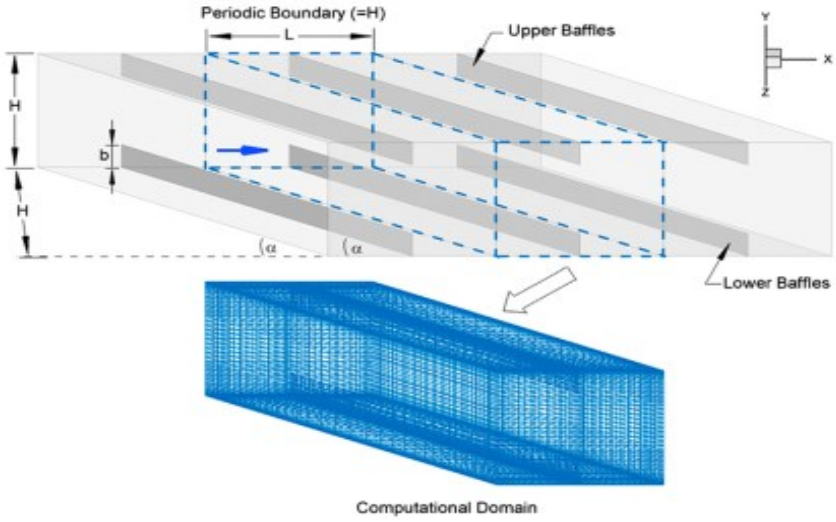


**Figure I-21 :** Duct geometry and computational domain with baffles

### I.3.2.1.2.Rectangular baffles with inclined upper part

Based on the previous studies of Aoues et al [56], the baffles fixed to the bottom plate of SAH(Figure I-22) formed with two parts: first part is perpendicular to fluid flow and the second part is inclined,

Menasria et al. [57] investigated numerically the effect of continuous rectangular baffles having an inclined upper part placed on bottom wall on thermohydraulic performance in a SAH duct.

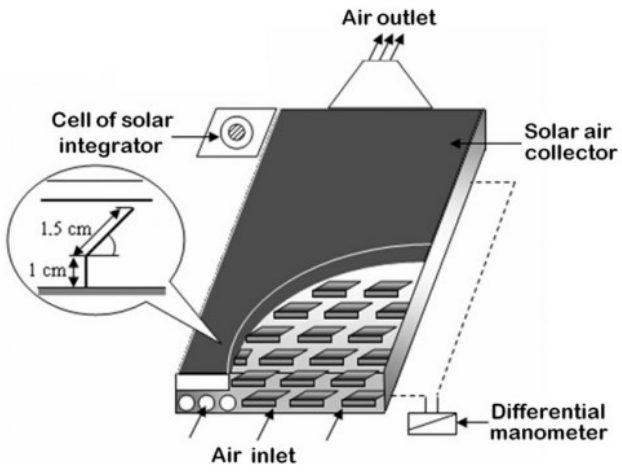


**Figure I-22 :** Solar air heater with rectangular baffles having an inclined upper part

The studied case is shown in Figure I-23. The configuration having flow blockage ratio of 0.7, baffle-pitch spacing ratio of 2 and the Reynolds of 5000 brought out the best thermohydraulic performance factor. The presence of baffles on the bottom wall of ducts was noted to be an effective technique to improve the heat transfer rates. The geometry, location of baffles, and Reynolds number are the main controlling parameters.

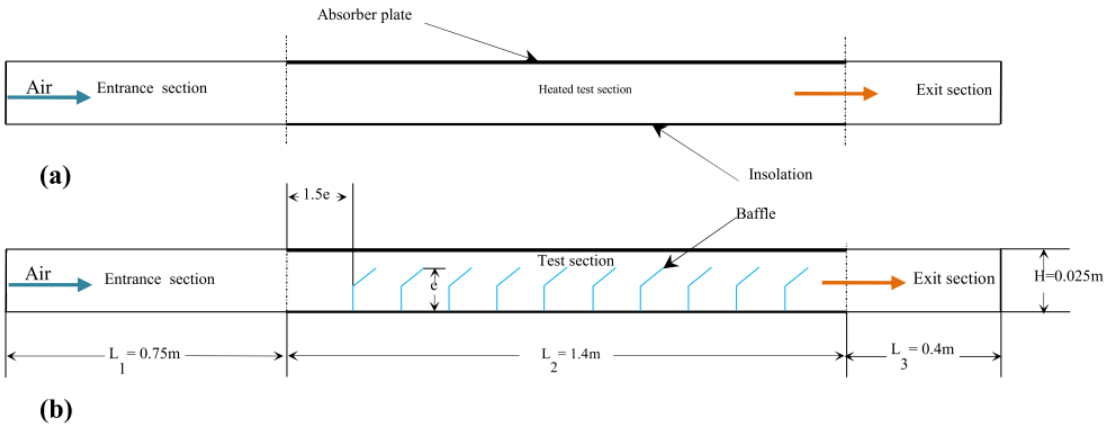


**Figure I-23:**Schematic of studied domain (a) smooth duct (b) baffled duct

### I.3.2.1.3. Cylindrical baffles

Leander Antony et al [58] studied numerical analysis on the thermal performance enhancement of a flat plate solar air heater provided with stepped cylindrical turbulators attached below the absorber plate for Reynolds numbers ranging from 3000 to 24000. The number of steps on the turbulator is varied from 1 to

3 and the number of rows of turbulators is varied from 1 to 3, where core diameter of turbulators varying from 3 mm to 7 mm in steps of 1 mm and the relative roughness pitch ratio is varied as 11.11, 16.67, 22.22, and 27.78. It has been noticed that the thermal enhancement factor increases with the increment in number of rows and also increases with decrease in core diameter for Reynolds number range beyond 12000. The maximum Nusselt number of 76.41 was obtained for a core diameter of 7 mm corresponding to a three-row configuration at a flow Reynolds number of 24000, and maximum thermohydraulic performance parameter of 1.49 was achieved corresponding to a Reynolds number of 18000. Figure I-24 shows the studied configuration.

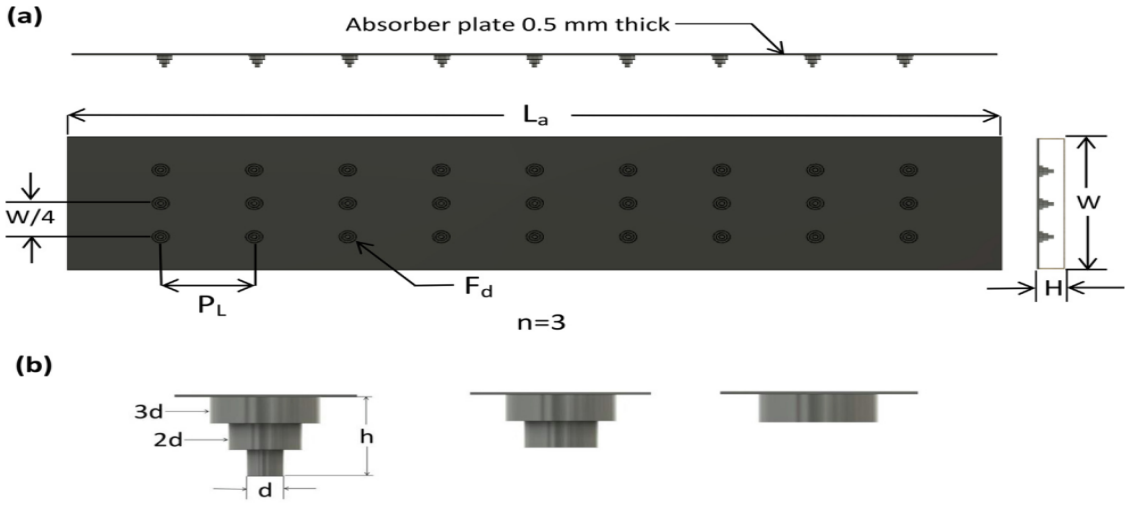


**Figure I-24 :** Baffle configurations

**I.3.2.1.4. V-baffles**

An experimental investigation by Promvonge [59] was achieved to assess turbulent forced convection heat transfer and friction behaviors for airflow through a channel fitted with a multiple 60° V-baffle turbulator as shown in Figure I-25 (a).

Experiment was carried out using a channel of aspect ratio, AR=10 and height, H=30 mm with three different baffle blockage ratios, (e/H=0.10, 0.20 and 0.30) and three baffle pitch spacing ratios, (PR=P/H=1, 2 and 3) while the transverse pitch of the V-baffle is set to 2 H and kept constant. In comparison with smooth duct, the experimental results confirmed that the V-baffle provides the drastic increase in Nusselt number, friction factor values due to better flow mixing from the formation of secondary flows induced by vortex flows generated by the V-baffle. At lower Reynolds number, the use of V-baffle with e/H=0.10 and PR=1, reported the highest value of 1.87 for thermal enhancement factor. The next studies were numerical investigations on V-baffle turbulator by Promvonge et al. [60,61], where at the same year of [59] Promvonge et al [60] was examined periodic laminar flow and heat transfer characteristics in a three-

dimensional isothermal wall channel of aspect ratio, AR=2 with 45° staggered V-baffles. After two years, Promvonge et al [61] used inline 45° V-shaped baffles on two opposite walls. The computational domain is shown in Figure I-25 (b).

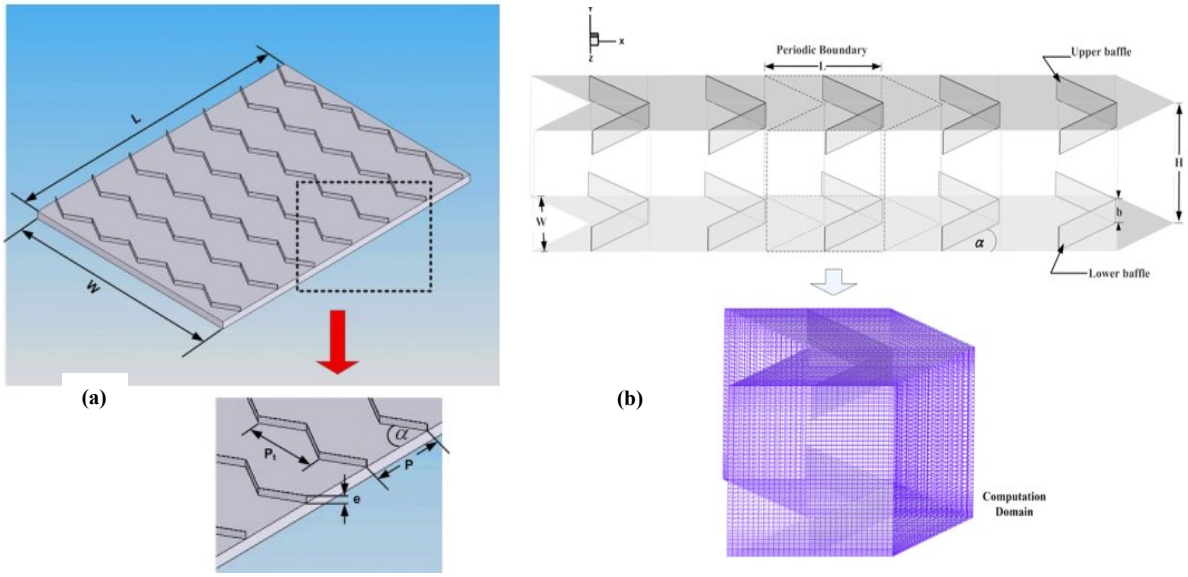


**Figure I-25 : (a)** Multiple 60° V-baffles, **(b)** Computational domain with45°V-baffles

### I.3.2.1.5. Z-baffles

Sriromreun et al. [62] investigated experimentally and numerically the effect of baffle turbulators on heat transfer augmentation in a rectangular channel of aspect ratio of 10 fitted with the in-phase and out-phase 45° Z-baffles in the turbulent regime from Re=4400 to 20400. In the experiment, the baffles were placed in a zigzag shape (Z-shaped baffle) aligned in series on the isothermal-fluxed top wall, similar to the absorber plate of a solar air heater channel. The Z-baffle pitch spacing and height length effect were examined to find the optimum thermal performance for the Reynolds number from 4400 to 20400.

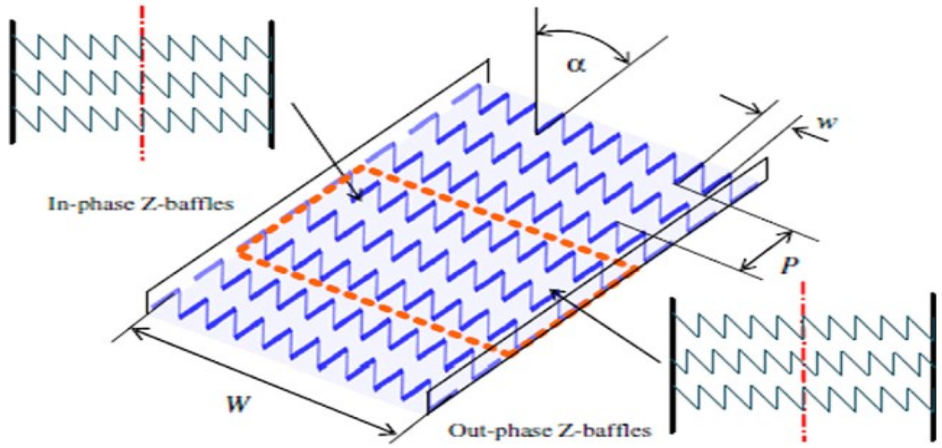


**Figure I-26 :** Z shaped baffles arrangement in SAH

The Z-baffles inclined to 45° relative to the main flow direction were characterized at three baffles to channel-height ratios (e/H=0.1, 0.2 and 0.3) and baffle pitch ratios (P/H=1.5, 2 and 3). Importantly, the Z-baffle with e/H=0.1 at P/H=1.5 shows higher heat transfer rate than the one at P/H=2 and 3 around 15% and 30%, respectively. The arrangement of baffles is shown in Figure I-26.

### I.3.2.2. Porous and perforated baffles

#### I.3.2.2.1. Porous baffles

Rectangular duct with porous baffles which are arranged on the top and bottom duct walls in a periodically staggered way has been studied numerically predictions by Yang and Hwang [63]. the numerical prediction based on experimental parameters of baffle height (h/H=0.25, 0.5 and 0.75 mm), porosities (υ=0.2, 0.42 and 0.7) and fixed baffle spacing S/H at 1.0. Replacing the solid baffles by the porous baffles helps to reduce the thermal conductivity of the baffle, so flow transport phenomenon changes and the heat transfer increases. The friction factor had a lower value for porous-type baffle in comparison to the solid-type baffle because of less channel blockage. A schematic of porous baffles is shown in Figure I-27.

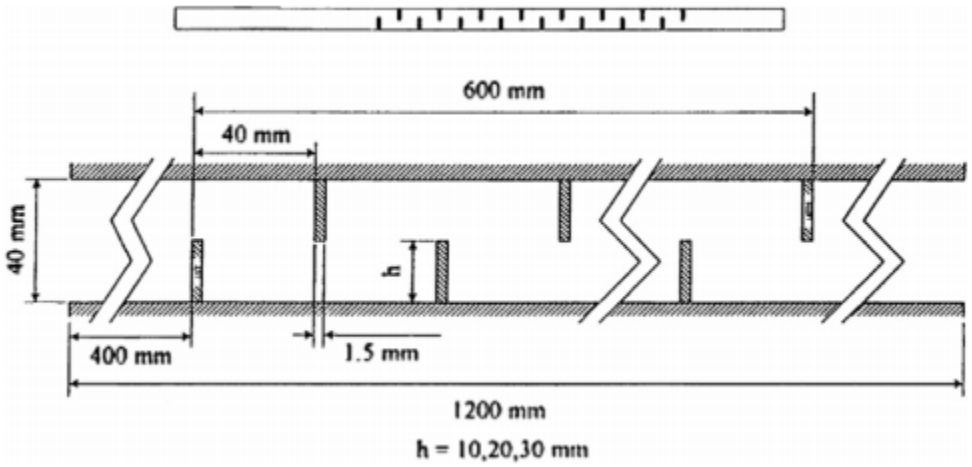


**Figure I-27:** Channel with porous baffles

#### I.3.2.2.2. Perforated baffles

Karwa and Maheshwari [64] studied experimentally the heat transfer and friction in a rectangular section duct with fully perforated baffles (open area ratio of 46.8%) or half perforated baffles (open area ratio of 26%) at relative roughness pitch of 7.2–28.8 affixed to one of the broader walls as shown in Figure I-28. The Reynolds number of the study ranges from 2700 to 11150. The baffled wall of the duct is uniformly heated while the remaining three walls are insulated.

The study represent an enhancement of 79–169% in Nusselt number over the smooth duct for the fully perforated baffles and 133–274% for the half perforated baffles while the friction factor for the fully

perforated baffles is 2.98– 8.02 times of that for the smooth duct and is 4.42–17.5 times for the half perforated baffles. The half-perforated baffles at a relative roughness pitch of 7.2 give the greatest performance advantage of 51.6–75% over a smooth duct at equal pumping power.

Djamel Sahel et al [65] investigated numerically the performance of a new perforated baffle design aiming to enhance the heat transfer phenomenon in the channel as shown in Figure I-29. the perforated baffle having a row of four holes placed at three different positions.

These positions are described by a ratio called the PAR (Pores Axis Ratio), where their values are 0.190, 0.425 and 0.660, respectively. The characteristics of fluid flows and heat transfer are presented for Reynolds numbers ranging from 104 to 105.

All investigations based on the CFD code Fluent. The validation of the numerical results has been done with available experimental data and a satisfactory agreement is found. The obtained results show that the Pores Axis Ratio (PAR) of 0.190 is the best design that eliminates significantly the LHTAs, giving thus an increase in the heat transfer rate from 2% to 65% compared with the simple baffle.

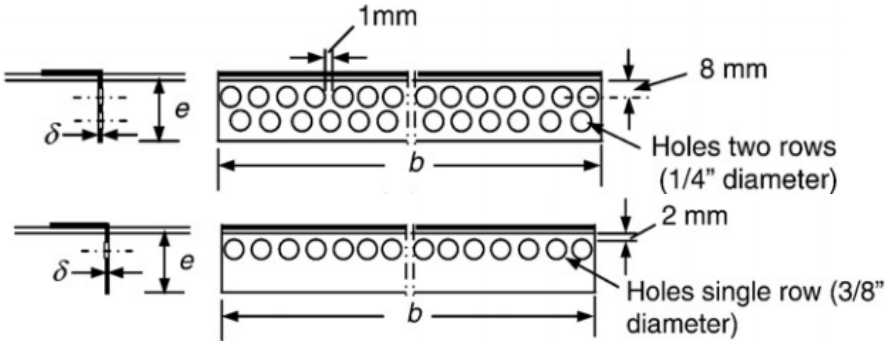


**Figure I-28 :** Schematic of the fully perforated baffles (with two rows of holes) and half perforated baffles (with single row of holes)

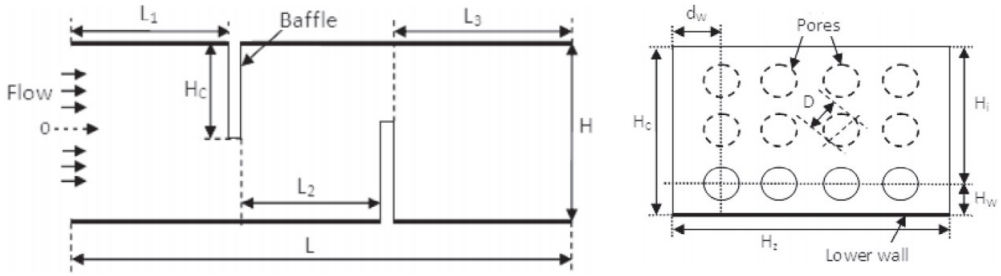


**Figure I-29 :** Schematic of the channel and the perforated baffle geometry

### I.3.2.3. Delta winglet

The secondary or rotary flow is created using swirl or vortex generators that are inserted in main flow that to enhance the rate of heat transfer in engineering devices like heat exchange, where the delta winglet one of the vortex generators.

An experimental study was achieved by Yakut et al. [66] to study the effects of various delta-winglet vortex generators (Figure I-30 (a)) on the heat transfer and flow characteristics. The maximum vortex-shedding frequency occurred at 16906 Reynolds number, 25 mm pitch, 8 mm winglet height and 30° angle of attack. The minimum vortex-shedding frequency was obtained at 3690 Reynolds number, 75 mm pitch, 16 mm winglet height and 90° angle of attack.

The maximum heat-transfer rate was observed at 16906 Reynolds number, 60° angle of attack, 16 mm winglet height and 25 mm pitch of the winglets and the minimum friction factor was observed at 8 mm winglet height, 16906 Reynolds number, 30° angle of attack and 75 mm pitch. The optimum results were obtained at 25 mm pitch, 8 mm height of winglet, 30° angle of attack and a Reynolds number of 16906 for larger frequencies required to avoid resonance. The optimum results were 75 mm pitch, 8 mm height of winglet, 60° angle of attack and a Reynolds number of 16906. The entropy generation in a cross-flow HX with a new winglet-type convergent-divergent longitudinal vortex generator (CDLVG) has been studied by Kotcioglu et al. [67] as shown in Figure I-30. The low Reynolds number has influenced on the heat transfer while at the high Reynolds number has influenced on the pressure drop. The present vortex generator (CDLVG) shows an increase in the heat transfer enhancement from 15% to 30% and also an increase in the pressure-loss penalty from 20% to 30%.

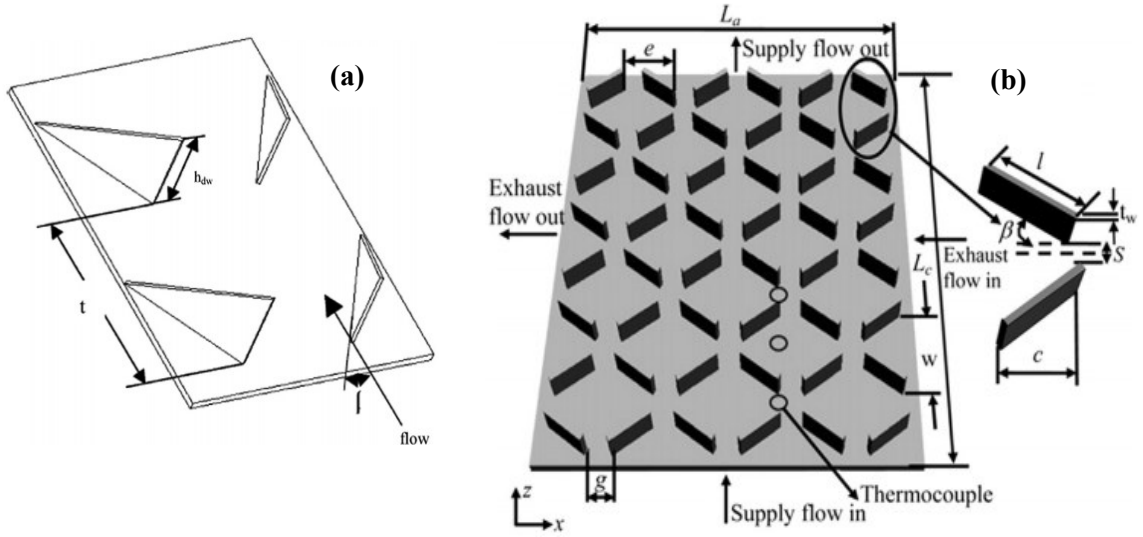


**Figure I-30 :** Different winglets in rectangular channel

### I.3.2.4. Other baffles shapes

There are several baffles shapes has been used from numerous researchers which studied its effect on the thermohydraulic performance. Sripattanapipat et al. [68] investigated numerically the laminar periodic fluid flow and heat transfer of two-dimensional horizontal channel with isothermal walls and with staggered baffles as shown in Figure I-31.

The influence of different baffle tip angles on heat transfer and pressure loss in the channel were conducted and the results of the diamond baffle were compared with simple baffle. The order of enhancement was reported about 200–680% for using the diamond baffles. The augmentation was associated with enlarged friction loss ranging from 20 to 220 times above the smooth channel.

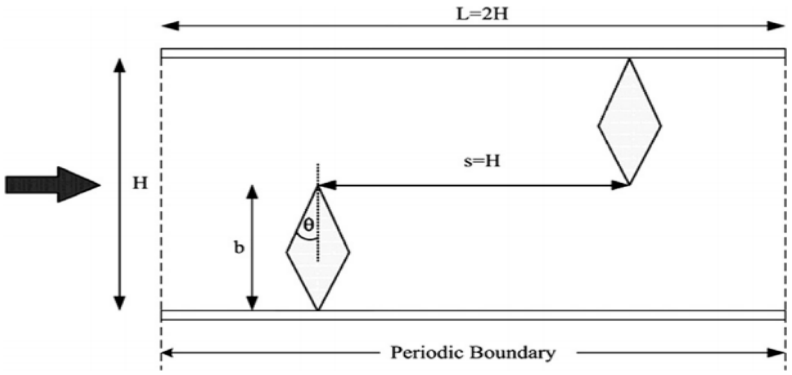


**Figure I-31 :** Diamond shape baffle

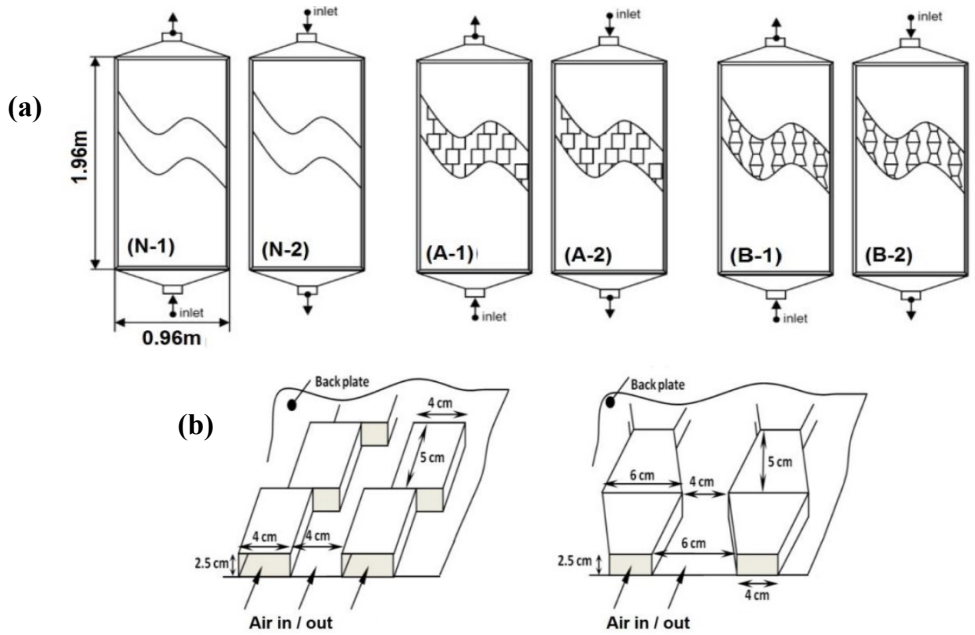


**Figure I-32 :** Schematic of different solar air heater designs (a) and the geometry of the studied obstacles (b)

Labed et al [69] carried out a comparative study on the thermal performance and pressure drop for two obstacle configuration son several designs of solar air heater (Figure I-32 (a)(b)), where they proposed: 1) adding different forms of obstacles in the airflow duct, 2) reversing the flow direction (blowing up / blowing down), 3) rotating the flow around the bottom plate to obtain a double pass flat plate collector having trapezoidal obstacles.

Abene et al. [70] studied the efficiency-temperature rise couple of the flat-plate solar collector by considering different baffles shapes as ogival transverse (OT), ogival inclined folded (OIF), waisted tube

(WT), waisted delta lengthways (WDL) and waisted ogival lengthways (WOL) and transverse longitudinal obstacles (TL).

Baissi et al. [71] carried out an experimental study to improve the thermo-hydraulic performance in the absorber surface of a SAH channel fitted with perforated and non-perforated longitudinally curved delta-shaped baffles as shown in Figure I-33.

The investigation encompassed for the range of Reynolds number (Re) from 2500 to 12000, relative longitudinal length of the obstacles on the absorber plate Pl/e from 3 to 5, relative transversal length of the obstacles on the absorber plate Pt/b from 0.6 to 1, relative roughness height (e/H = 0.8) and single attack angle (α = 45°). Significant heat transfer rates, as well as a significant increase in friction factor have been obtained when compared to those obtained with smooth channel.

The maximum thermal enhancement factor (TEF) rate was found to be around 2.26 when Pl/e and Pt/b are respectively equal to 0.3 and 0.6.

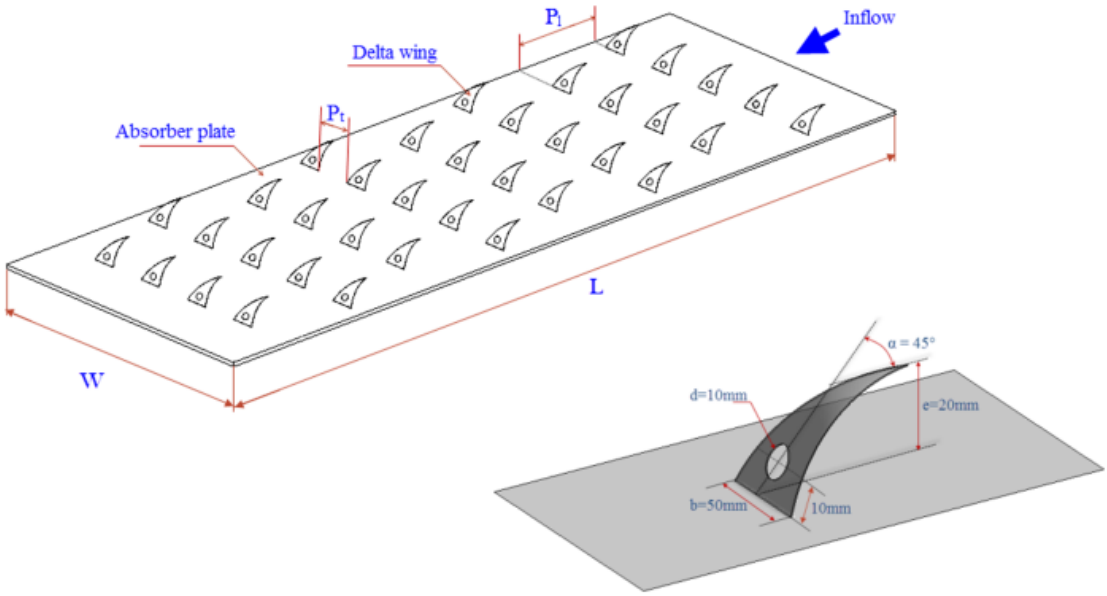


**Figure I-33 :** Schematic of absorber plate with longitudinally curved delta-shaped baffles

### I.3.2.5. Baffles combination

The combination of different baffle configurations has been investigated by several researchers. Yeh et al. [72] conducted experimentally the solar air heater efficiency with a combination of baffles and fins as shown in Figure I-34 (a). The used baffles to create the air turbulence and extended the heat transfer area. This arrangement caused considerable improvement in collector efficiency. It was studied that increasing the density of baffles also increases the collector efficiency but this will increase the power consumption by blower.

Yeh et al. [73] investigated theoretically the effect of baffles and aspect ratio of air duct on the efficiency of the solar air heater. The increase of efficiency with the increase of aspect ratio has been noted. The performance of a double-pass solar air heater with fins and baffles design was investigated by Chi-Dong et al. [74] basing both experimental and theoretical approaches, for the recycling operation effect. The performances of the new design and the other two designs, which are double-pass without fins and double-pass with fins only, were compared.

The best collector efficiency was noted for new design as compared to all other designs under recycling operation. The improvement of collector efficiency was found due to use of baffles. The best possible reflux ratio for the fined plus baffled double-pass design was investigated about 0.5 while considering both the collector efficiency and the pumping power requirement. A schematic of a fined plus baffled double pass solar air heater is shown in Figure I-34(b).

Akpinar and Koc-yigit [75] experimentally studied the heat transfer performance of a new flat-plate SAH with several obstacles (Types I–III) and without obstacles (Type IV) as given in Figure I-35. Experiments were performed for two air mass flow rates of 0.0074 and 0.0052 kg/s.

The energy and exergy efficiencies were determined for SAHs and comparisons were made among them. The energy efficiency values changed between 20% and 82%. The exergy efficiency values varied from 8.32% to 44.00%.

They reported that the highest efficiency was determined for the SAH with Type II absorbent plate in flow channel duct for all operating conditions, whereas the lowest values were obtained for the SAH without obstacles (Type IV).

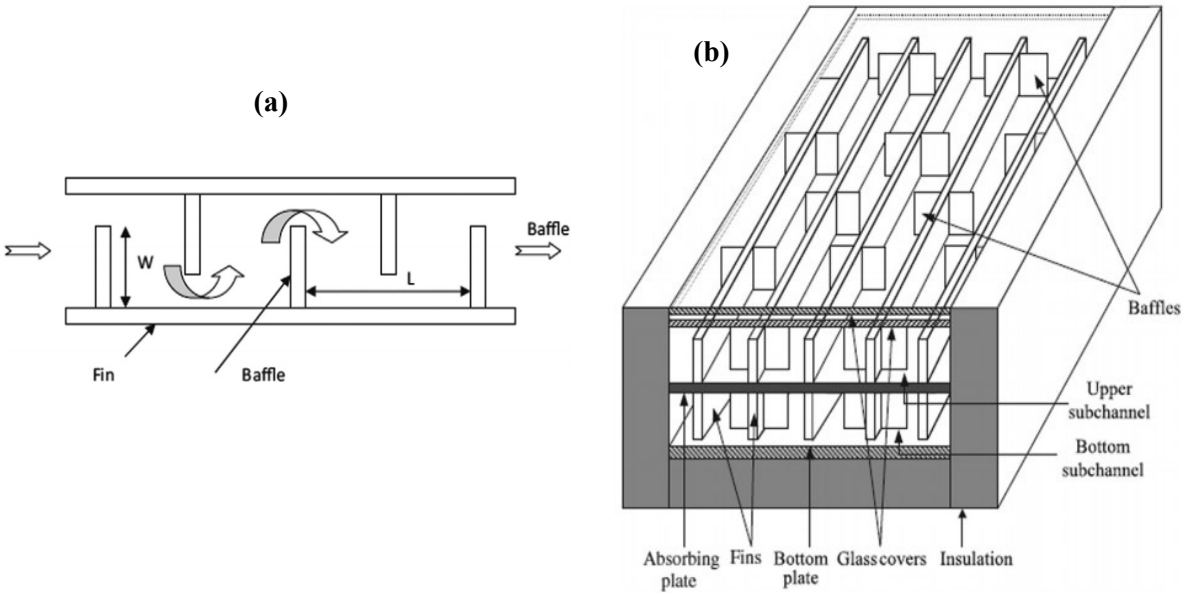


**Figure I-34 :** Solar air heaters with fins and baffles

Recently, Jianjun Hu et al [76] used baffles with holes in solar air collector (BSAC) to improve the thermal performance. Small jets were created when fluid flowing out of the holes, which can weaken or blow away the vortexes behind baffle avoiding the generation of hot spots, and the bypass effect caused by these holes can reduce the flow resistance simultaneously.

Moreover, these small jets strengthen the mixing and flow disturbance, which can enhance the heat transfer between the airflow and absorber plate leading to efficiency improvement.

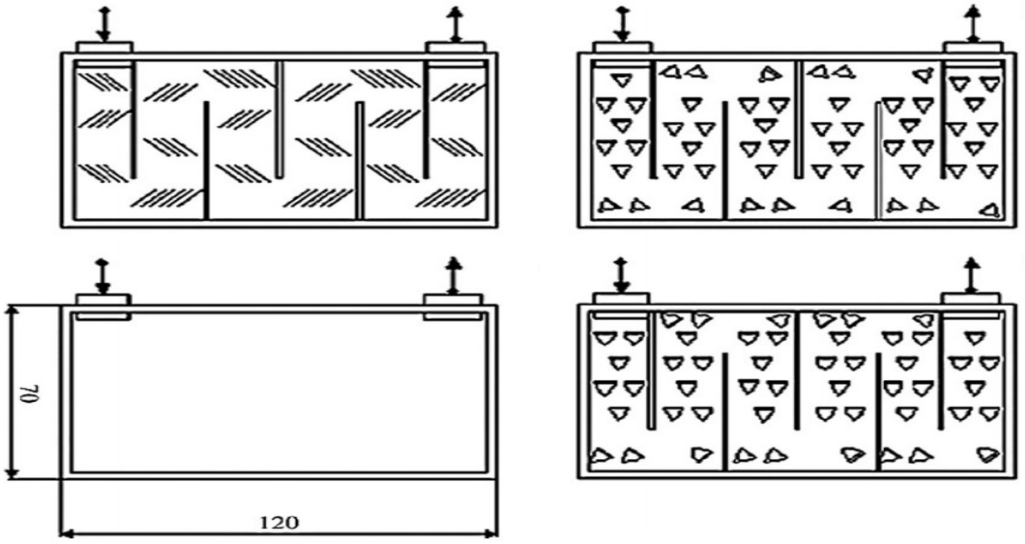


**Figure I-35 :** Solar air heaters with compound baffles

The hole impact parameters on thermal performance of the studied system were studied by orthogonal numerical tests. The optimal parameter combination under different flow rates was obtained. The optimal system efficiencies are 69.63%, 81.71%, and 86.83% corresponding mass flow rates 0.0044, 0.0088, and 0.0132 kg/s.m$^2$, respectively.

A numerical comparison has been made between the BSAC with and without holes on baffle, which explains the reason why the improved BSAC can promote the thermal efficiency and reduce the flow resistance simultaneously, providing a theoretical basis for the performance improvement of BSAC. A schematic of BSAC is shown in Figure I-36.

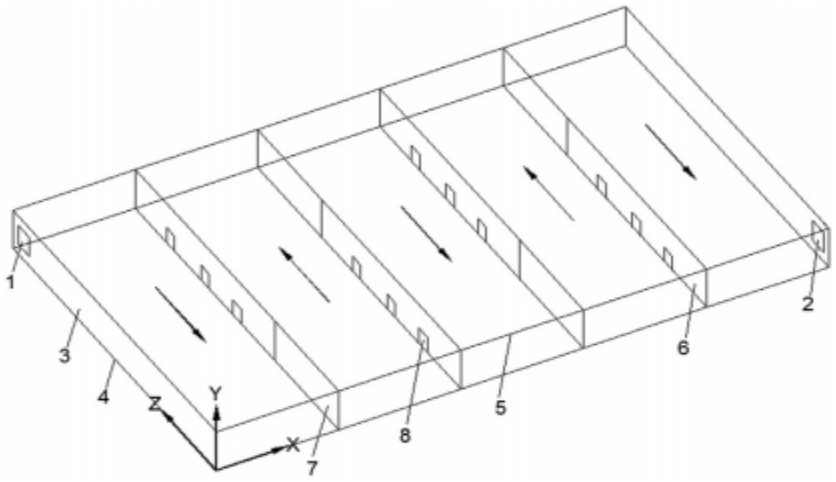


**Figure I-36:** Three-dimensional computational model: 1. Inlet 2. Outlet 3. Periphery structure 4. Absorber plate 5. Glass cover 6. Baffle 7. Passageway 8. Rectangle hole.

## I.4. PERFORMANCE ANALYSIS OF SOLAR AIR HEATER

The thermohydraulic performance of a solar air heater for describing the efficiency of the whole system. The heat transfer corresponding thermal performance within the solar air heater and hydraulic performance concerns with pressure drop in the duct. The following equations enable one to calculate the thermal and thermohydraulic efficiency of solar air heater.

### I.4.1. Thermal characteristics

Thermal performance of solar air heater can be evaluated by the following equation investigated by Hottel-Whillier and Bliss [77,78] and given by Duffie and Beckman [2].

Bliss [78] introducing 'collector heat removal factor', $F_R$, defined as the ratio of actual useful energy gain to the useful energy gain if the whole collector absorbing surface were at the fluid inlet temperature.

$$Q_u = A_c F_R [\, I_G(\tau\alpha)_e - U_L(T_{in} - T_a)] \quad \text{(I-1)}$$

The rate of useful energy gain by the flowing air through duct of a solar air heater may also be calculated by using the following equation:

$$Q_u = \dot{m} C_p (T_{out} - T_{in}) = h A_c (T_{pm} - T_{fm}) \quad \text{(I-2)}$$

As discussed above, heat transfer coefficient ($h$) can be described in non-dimensional form by using the following relationship of Nusselt number ($Nu$) reported by Duffie and Beckman [2]:

$$Nu = \frac{hD_H}{k} \quad \text{(I-3)}$$

### I.4.2. Hydraulic characteristics

Thermal performance does not describe the pumping power loss, therefore it is necessary to take into account the hydraulic performance for the optimum design. Hydraulic performance of a solar air heater concerns with pressure drop ($\Delta P$) in the duct. Pressure drop accounts for energy consumption by a blower to propel air through the duct. The pressure drop is related to the friction factor between air and surface of flow channel by the following equation reported by Frank and Mark [79]:

$$f = \frac{(\Delta P/L)D_H}{2\rho V^2} \quad \text{(I-4)}$$

Where $D_H$ is the hydraulic diameter of the test section, calculated by multiplying cross-section A by four and dividing by the cross-section wet perimeter p:

$$D_H = \frac{4A}{P} \quad \text{(I-5)}$$

### I.4.3. Thermohydraulic characteristics

To evaluate the overall performance of a system, it is therefore vital to simultaneously take into account both the heat transfer and hydrodynamics. Webb and Eckert [80] defined the thermo-hydraulic performance parameter ($THPF$) which shows the enhancement of heater transfer of roughened duct relative to smooth duct operating under similar conditions and require same pumping power. The thermohydraulic performance factor is given as follows:

$$THPF = \frac{{}^{Nu}/_{Nu_s}}{\left({}^{f}/_{f_s}\right)^{\frac{1}{3}}} \quad \text{(I-6)}$$

## I.5. CONCLUSION

This chapter introduced some background information and state of the art on solar air heaters. The solar air heaters with artificial roughness have an improved heat transfer rate compared to smooth solar air heaters or without artificial roughness. At the start of this chapter, the different mechanisms and techniques to improve the performance of solar air heaters have been presented. The main categories of the artificial roughness to improve the solar air heaters performances are the ribs and the baffles where each category has many classifications based on the shapes, sizes, orientations and arrangements. The last part concerns the parameters of thermohydraulic performance corresponding heat transfer and pressure drop of solar air heaters to evaluate the overall studied system.

# *CHAPTER II*

# *EXPERIMENTAL STUDY*

## II.1. INTRODUCTION

From the necessary points of the current work are the fabrication steps, design parameters, operation conditions and measurements procedures, because they have a great effect on the performance of the solar air heater.

The test device was a solar air heater (SAH) with a single pass designed and manufactured from locally available materials at the technological hall in Mohamed Khider University of Biskra, Algeria, whose latitude is 34°48'N and longitude 5°44'E. The experiments were performed during the period from 29/05/18 to 09/06/18 where the readings were made on very sunny days with sometimes cloudy periods. The daily experimental results of temperatures, global solar radiation have been measured while the solar air heater is oriented due south, with an inclination angle of 34.48°.

## II.2. EXPERIMENTAL MODEL DESIGN

The solar air heater device is made of a simple rectangular wooden channel, the main dimensions of the solar heater were: length 1500 mm, width 750 mm and air flow duct height of 25 mm.

Figure ***II-1***,2 show a photograph and schematic diagram of experimental set-up of the constructed SAH system.

The system consists of the following main parts: a glass cover, an air gap, an absorber plate coated in black paint to increase its absorbance, an air channel where the heated air circulates, and a well-insulated bottom plate and the right and left sides to minimize energy losses. The thermo-physical properties of the components are given in Table II-1.

- The cover was a clear single glass with thickness of 5 mm, transmitance of 88%, solar absorptivity of 0.06 and emissivity of 0.93.
- The air gap between the glass cover and the absorber was airtight with a thickness of 30 mm and solar absorptivity of 0.95, emissivity of 0.95.
- The absorber plate with a thickness of 0.5 mm.
- The ventilated air duct was 25 mm thick, with the inlet at the bottom and the outlet at the top.
- The bottom plate had a 40 mm polystyrene insulation.

**Figure II-1**: Photograph of experimental set-up

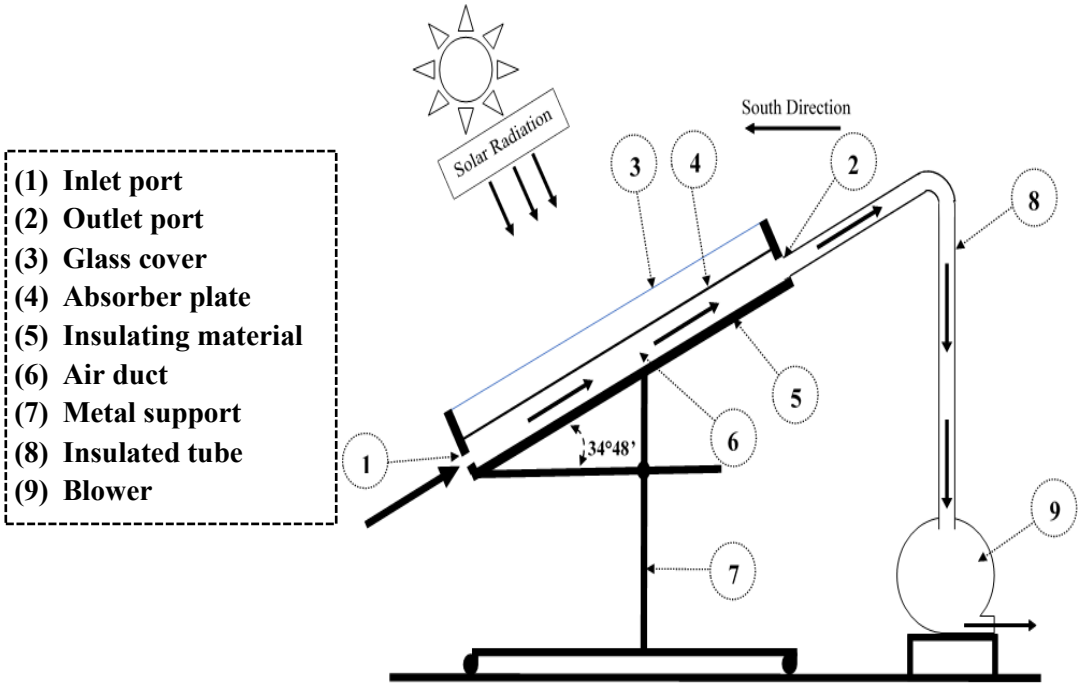


**Figure II-2:** A schematic diagram of experimental set-up

The baffles are made from aluminum alloys of rectangular shapes, placed and staggered on the bottom plate of the air channel. The rectangular baffles, were 20 mm high (e), 60 mm wide (w), 0.5 mm thick, the

spacing between baffles lines (p) was 50 mm and the spacing interbaffles in the same line was 30 mm. The studied as shown in Figure II-3.

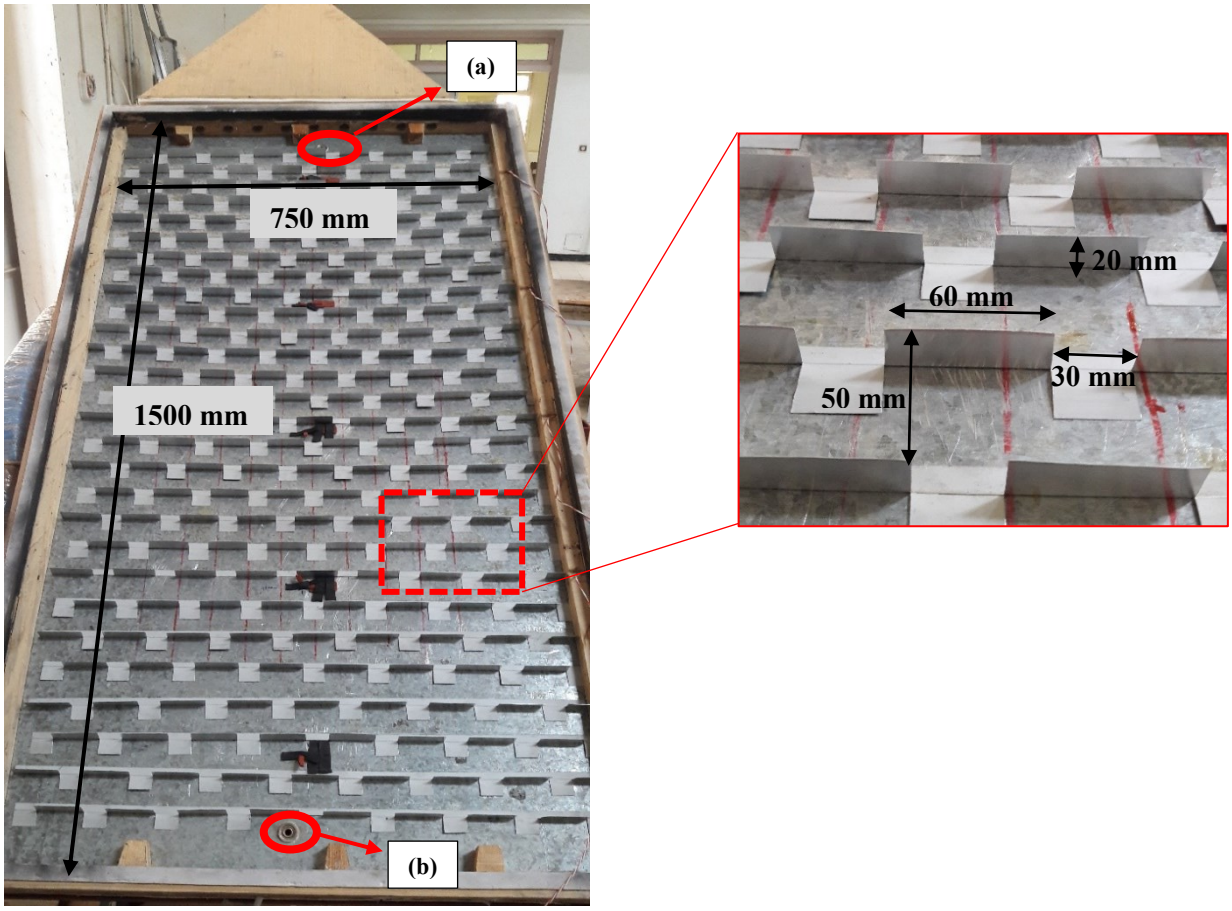


**Figure II-3:** Dimensions of experimental set-up and baffles

### II.2.1. Description of cases

In this work, we used four cases with changing the positions and arrangements and a smooth plate as the reference case. All the cases are presented in Figure II-4 The configurations are as follows:

- Smooth case: without baffles, as the reference case.
- Case 1: baffles positioned in the second half of the air channel “50% Up”.
- Case 2: baffles positioned in the first half of the air channel “50% Down”.
- Case 3: baffles positioned in the middle of the air channel “50% Middle”.
- Case 4: baffles positioned in all the air channel “100%”.

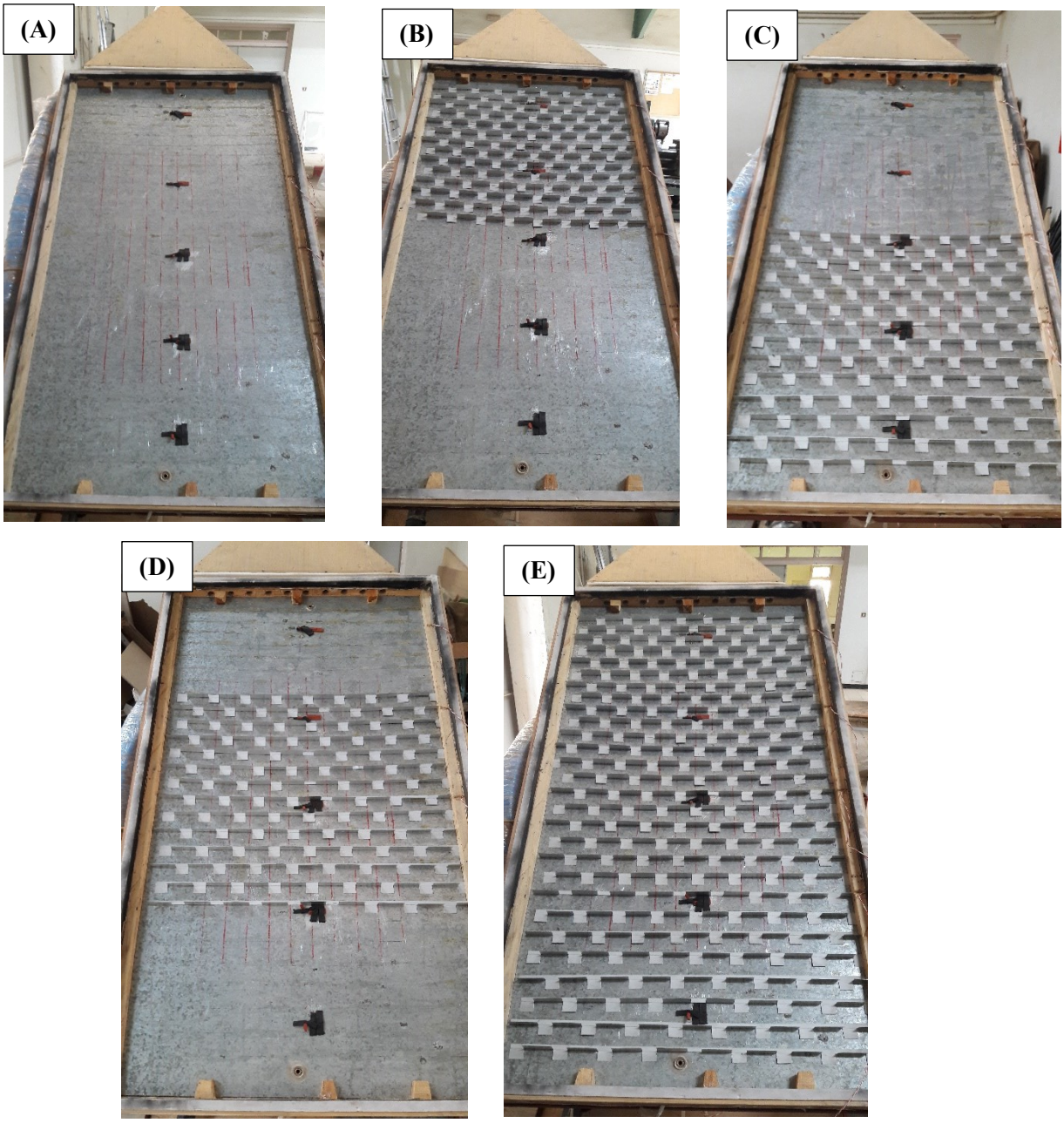


**Figure II-4:** Studied cases of solar air heater and dimensions: (A) Smooth plate (without Baffles); (B) Case 1(50% Up); (C) Case 2(50% Down); (D) Case 3(50% Middle); (E) Case 4(100%).

**Table II-1:** The thermo-physical properties of the components

| Component | Materials | Density, ρ [kg/m$^3$] | Thermal conductivity, λ [W/mK] | Specific heat, Cp [J/kgK] |
|---|---|---|---|---|
| Transparent cover | Glass | 2700 | 0.93 | 840 |
| Absorber | Galvanized steel | 7850 | 60 | - |
| Bottom | Polystyrene | 15 – 30 | 0.025 – 0.040 | 1450 |

## II.3. EXPERIMENTAL PROCEDURE, MEASUREMENT AND HEAT TRANSFER CALCULATION

The follow of measurable necessary parameters evolution for our experimental study has been done in accordance with the recommendations of ASHRAE 93-77 [81] to test the solar collectors operating in open loop circulation mode. All measuring instruments have been calibrated. The tests are carried out in transient mode to collect the relevant data on heat transfer and friction. The test data of the SAHs were recorded every 30 min, the tests starting at 9 am and ending at 3 pm.

The parameters measured in the experiments were: collector inlet temperature, collector outlet temperature, ambient temperature, air velocity and pressure in the duct, solar radiation intensity, wind velocity and the electric power consumed by the blower.

To prevent leakage, it's important to check the whole device before starting the experiment each time. The air leaks through cracks between surfaces or through the holes of the measuring sensors pass are prevented by silicone withstanding high temperatures.

### II.3.1. Temperature measurement

The air temperature was measured at the inlet and outlet of the test section. The temperature was measured at the nineteen points where the thermocouples were positioned on the absorber plate, air duct and bottom plate, at identical positions along the direction of flow as shown in Figure II-5.

The thermocouples of Pt100 Type to IEC 751 Class B with 04 wires (Figure II-6 (a)) attached in Thermocouples Input Module NI 9213 16-Ch (Figure II-6 (b)), where it is connected with Data Acquisition type 'Chassis Compact DAQ-9188-8 Slot Usb' (Figure II-6 (c)) which converted automatically the voltage signal into temperature.

Data Acquisition has 8 Thermocouple Input Module and each Thermocouple Input Module has 4 thermocouples.

Using the Data Acquisition, the temperature values are recorded during the experiments, by means of an interface of installed software NI-LabVIEW Signal Express on a computer as shown in Figure II-7.

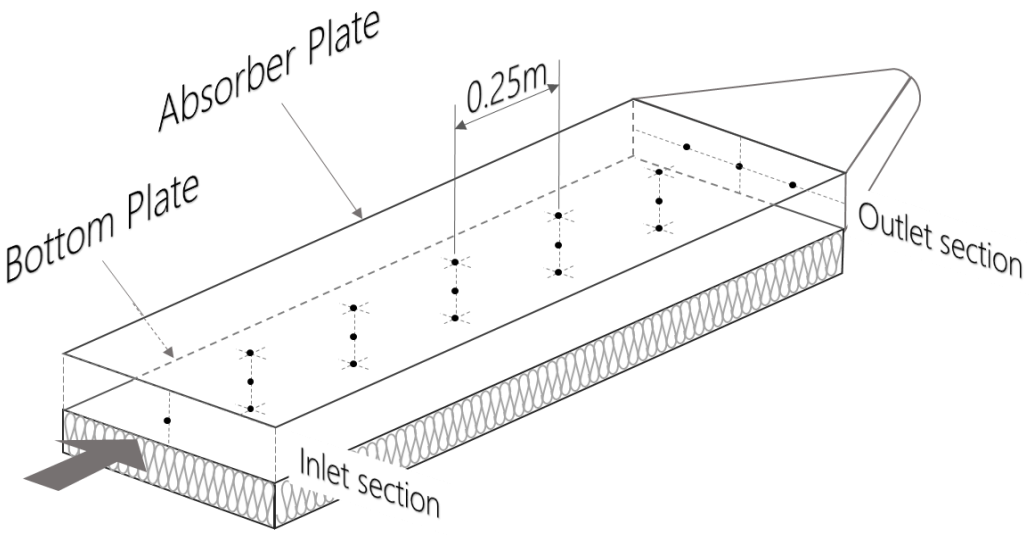


**Figure II-5:** View of thermocouples position for absorber plate, air duct, bottom plate, inlet and outlet sections

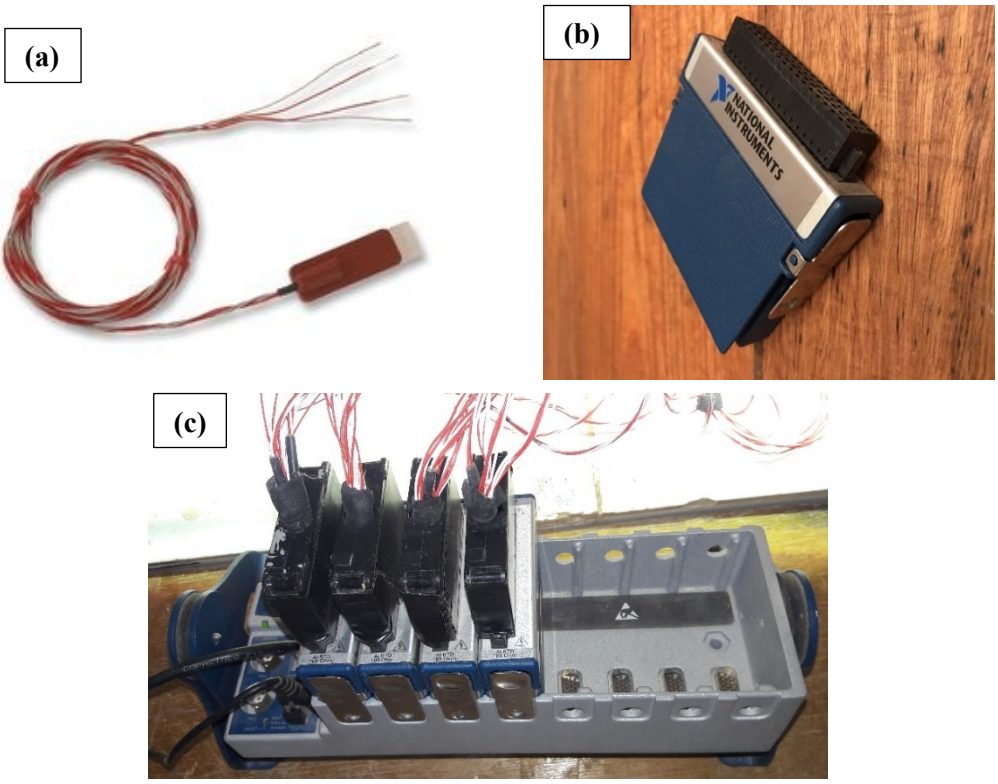


**Figure II-6:** Photographs of (a) Thermocouple Pt100 type with 4 wires, (b) Thermocouple Input Module, (c) Connected Data Acquisition

The measured values are presented as curves and as values in tables format which makes reading and storing the collected data easily and separately, it is mentioned that the data acquisition is programmed manually so the data will be taken and recorded automatically during known time intervals.

Figure II-7 shows the interface of installed software NI-LabVIEW Signal Express on a computer in working day with clarification of the necessary parts on the interface for understanding and reading easily, parts are given as follow:

**(a)** Temperatures measured curves corresponding thermocouples number.

**(b)** Recording button.

**(c)** Temperatures measured values corresponding thermocouples number.

**(d)** Thermocouples input module.

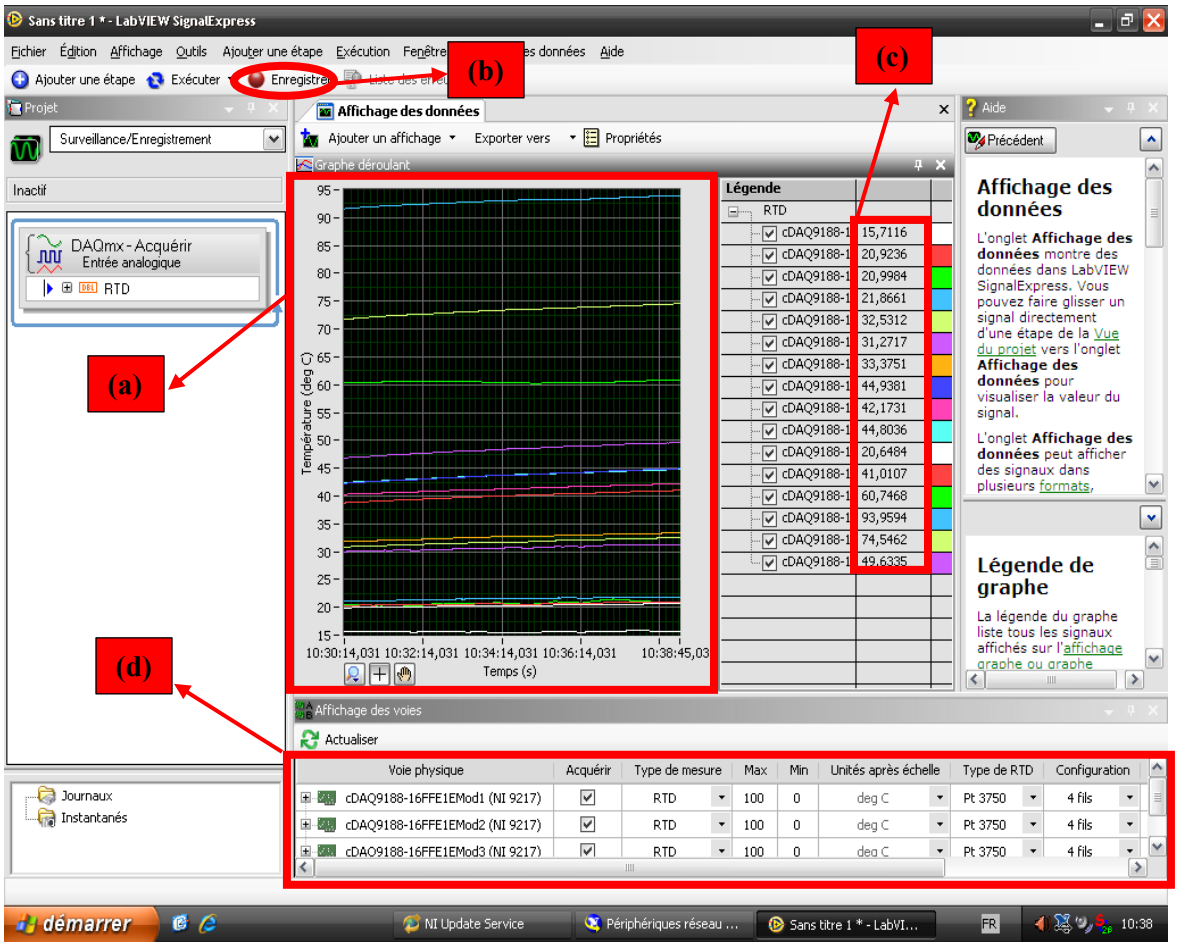


**Figure II-7:** visualization of the temperature measurement interface via NI-LabVIEW Signal Express acquisition

### II.3.2. Solar radiation measurement

The amount of solar radiation is the intensity of sunlight level in Watt per meter square ($W/m^2$) is the main indicator of the quality of solar radiation. The measurement of the solar radiation is ensured by Hand Pyranometer 4892.20 (Figure II-8)

This type of Pyranometer has a PV Cell which creates a potential (voltage) across the material and translates it into values on the crystal display screen under measuring range of 0-1999 $W/m^2$. The pyranometer is located beside the glass cover in the same plane of solar air heater. The temperature might have minor deviation effect on the reading which is not more than 3% in practical.


**Figure II-8:** A photograph of Manual pyranometer

### II.3.3. Air flow rate measurement

Air flow rate measurement is accomplished by a calibrated Kimo type anemometer (VT300) with hot wire as shown in Figure II-9 (a).

The anemometer is placed at outlet conduit of the solar air heater, it can display the values of the air velocity (measured range from 0 to 35 m/s), air flow and air temperature (measuring range from 20 to 80°C). The blower device "TD-MIXVENT Series TD-800" type (Figure II-9 (b)) is responsible for the variation of air flow with a maximum value of 200 $m^3/h$ and maximum electric power consumption of 120 W, where the electric power consumption is measured by Wattmeter instrument (Figure II-9 (c)) linked with the alimentation source and the blower sequentially.

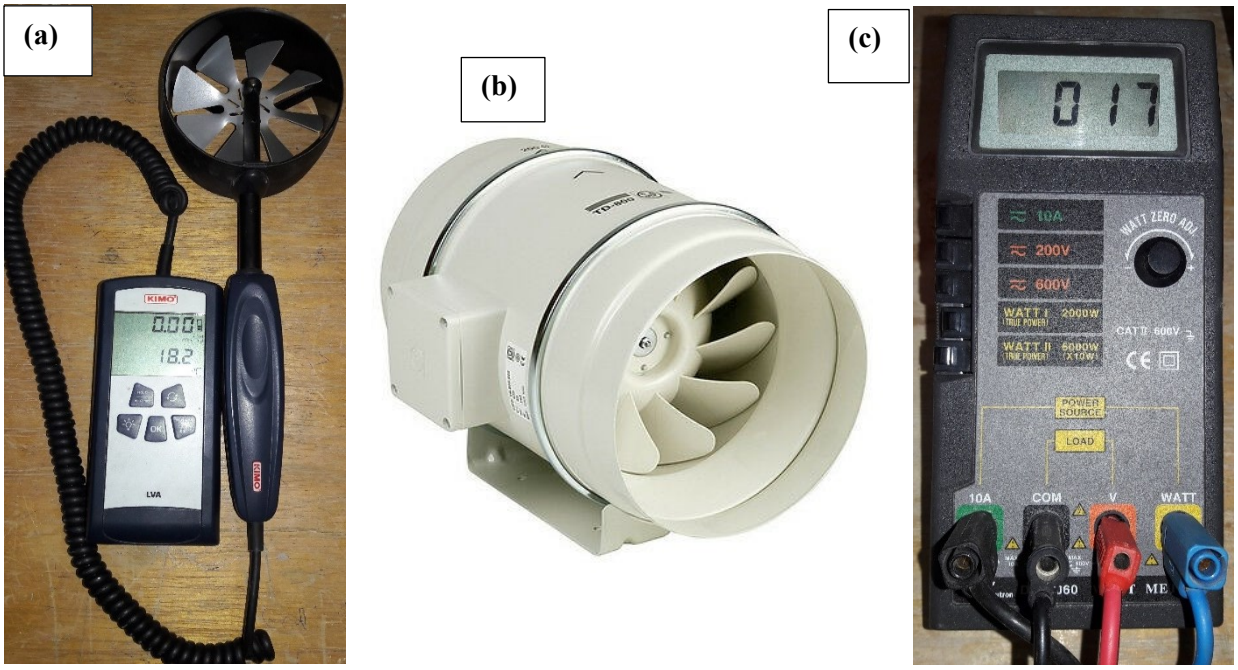


**Figure II-9:** Photographs of instruments: (a) Kimo type anemometer , (b) Blower device "TD-MIXVENT" ,(c) Wattmeter .

### II.3.4. Pressure measurement

The pressure drop across the air duct of the solar air heater was measured by a calibrated digital barometer AIRFLOW type DM3 (Figure II-10) which measures the pressure difference between two static pressure individual points placed as orifices between the outlet and inlet sections as shown in above Figure II-3 at (a) and (b) elements, respectively. The measuring ranges from $-10^5$ to $+2.10^5$ Pa.


**Figure II-10:** Digital barometer AIRFLOW type DM3

### II.3.5. Uncertainty

All experimental tests based on different instrument measures described in detail above, wherefrom important indices that should be taken into consideration are the uncertainties and errors of those instruments.

The uncertainties and errors in the measurements can result from the instruments, test planning, reading and observation, calibration, environment, instrument condition. The results are powerful tools. Table II-2 presents the occurred uncertainties.

**Table II-2:** The instruments uncertainties

| Instruments | Parameters | Uncertainty |
|---|---|---|
| Thermocouples | Temperatures (◦C) | ±0.1 |
| Pyranometer | Solar radiation (w/m$^2$) | ±1 |
| Anemometer | Flow rate (m$^3$/h) | ±0.1 |
| Wattmeter | Electric power consumption (W) | ±2 |
| Digital barometer | Pressure droop (Pa) | ±0.1 |

### II.3.6. Heat transfer calculation

The description of the heat transfer specifically between the absorber plate and the fluid using the heat transfer parameter which represented by the local heat transfer coefficient $h_x$ based on the explanation of Moummi et al [54]. The convective heat flux from the absorber plate to the fluid is given as follow:

$$\Phi_x = h_{(x)}(T_{ab} - T_f) \quad \text{(II-1)}$$

Where

$T_{ab}$ and $T_f$ are the superficial absorber temperature and the fluid mean temperature respectively, in five X-points at t-time of air in the duct section for each distance of 0.25 m, given as an average along the absorber width L. Based on the next assumptions:

- $T_f$ depended only on X-direction and it is constant in each perpendicular section to the flow.
- The $\rho_f$ and $C_p$ are constant along the air flow.

The heat exchanged quantity by air during dt-time and per unit of length is written as:

$$dq = \rho_f \, C_p S \, dt \left[\frac{\partial T_f}{\partial t} + U \frac{\partial T_f}{\partial x}\right] dx \qquad \text{(II-2)}$$

Where

$S = l.e$ is the total cross section perpendicular to the air flow.

From Eqts II-1 and II-2

$$dq = \Phi_{\mathrm{x}} \, \mathrm{l} \, dt \mathrm{dx} \qquad \text{(II-3)}$$

So

$$\frac{h_{(x)}(T_{ab} - T_f)}{\rho_f \, C_p e} = \left[\frac{\partial T_f}{\partial \mathrm{t}} + \mathrm{U} \frac{\partial T_f}{\partial \mathrm{x}}\right] \qquad \text{(II-4)}$$

The local heat transfer coefficient $h_x$ depends on the nature of the fluid flow, the quality of contact between the absorber plate and the air, also depends on the mean temperature of fluid $T_f$ and on the absorber plate temperature. In the permanent regime, the system reaches its thermal balance, where we can write:

$$\frac{\partial T_f}{\partial \mathrm{t}} = 0 \qquad \text{(II-5)}$$

Then, the local heat transfer coefficient is estimated at a given position for different mass flow rates by the following relationship [54]:

$$h(x) = \frac{eU\rho_f C_p \frac{\partial T_f(x)}{\partial x}}{T_{ab}(x) - T_f(x)} \qquad \text{(II-6)}$$

$\frac{\partial T_f(x)}{\partial x}$ the polynomial partial derivative expression of the fluid temperature as a function of the distance x measured from the inlet of the conduit, the polynomial of fluid temperature $T_f(x)$ profile is obtained using Polyfit function by MATLAB as a function of first-order. To calculate the average velocity $U$ in the air duct for each section in all studied configurations, corresponding each x-point, we used the continuity equation, whose value found is replaced in the Eqt II-6.

## II.4. RESULTS AND DISCUSSION

The presentation of experimental results performed from May to June 2018. The examination of five configurations under climatic conditions of Biskra have been compared. all the measured parameters (the solar radiation, temperatures, pressure droop and power consumption ...) were recorded for all cases in each 30 minutes on through studied days from with a fixed and varied mass flow rate from 0.011 to 0.041 kg/s. Table II-3 and 4 present some examples of measurement produced of the measurable parameters necessary for our experimental study, such as the air temperatures at the inlet, at the outlet, at identical positions along the direction of flow, also the surface of the absorber plate and bottom plate for four different positions with distance of 0.25 m, in addition, solar radiation on the inclined collector plane, electric power consumed by the blower, mass flow rate.

Figure II-11 to II-15 show the hourly variations of the measured solar radiation, inlet and outlet temperatures of different conditions of the studied days for smooth plate and using different baffles emplacements at the bottom plate, corresponding mass flow rate of 0.017 kg/s. The maximum values of solar radiation for the studied days during the days between 30/05/2018 and 07/06/2018 are 970, 950, 975, 960 and 955 W/m², respectively, for corresponding all studied cases. The temperatures of various elements increase with time as the solar radiation increases showing their maximum values between 12:00 and 13:00 as seen in Figures.

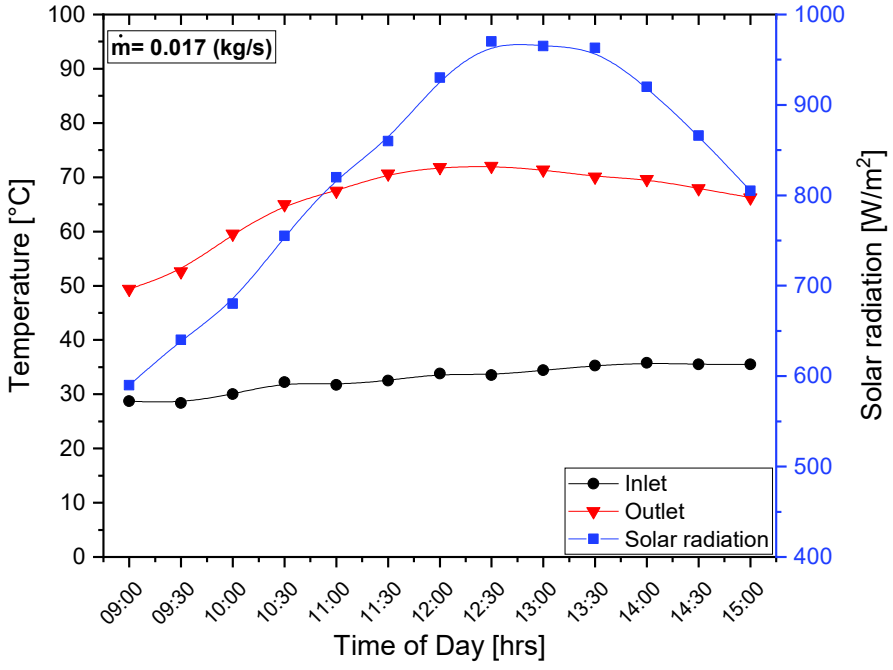


**Figure II-11:** The evolution of inlet and outlet temperatures were associated with solar radiation versus time of day for mass flow rate of m = 0.017 kg/s (30/05/2018)

**Table II-3:** The measured parameters of Smooth case for mass flow rate $\dot{m}$ = 0.017 (kg/s) (30/05/2018)

| | | | | | | | | Bottom | | | | | Air | | | | | Absorber | | | | |
|---|---|---|---|---|---|---|---|---|---|---|---|---|---|---|---|---|---|---|---|---|---|---|
| **Time** | **$I_T$** | **V(m/s)** | **ṁ(kg/s)** | **Pm(w)** | **ΔP** | **Tin** | **Tout** | **T1** | **T2** | **T3** | **T4** | **T5** | **T1** | **T2** | **T3** | **T4** | **T5** | **T1** | **T2** | **T3** | **T4** | **T5** |
| 09:00 | 582 | 1.54 | 0.017 | 36 | 0.1 | 28.7 | 49.42 | 37.03 | 41.2 | 47.36 | 50.06 | 52.57 | 41.46 | 50.95 | 55.33 | 63.37 | 60.67 | 57.24 | 70.12 | 77.17 | 78.96 | 79.65 |
| 09:30 | 668 | 1.54 | 0.017 | 36 | 0.1 | 28.4 | 52.62 | 38.25 | 42 | 48.63 | 51.98 | 55.43 | 40.73 | 48.76 | 53.69 | 62.9 | 61.12 | 56.46 | 69.83 | 77.4 | 79.7 | 81.47 |
| 10:00 | 745 | 1.54 | 0.017 | 36 | 0.1 | 30 | 59.57 | 40.75 | 46.41 | 54.29 | 58.75 | 63.02 | 40.39 | 48.45 | 52.93 | 62.97 | 61.28 | 56.46 | 70.01 | 78.19 | 80.83 | 83.33 |
| 10:30 | 820 | 1.54 | 0.017 | 36 | 0.1 | 32.2 | 65.01 | 44.48 | 53.08 | 62.08 | 67.09 | 71.41 | 41.76 | 51.71 | 55.35 | 66.65 | 64.74 | 59.16 | 74.05 | 83.26 | 86.05 | 89.18 |
| 11:00 | - | - | - | - | - | - | - | - | - | - | - | - | - | - | - | - | - | - | - | - | - | - |
| 11:30 | - | - | - | - | - | - | - | - | - | - | - | - | - | - | - | - | - | - | - | - | - | - |
| 12:00 | - | - | - | - | - | - | - | - | - | - | - | - | - | - | - | - | - | - | - | - | - | - |
| 12:30 | - | - | - | - | - | - | - | - | - | - | - | - | - | - | - | - | - | - | - | - | - | - |
| 13:00 | - | - | - | - | - | - | - | - | - | - | - | - | - | - | - | - | - | - | - | - | - | - |
| 13:30 | 922 | 1.54 | 0.017 | 36 | 0.1 | 35.3 | 70.07 | 47.29 | 55.69 | 65.58 | 71.27 | 76.56 | 46.84 | 63.35 | 62.13 | 75.57 | 72.7 | 64.89 | 81.9 | 94.39 | 97.75 | 103.53 |
| 14:00 | 872 | 1.54 | 0.017 | 36 | 0.1 | 35.8 | 69.64 | 47.29 | 55.52 | 64.78 | 70.19 | 75.5 | 45.65 | 61.27 | 59.73 | 72.47 | 69.5 | 62.32 | 78.4 | 90.33 | 93.61 | 99.43 |
| 14:30 | 802 | 1.54 | 0.017 | 36 | 0.1 | 35.5 | 67.94 | 46.16 | 53.58 | 62.51 | 67.57 | 72.43 | 43.8 | 59.48 | 57.85 | 69.7 | 66.82 | 59.46 | 75.49 | 86.42 | 89.66 | 95.55 |
| 15:00 | 723 | 1.54 | 0.017 | 36 | 0.1 | 35.5 | 66.24 | 46.44 | 53.83 | 62.16 | 67.21 | 71.7 | 43.97 | 57.86 | 56.23 | 66.96 | 64.26 | 57.94 | 72.09 | 82.36 | 85.61 | 91.5 |

**Table II-4:** The measured parameters of Case 2 for different mass flow rates (07/06/2018)

| | | | | | | | | Bottom | | | | | Air | | | | | Absorber | | | | |
|---|---|---|---|---|---|---|---|---|---|---|---|---|---|---|---|---|---|---|---|---|---|---|
| **Time** | **$I_T$** | **V(m/s)** | **ṁ(kg/s)** | **Pm(w)** | **ΔP** | **Tin** | **Tout** | **T1** | **T2** | **T3** | **T4** | **T5** | **T1** | **T2** | **T3** | **T4** | **T5** | **T1** | **T2** | **T3** | **T4** | **T5** |
| 09:00 | 620 | 1.05 | 0.0116 | 23 | 2.5 | 26.7 | 26.4 | 34.64 | 45.14 | 55.76 | 55.83 | 54.84 | 35.59 | 47.86 | 58.43 | 63.9 | 62.13 | 49.63 | 59.99 | 69.3 | 75.73 | 76.6 |
| 09:30 | 680 | 1.15 | 0.0127 | 26 | 3.7 | 26.7 | 26.5 | 35.03 | 46.49 | 56.89 | 58.36 | 58.71 | 35.97 | 47.08 | 58.85 | 65.69 | 64.74 | 49.54 | 59.78 | 70.23 | 79.13 | 81.14 |
| 10:00 | 735 | 1.31 | 0.0144 | 27 | 4 | 26.6 | 26.5 | 35.65 | 47.86 | 59.74 | 60.92 | 61.56 | 37.08 | 50.82 | 62.7 | 69.4 | 68.68 | 52.87 | 64.09 | 74.8 | 83.17 | 85.2 |
| 10:30 | 855 | 1.48 | 0.0163 | 32 | 6.2 | 28.4 | 27.3 | 36.77 | 50.07 | 64.3 | 66.03 | 68.2 | 38.28 | 54.13 | 67.07 | 75.12 | 75.88 | 55.63 | 67.54 | 80.08 | 90.78 | 93.87 |
| 11:00 | - | - | - | - | - | - | - | - | - | - | - | - | - | - | - | - | - | - | - | - | - | - |
| 11:30 | - | - | - | - | - | - | - | - | - | - | - | - | - | - | - | - | - | - | - | - | - | - |
| 12:00 | - | - | - | - | - | - | - | - | - | - | - | - | - | - | - | - | - | - | - | - | - | - |
| 12:30 | - | - | - | - | - | - | - | - | - | - | - | - | - | - | - | - | - | - | - | - | - | - |
| 13:00 | - | - | - | - | - | - | - | - | - | - | - | - | - | - | - | - | - | - | - | - | - | - |
| 13:30 | 952 | 2.96 | 0.0327 | 43 | 15.4 | 33.5 | 32.4 | 40.75 | 52.95 | 66.98 | 71.02 | 74.68 | 41.91 | 57.41 | 69.12 | 80.28 | 81.25 | 57.45 | 69.56 | 81.88 | 96.32 | 100.01 |
| 14:00 | 900 | 3.29 | 0.0364 | 53 | 18.7 | 33.7 | 32.7 | 39.08 | 50.69 | 63.66 | 67.85 | 71.69 | 40.75 | 54.61 | 65.32 | 75.94 | 77.06 | 54.91 | 66 | 77.08 | 91.21 | 95.06 |
| 14:30 | 835 | 3.62 | 0.04 | 70 | 20 | 33.7 | 32.8 | 38.79 | 49.16 | 61.02 | 64.93 | 68.69 | 40 | 52.74 | 62.56 | 72.39 | 73.34 | 53.09 | 63.25 | 73.31 | 86.84 | 90.42 |
| 15:00 | 817 | 3.71 | 0.041 | 71 | 20.2 | 33.6 | 32.7 | 37.55 | 48 | 60.33 | 62.14 | 66.28 | 38.7 | 51.1 | 61.85 | 70.05 | 71.7 | 52.11 | 60.44 | 71 | 82.17 | 86.2 |

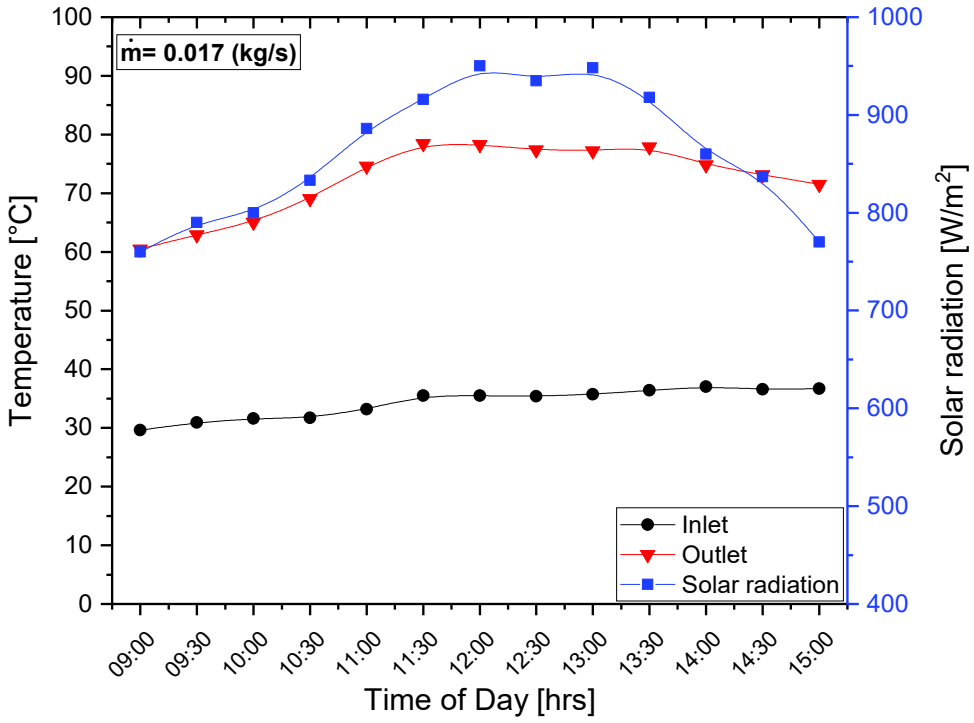


**Figure II-12:** The evolution of inlet and outlet temperatures were associated with solar radiation versus time of day for mass flow rate of m = 0.017 kg/s (31/05/2018)

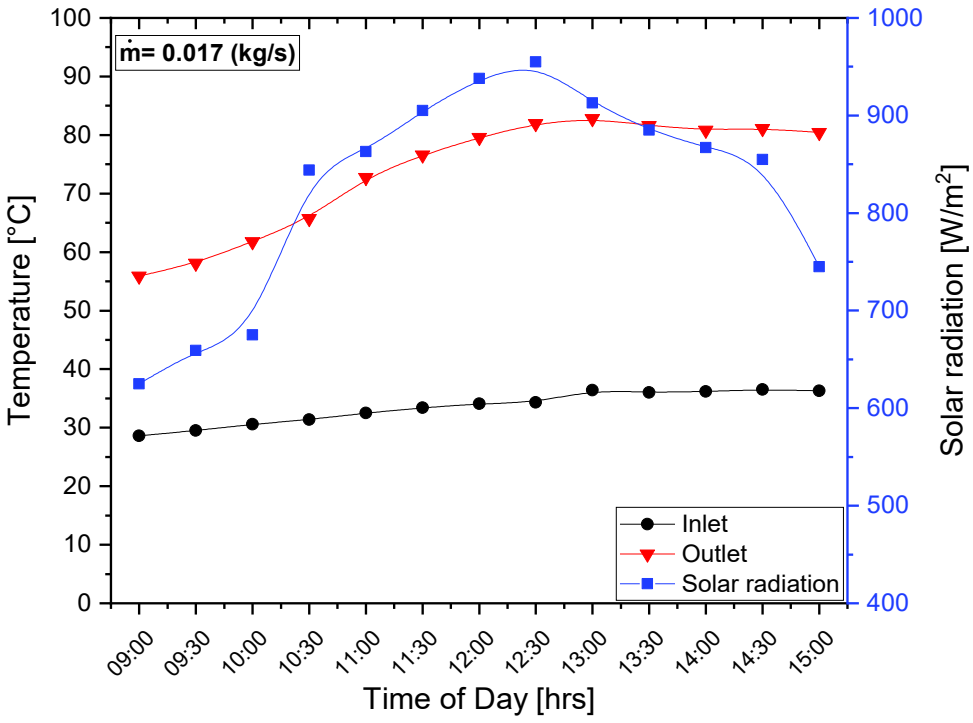


**Figure II-13:** The evolution of inlet and outlet temperatures were associated with solar radiation versus time of day for mass flow rate of m = 0.017 kg/s (04/06/2018)

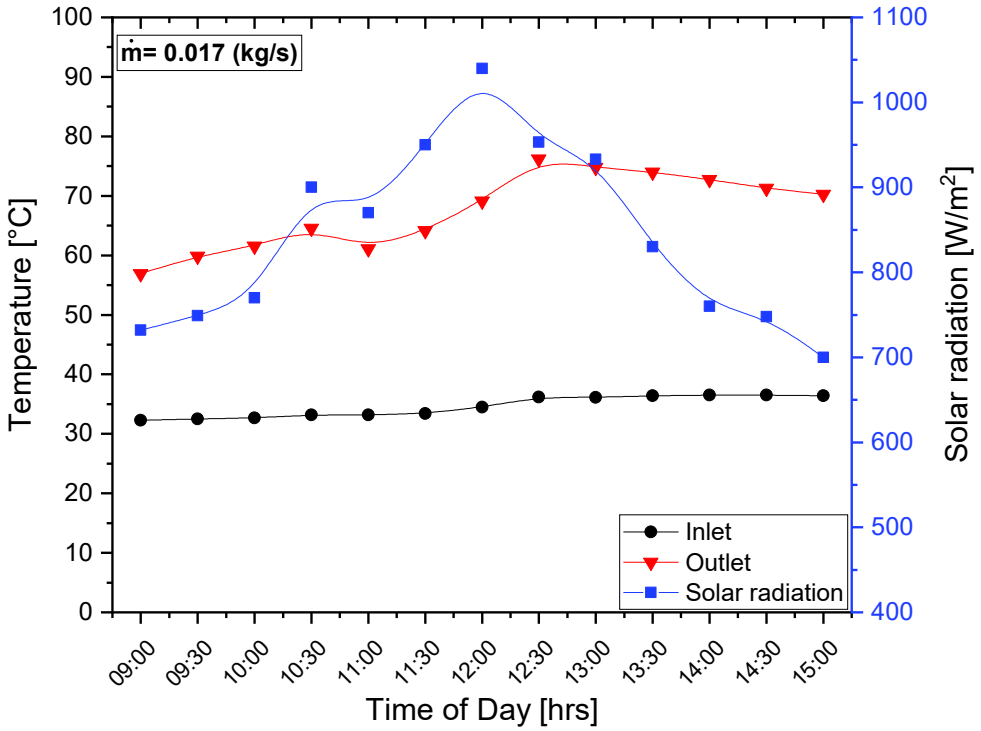


**Figure II-14:** The evolution of inlet and outlet temperatures were associated with solar radiation versus time of day for mass flow rate of m = 0.017 kg/s (07/06/2018)

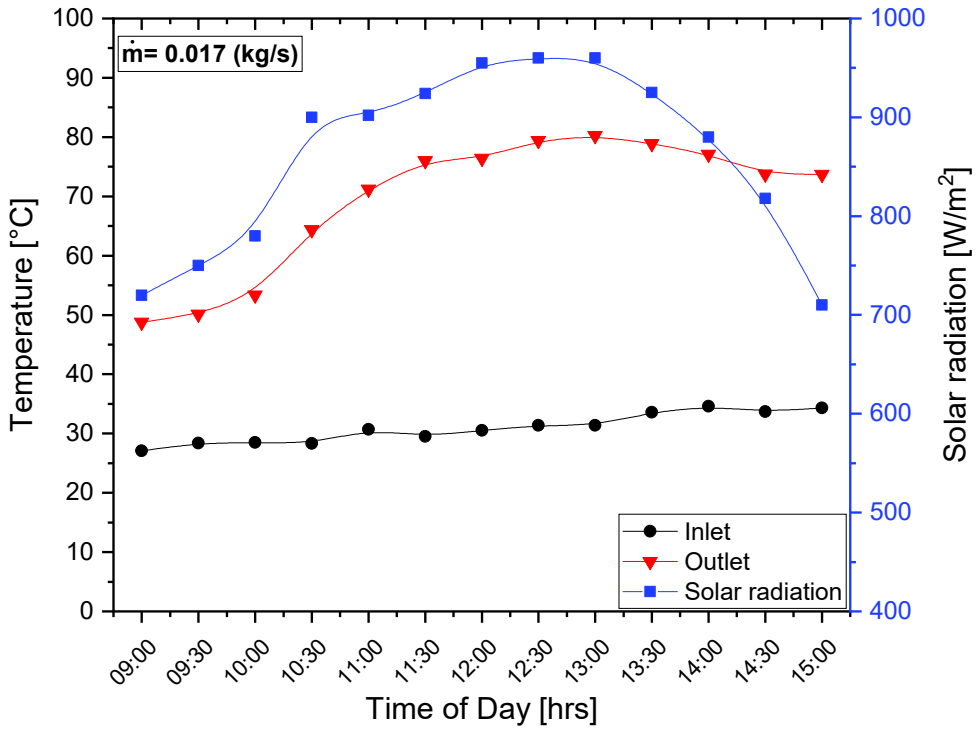


**Figure II-15:** The evolution of inlet and outlet temperatures were associated with solar radiation versus time of day for mass flow rate of m = 0.017 kg/s (08/06/2018)

Figures II-16 to II-20 show the measured temperatures of air, absorber and bottom plates were associated with the estimated local heat transfer coefficient versus the SAH length, from 0 to 1.5 m, corresponding the studied cases, smooth case, case 1, case 2, case 3, case 4, respectively. The temperatures values were measured in five points (distance between each point is 0.25 m) along the length of the air duct from the inlet cross section to the outlet after the test section.

The local heat transfer coefficient was estimated based on the relationship (Eqt II-6) of Moummi et al. [54] which has been demonstrated previously in section (II.3.6) at a given position or point. The studied cases with baffles and their different positions have a great effect on the temperatures of air, absorber and bottom plates where the local heat transfer coefficient describes that.

Figure II-16 illustrates the air temperature, absorber temperature, bottom temperature and local heat transfer coefficient of the smooth case (without roughness), with the length of SAH for air mass flow rate of 0.017 kg/s. This figure gives clear indications of the relationship between the local heat transfer coefficient and the temperature difference between the absorber plate and the fluid (air), where the increase of local heat transfer coefficient is based on temperature difference decreases as presented in the points 0.25, 0.5 and 1 m. Also, the opposite, where the decrease of local heat transfer coefficient is based on temperature difference increases as presented in the points 0.75 and 1.25 m.

Figure II-17 shows the air temperature, absorber temperature, bottom temperature and local heat transfer coefficient of the Case 1 (50%Up), with the length of SAH for air mass flow rate of 0.017 kg/s. In this case, there are two parts the first one from 0 to 0.75 m represents the smooth part (without baffles), the second part from 0.75 to 1.5 m represents the baffled part. The local heat transfer coefficient curve decreases in the smooth part from 0.25 to 0.75 m and suddenly increases dramatically at the baffled part until the point 1.25 m. From another side, the temperature difference between the air and absorber plate follows reversibly the same behavior of the heat transfer coefficient. So, the baffles have a great effect on heat transfer.

The air temperature, absorber temperature, bottom temperature and local heat transfer coefficient of the Case 2 (50%Down), with the length of SAH for air mass flow rate of 0.017 kg/s as shown in Figure II-18, this case has two parts the first one from 0 to 0.75 m represents the baffled part, the second part from 0.75 to 1.5 m represents the smooth part (without baffles). The local heat transfer coefficient curve increases at the baffled part from 0.25 to 0.5 m and decreases gradually until the end of the smooth part. From another side, the temperature difference between the air and absorber plate follows reversibly the same behavior of the heat transfer coefficient, where the maximum temperature difference between the air and the absorber plate in the point 1.25 m corresponding to the minimum local heat transfer coefficient value.

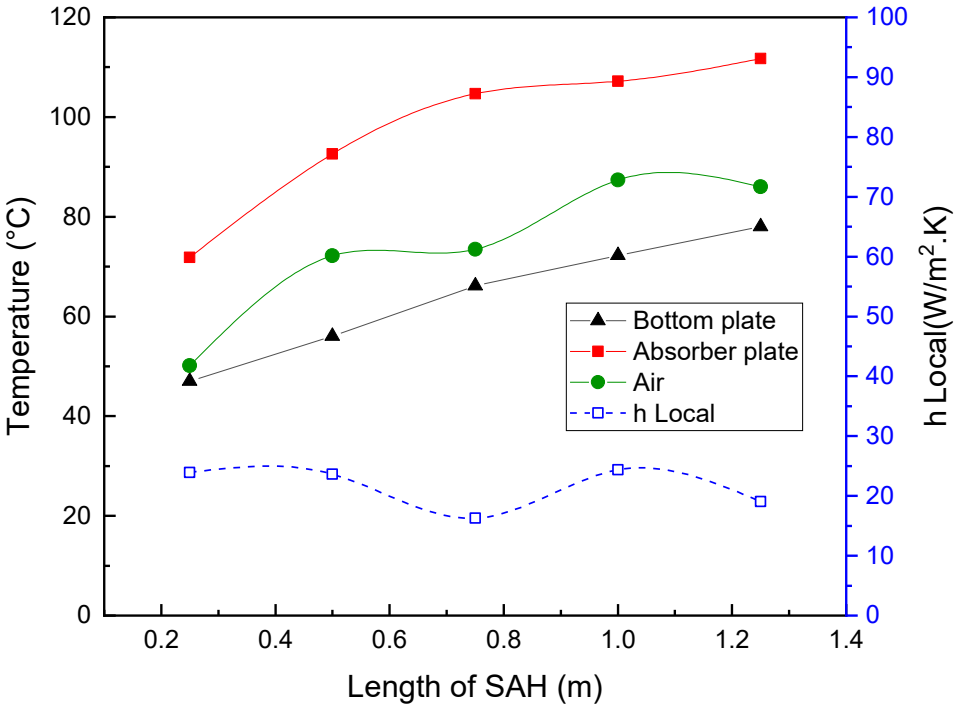


**Figure II-16:** The evolution of air, absorber and bottom temperatures were associated with local heat transfer coefficient versus length of SAH for Smooth case at $\dot{m}$ = 0.017 kg/s

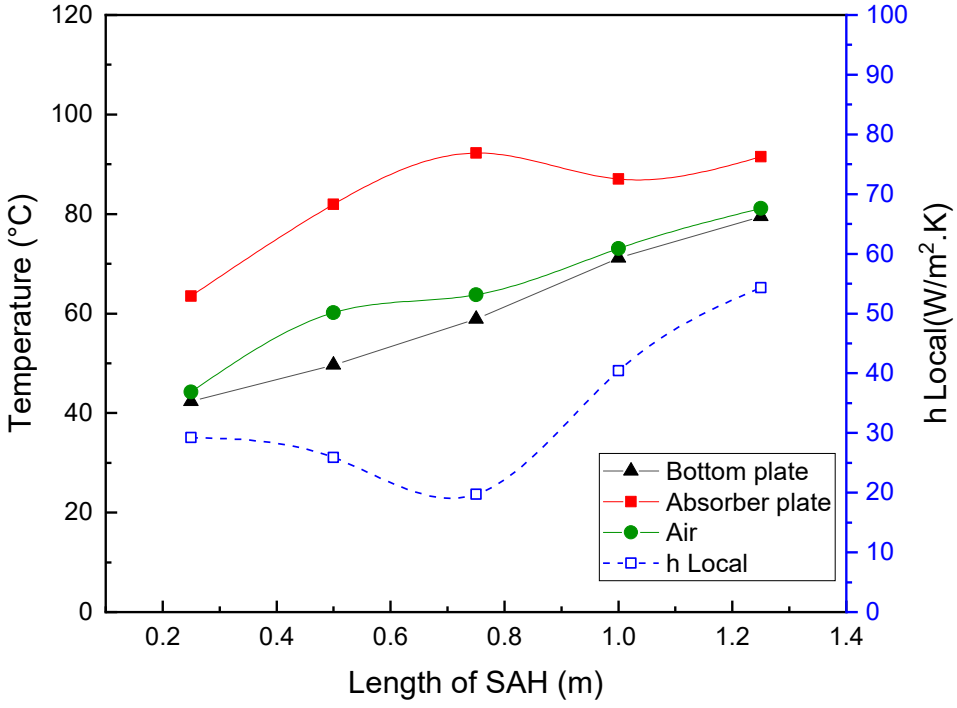


**Figure II-17:** The evolution of air, absorber and bottom temperatures were associated with local heat transfer coefficient versus length of SAH for Case 1 at $\dot{m}$ = 0.017 kg/s

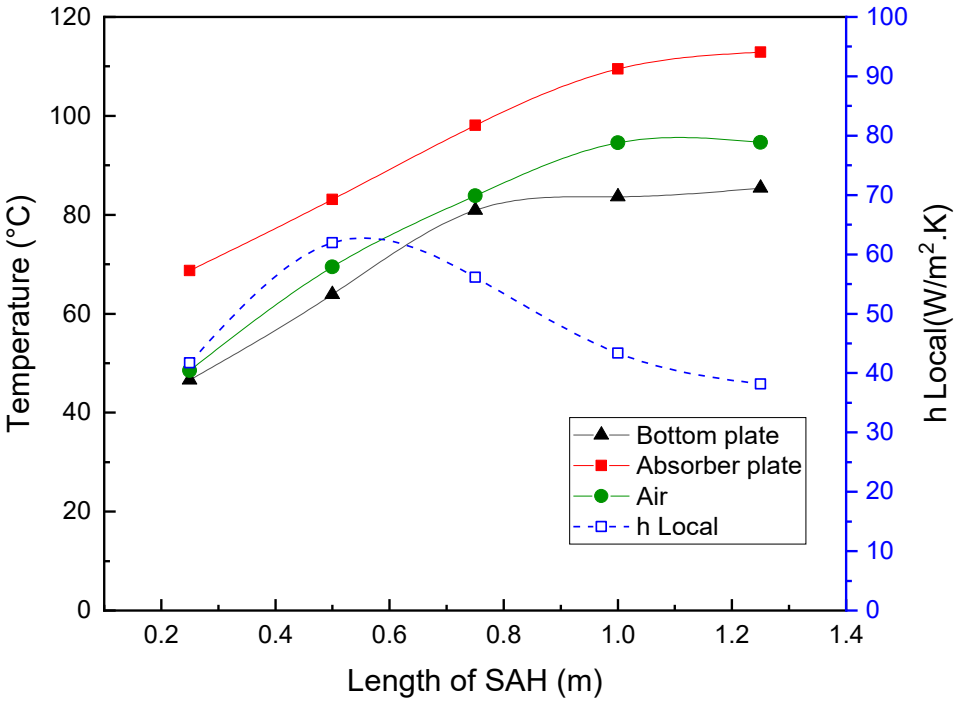


**Figure II-18:** The evolution of air, absorber and bottom temperatures were associated with local heat transfer coefficient versus length of SAH for Case 2 at $\dot{m}$ = 0.017 kg/s

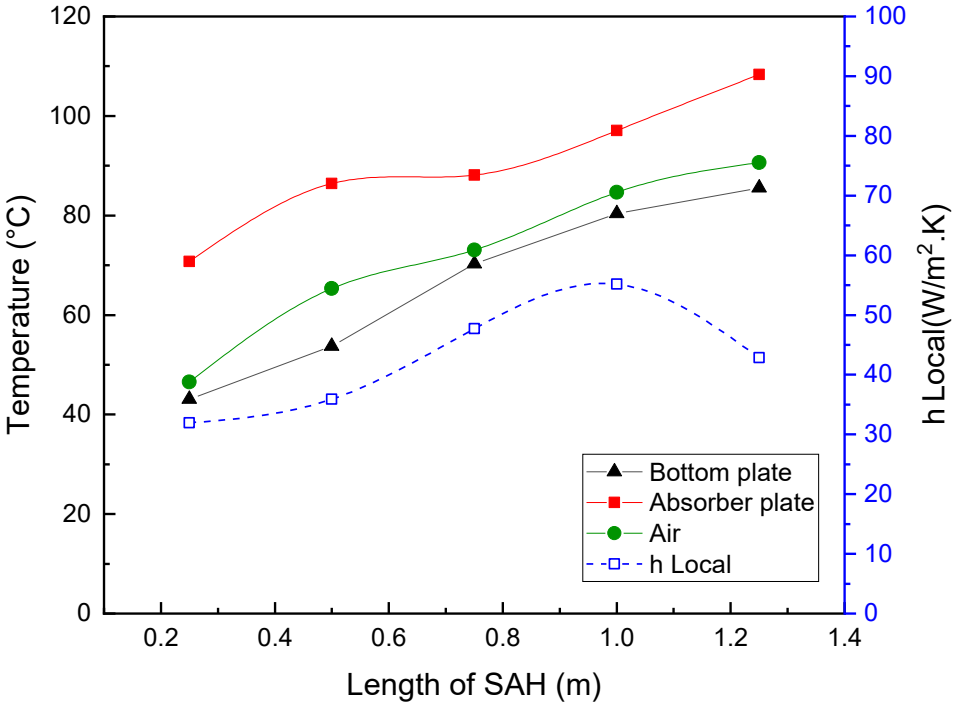


**Figure II-19:** The evolution of air, absorber and bottom temperatures were associated with local heat transfer coefficient versus length of SAH for Case 3 at $\dot{m}$ = 0.017 kg/s

Figure II-19 shows the air temperature, absorber temperature, bottom temperature and local heat transfer coefficient of the Case 3 (50% Middle), with the length of SAH for air mass flow rate of 0.017 kg/s. This case divided into three parts the first one from 0 to 0.5 m represents the smooth part (without baffles), the second part from 0.5 to 1 m represents the baffled part, the last part is the smooth part from 1 to 1.5 m (without baffles).

The local heat transfer coefficient increases slightly at the smooth part from 0.25 to 0.5 m and increases gradually to the maximum at the point of 1 m corresponding to the end of the baffled part, after that decreases with the beginning of the smooth part from 1 to 1.25. From another side, the temperature difference between the air and absorber plate follows reversibly the same behavior of the local heat transfer coefficient, where the minimum temperature difference between the air and the absorber plate in the point of 1 m corresponding the maximum local heat transfer coefficient value.

Case 4 (100%) is full of baffles. The variation of air, absorber, bottom temperatures and the estimated local heat transfer coefficient versus the length of SAH for air mass flow rate of 0.017 kg/s are presented in Figure II-20. The local heat transfer coefficient decreases gradually until the end of air duct. From another side, the temperature difference between the air and absorber plate increases slightly until the end of air duct.

Based on the different configurations corresponding to different baffles positions, the approximate comparison between the studied Cases has been done in Figure II-21. the comparison is made on the local heat transfer coefficient versus the air duct length of the solar air heater at the mass flow rate of 0.025 kg/s.

It can be observed from this figure that their maximum local heat transfer coefficient is always located at the baffled part of the studied system regardless of the mass flow rate value, the lower values of local heat transfer coefficients are obtained from the smooth case (without baffles) and the highest values are obtained from the Case 4 (with baffles).

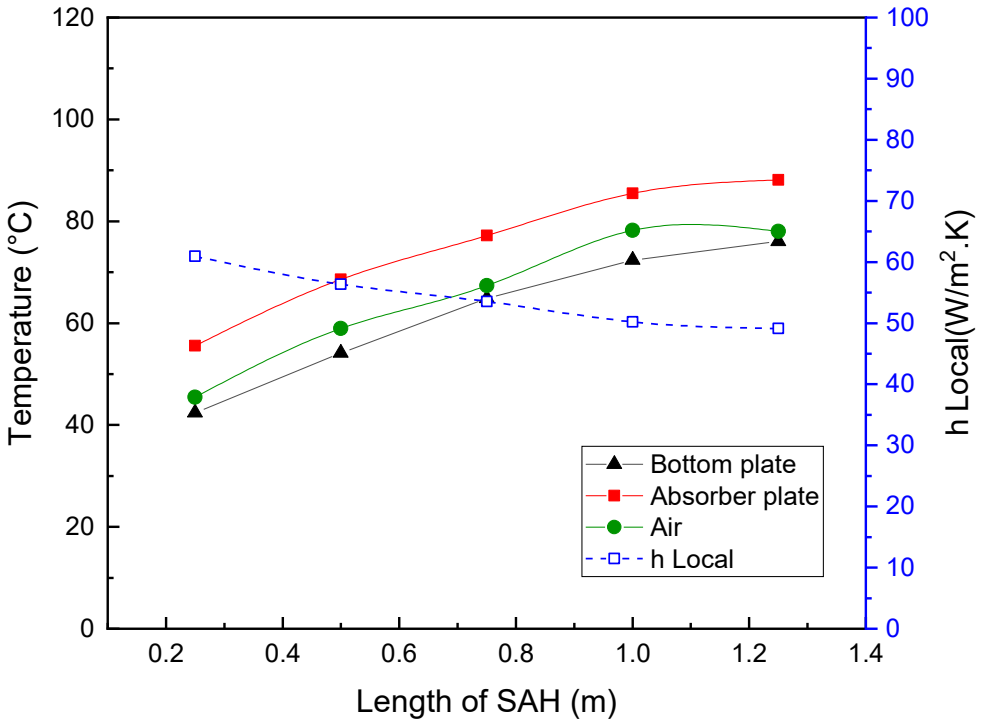


**Figure II-20:** The evolution of air, absorber and bottom temperatures were associated with local heat transfer coefficient versus length of SAH for Case 4 at $\dot{m}$ = 0.017 kg/s

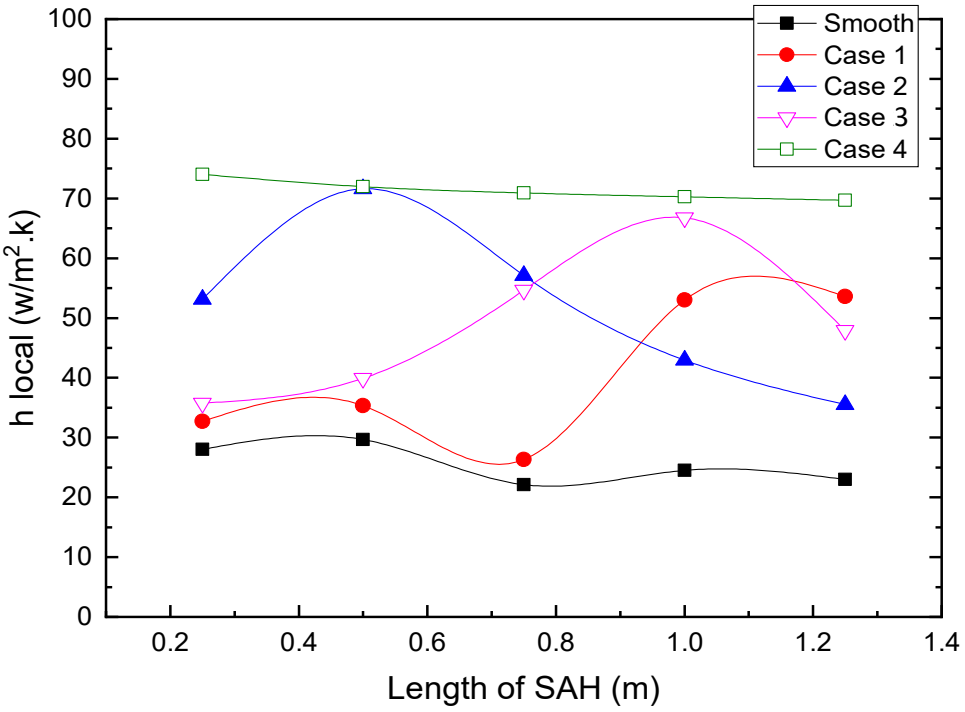


**Figure II-21:** The evolution of local heat transfer coefficient versus length of SAH for all Cases at $\dot{m}$ = 0.025 kg/s

## II.5. CONCLUSION

In this chapter, the solar air heater description, the five studied cases including conventional case (smooth) and the baffles type construction and fabrication have been presented, also the procedure of the experimental process has been described. The evolution of the measurable parameter for our experimental study has been done in accordance with the recommendations of ASHRAE 93-77 [81] to test the system operating. The instruments of measurements and its uncertainties to ensure that the measured parameters are reliable.

The experimental results have presented that the baffled cases are more efficient than the smooth case. In comparison with baffled cases and smooth duct, the baffled cases prove their reliability in increasing heat exchange. The presented configurations can be utilized for the SAHs enhancement.

# *CHAPTER III*
# *NUMERICAL STUDY*

## III.1. INTRODUCTION

In this chapter, a numerical model based on computational fluid dynamics (CFD) was developed based on the geometry of the experimental test model. Computational Fluid Dynamics or CFD is the analysis of systems involving fluid flow, heat transfer and associated phenomena such as chemical reactions by means of computer-based simulation. The technique is very powerful and spans a wide range of industrial and non-industrial application areas as:

- Aerodynamics of aircraft and vehicles
- Hydrodynamics of ships
- Electrical and electronic engineering
- Energy flows
- Biomedical engineering
- Chemical process engineering

There are several numerical methods in order to obtain solutions to such issues: finite difference, finite element and finite volume methods. The equations governing the fluid flow are the continuity (conservation of mass), the Navier–Stokes (balance of momentum), and the energy (conservation of energy) equations.

The geometry of the configuration considered, the modeling equations, the simplifying assumptions, and the boundary conditions appropriate to the turbulent flow within a rectangular duct is presented. During the geometry construction, four steps are followed: the geometry definition, the mesh and its verification, the boundary conditions definition and definitions of the calculation fields.

The developed CFD models to assess the influence of different positions of the baffles on the thermo-hydraulic performance under different boundary conditions were used the heat flux imposed on the absorber plate, inlet air temperature and adiabatic conditions at the bottom plate and side walls. The geometry and mesh construction with GAMBIT 2.4.6, the resolution and processing with ANSYS FLUENT 15.0.

## III.2. NUMERICAL METHODOLOGY

The numerical model based on CFD was developed based on the geometry of the experimental test model, grid independency and the turbulence model were analysed. This numerical model was developed and carried out under the defined assumptions. In a first stage, the computational model was experimentally validated and, in a second stage, the model was used to assess the influence of different positions of the baffles on the thermo-hydraulic performance under diferent boundary conditions.

For the experimental validation of the numerical model, the boundary conditions were the temperature imposed on the absorber and bottom plates of the air channel, and that of the air at the inlet section.

All these values were taken from the experimental campaign. The results obtained with the numerical model in terms of local air temperature at different points from the inlet to the outlet of the solar air heater were compared with the experimental ones for two different mass flow rate values.

After the experimental validation of the numerical CFD model, it was used to assess the influence of the position of the baffles on the thermal and hydraulic performance of the solar air heater. In each studied case, the same boundary conditions were used: heat flux imposed on the absorber plate, inlet air temperature and adiabatic conditions at the bottom plate and side walls.

For six different mass flow rate values, the results in terms of local convective heat transfer coefficient, friction factor, thermo-hydraulic performance factor (THPF) and thermal efficiency were compared to determine the best solar air heater configuration from a thermal and hydraulic point of view. The flow-diagram in the introduction which shows the methodology description followed in this work.

CFD codes are structured about the numerical algorithms that can tackle fluid flow problems. In order to provide their solving power easly, all commercial CFD packages include sophisticated user interfaces to input problem parameters and to examine the results. Hence all codes contain three main elements: (1) a pre-processor, (2) a solver and (3) a post-processor. We briefly examine the function of each of these elements within the context of a CFD code.

**(1) Pre-processor**

Pre-processing contains of the studied problem input to a CFD program by means of an operator-friendly interface and the subsequent transformation of this input into a form suitable for use by the solver.

The pre-processing stage consists :

- The geometry definition of the interest region : the computational domain.
- Grid generation : a grid (or mesh) of cells (or control volumes or elements).
- Definition of fluid properties.
- Specification of the boundary conditions.

**(2) Solver**

There are three deffrent streams of numerical solution techniques: finite difference, finite element and spectral methods. We are solely concerned with the finite volume method, a special finite difference formulation that is central to the most well-established CFD codes: CFX/ANSYS and FLUENT. The numerical algorithm consists of the following steps:

- Integration of the governing equations of fluid flow over all the control volumes of the domain.
- Discretization-conversion of the resulting integral equations into a system of algebraic equations.

- Solution of the algebraic equations by an iterative method.

The first step, the control volume integration, distinguishes the finite volume method from all other CFD techniques. Commercial codes may also give the user a selection of further, more recent, techniques such as Gauss–Seidel point iterative techniques with multigrid accelerators and conjugate gradient methods.

**(3) Post-processor**

As in pre-processing, a huge amount of development work has recently taken place in the post-processing field. Due to the increased popularity of engineering workstations, many of which have outstanding graphics capabilities, the leading CFD packages are now equipped with versatile data visualization tools. The post-processing can presents the tools to visualize the outcomes as the following:

- Domain geometry and grid display
- Vector plots
- 2D and 3D surface plots
- Particle and fluid movment tracking
- View manipulation (translation, rotation, scaling etc.)

More recently these facilities may also include animation for dynamic result display, and in addition to graphics all codes produce trusty alphanumeric output and have data export facilities for further manipulation external to the code.

The CFD approach has many advantages as substantial reduction of lead times and costs of new designs, ability to study systems where controlled experiments are difficult or impossible to perform (e.g., very large systems), ability to study systems under hazardous conditions at and beyond their normal performance limits (e.g., safety studies and accident scenarios), practically unlimited level of detail of results, complicated physics can be treated and time evolution of flow can be obtained. Also, without forget the Disadvantages as truncation errors, boundary conditions problems and computer costs.

## III.2.1. Geometry and cases descriptions

The solar air heater geometry is shaped of a simple rectangular channel, the main geometry dimensions were: length 1500 mm, width 750 mm and air flow duct height of 25 mm.

We used four baffled cases with changing the positions and arrangements and a smooth plate as the reference case, the baffles are located successively at the bottom plate of the unheated wall in the form of rectangular shape, were 20 mm high (e), 60 mm wide (w), 0.5 mm thick and the interbaffle spacing (p) was 50 mm, the spacing interbaffle in the same line was 30 mm.

The geometry, studied cases and baffles dimensions are presented in Figure III-1 . Four different cases were analyzed depending on the position of the baffles in the device: in case 1, the baffles were located in the second half of the air channel; in case 2, in the first half of the air channel; in case 3, in the middle of the air channel; and in case 4, throughout the whole air channel. In addition, a case without baffles was considered for comparison purposes, the configurations are as follows:

- Smooth case: without baffles, as the reference case.
- Case 1: baffles positioned in the second half of the air channel “50% Up”.
- Case 2: baffles positioned in the first half of the air channel “50% Down”.
- Case 3: baffles positioned in the middle of the air channel “50% Middle”.
- Case 4: baffles positioned in all the air channel “100%”.

## III.2.2. Mesh generation

### III.2.2.1. Mesh with Gambit

One of the most important aspects when using CFD tools is creating the computational grid for the domain.

To obtain accurate meaningful numerical solutions, the first crucial step is the meshing of the computational domain, the importance of which is discerned in fast and high moving flows due to steep gradients arising within the boundary viscous sublayer. For this reason, it is necessary to check that there are enough elements of the mesh within the boundary layer. The parameter that controls whether the number of nodes is sufficient is y +, which must be close to one.

The commercial mesh generator GAMBIT (version 2.4.6) was used to create the geometry of the solar air heater (SAH) and to generate the computational domain mesh. We chose a three-dimensional unstructured (Tri / tetra) tetrahedral mesh because of the complicated baffle shape studied. Figure III-2 shows the grid (mesh) of the bafled cases.

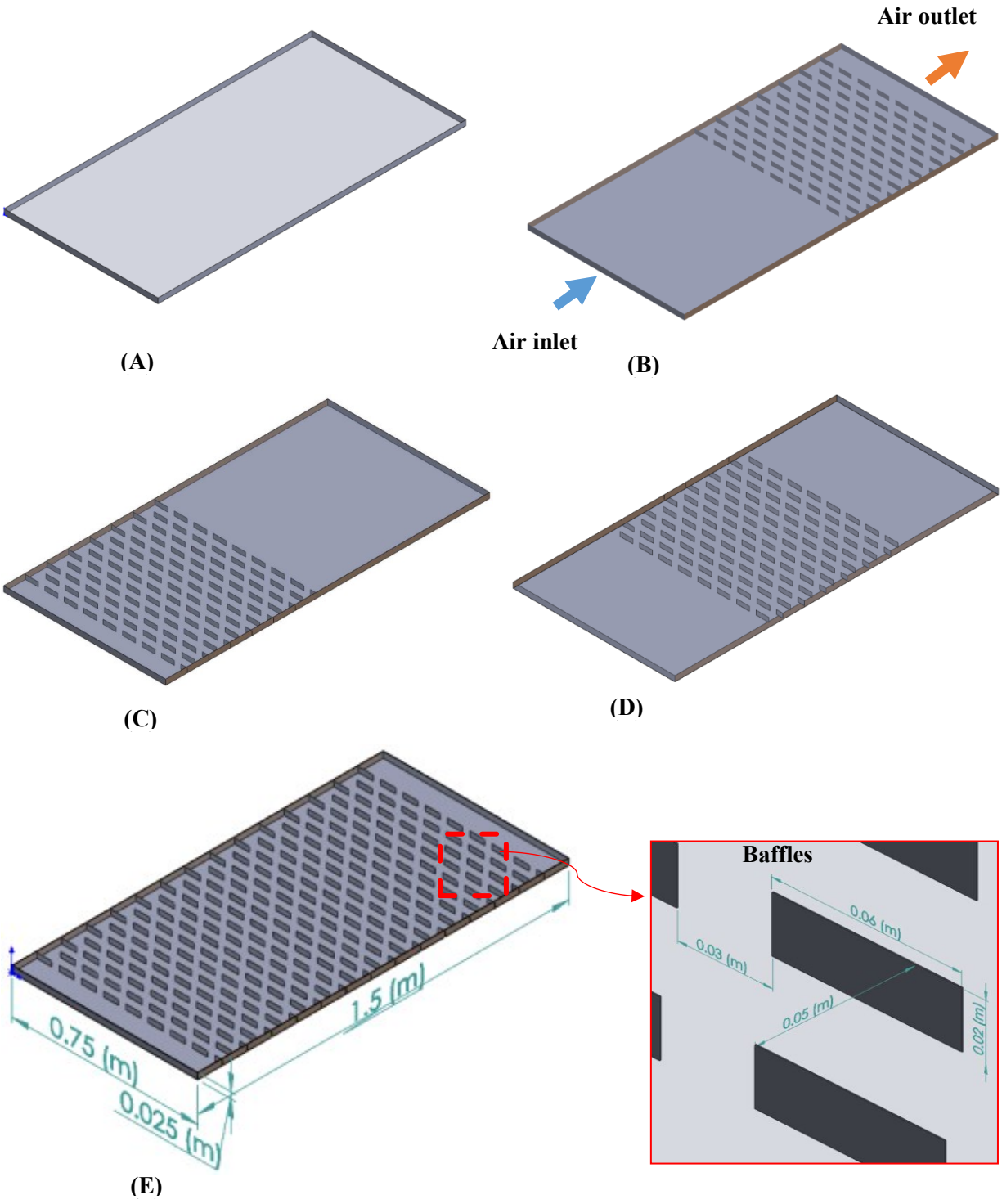


**Figure III-1:** Studied cases of solar air heater and dimensions: (A) Smooth plate (without Baffles); (B) Case 1(50% Up); (C) Case 2(50% Down); (D) Case 3(50% Middle); (E) Case 4(100%).

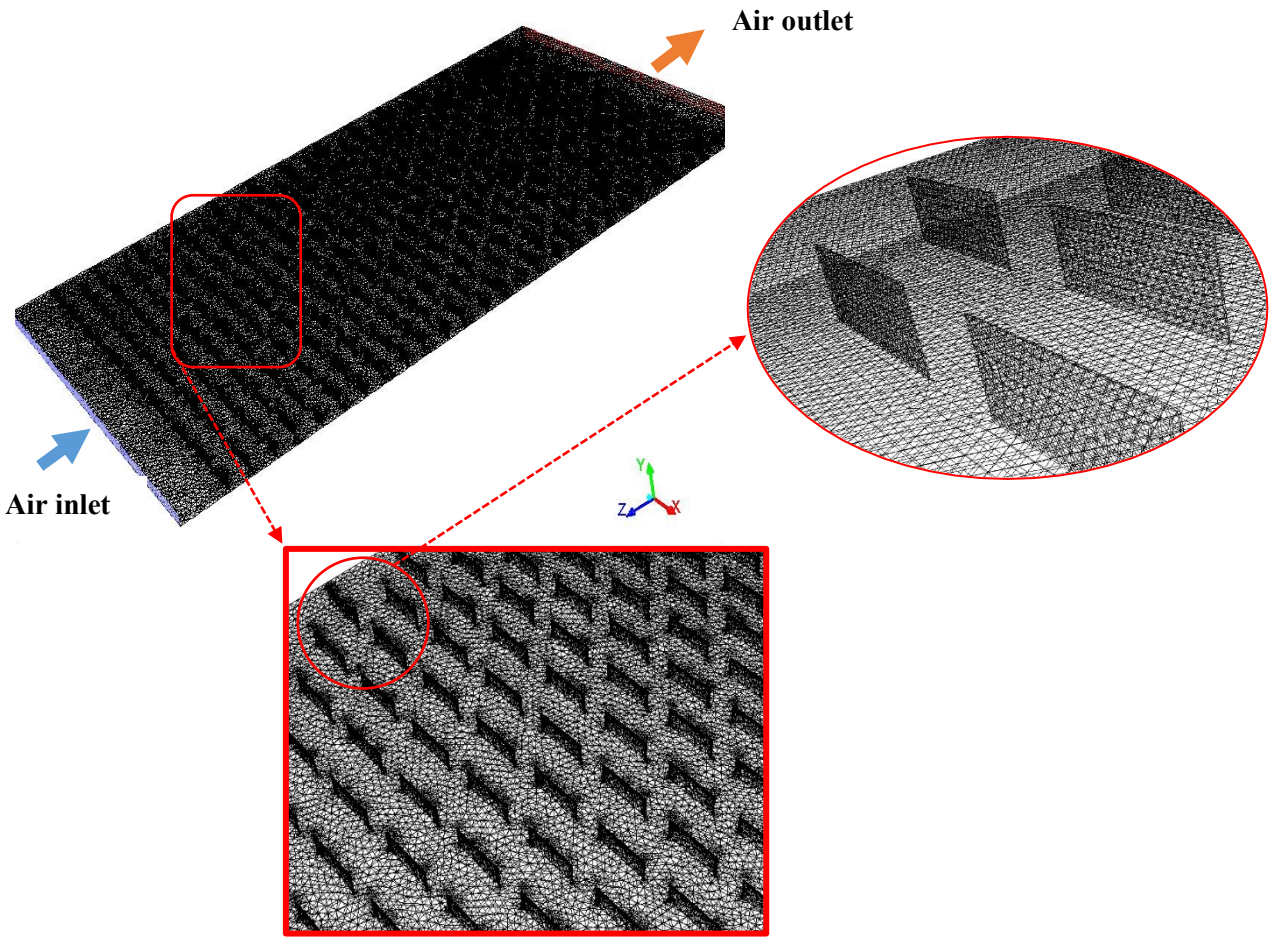


**Figure III-2:** Grid (mesh) of the bafled cases

### III.2.2.2.Boundary conditions in Gambit

Once the geometry and the mesh of the studied physical domain are defined, we will specify the geometrical zones on which we will apply the boundary conditions. Under Gambit, there are two characteristics of zone types (boundary conditions) (Figure III-3) :

• Boundary types (Wall or Wind) to define the external or internal boundaries.

• Continuum types (Fluid or Solid) to define the regions of the domain.

The flow in the channel is bounded by two horizontal walls, one upper "Absorber" and the other lower "bottom". The first is considered as static wall imposed on it a heat flux "Heat flux", while the second is adiabatic "Adiabatic wall", as well as the two other side walls are adiabatic "Adiabatic wall". The condition imposed on the inlet is a mass flow "Mass flow inlet" and at the outlet is a pressure "Pressure outlet". The interior domain is considered to be “fluid”.


**Figure III-3:** Boundary conditions in Gambit: (a) Boundary types ,(b) Continuum types

### III.2.3. Solver

In the computational model studied, steady state, 3D geometry, and Newtonian fluid are considered. All of the fluid's properties remain constant and it behaves as an ideal gas. All of the properties are evaluated at the fluid's average temperature within the enclosure. The phenomenon under study is forced convection; therefore, the velocities are large enough for all buoyancy effects to be negligible and for gravity to be ignored.

The CFD results are obtained by solving the Navier-Stokes equations and the energy equation through the finite volume method using the commercial software package (ANSYS FLUENT 15.0) under the following assumptions:

- The fluid maintains single-phase, incompressible turbulent flow across the duct.
- 3D fluid flow and heat transfer.

- Negligible radiative and natural convective heat transfer between components of computational domain.
- Steady-state conditions.
- The thermo-physical properties of both the fluid (air) and the solid absorber plate (aluminum) are constant.

Based on the above assumptions, the channel flow is governed by the continuity, the Navier–Stokes equations and the energy equation. In the Cartesian tensor system these equations can be written as follows:

**III.2.3.1.Continuity equation:**

This equation is deduced from the principle of mass conservation. It is expressed according to Versteeg et Malalasekera [82], in tensorial form as following:

$$\frac{\partial}{\partial x_i}(\rho u_i) = 0 \qquad \text{(III.1)}$$

Where *i= 1, 2, 3:* summation index

The air is considered an incompressible fluid ($\rho$ = constant), so, equation (III.1) reduces to:

$$\frac{\partial u_i}{\partial x_i} = 0 \qquad \text{(III.2)}$$

Where $u_i$ is the velocity components in the Cartesian coordinate system with its coordinates $x_i$

**III.2.3.2.Momentum equation:**

This equation is deduced from the Second Law of Dynamics, which states that the change in the momentum of a fluid particle is equal to the sum of the external forces on that particle. It is written according to Versteeg and Malalasekera [82], in tensorial form as follows:

$$\frac{\partial(\rho u_i u_j)}{\partial x_j} = -\frac{\partial P}{\partial x_i} + \frac{\partial}{\partial x_j}\left[\mu\left(\frac{\partial u_j}{\partial u_i} + \frac{\partial u_i}{\partial u_j}\right)\right] \qquad \text{(III.3)}$$

Where

$\frac{\partial(\rho u_i u_j)}{\partial x_j}$ : Represents the transport rate of momentum in direction (i), by movement of the fluid.

$\frac{\partial P}{\partial x_i}$ : Represents the forces due to pressure.

$\frac{\partial}{\partial x_j}\left[\mu\left(\frac{\partial u_j}{\partial u_i} + \frac{\partial u_i}{\partial u_j}\right)\right]$ : Represents viscosity forces.

**III.2.3.3.Energy equation:**

The energy equation is obtained by applying the first principle of thermodynamics for an incompressible and Newtonian fluid, according to Versteeg and Malalasekera [82] it is written as follows:

$$\frac{\partial(\rho u_i T)}{\partial x_i} = \frac{\partial}{\partial x_j}\left[(\Gamma + \Gamma_t)\frac{\partial T}{\partial x_j}\right] \quad \text{(III.4)}$$

Where

$\Gamma = \frac{\mu}{P_r}$ : Represent the molecular thermal diffusivity.

$\Gamma_t = \frac{\mu_t}{P_{r_t}}$ : Represent the turbulent thermal diffusivity.

$\mu_t$: The eddy viscosity

$u_i$ is correspond to the average velocity of x, y and z direction, respectively. $\rho$ and T are represents average density and average temperature respectively.

ANSYS Fluent allows you to choose from several upwind schemes: first-order upwind, second-order upwind, power law, and QUICk. The governing equations were discretized by the QUICK differencing scheme, decoupling with the SIMPLE algorithm and solved using a finite volume approach which devloped by patankar [83].

The SIMPLE algorithm uses a relationship between velocity and pressure corrections to enforce mass conservation and to obtain the pressure field, the segregated SIMPLE algorithm steps has been presented in Figure III-4. The momentum, mass and energy equations were solved iteratively for the corresponding boundary conditions using numerical methods until convergence was reached for the variables of interest (velocities, temperature, pressure and the walls heat flow).

A double precision pressure-based solver and second order discretization method was considered to calculate the solution. Default under-relaxation factors of the solver are employed to control the update of computed variables for each iteration, These factors for pressure, density, momentum and energy are presented in Table III-1.

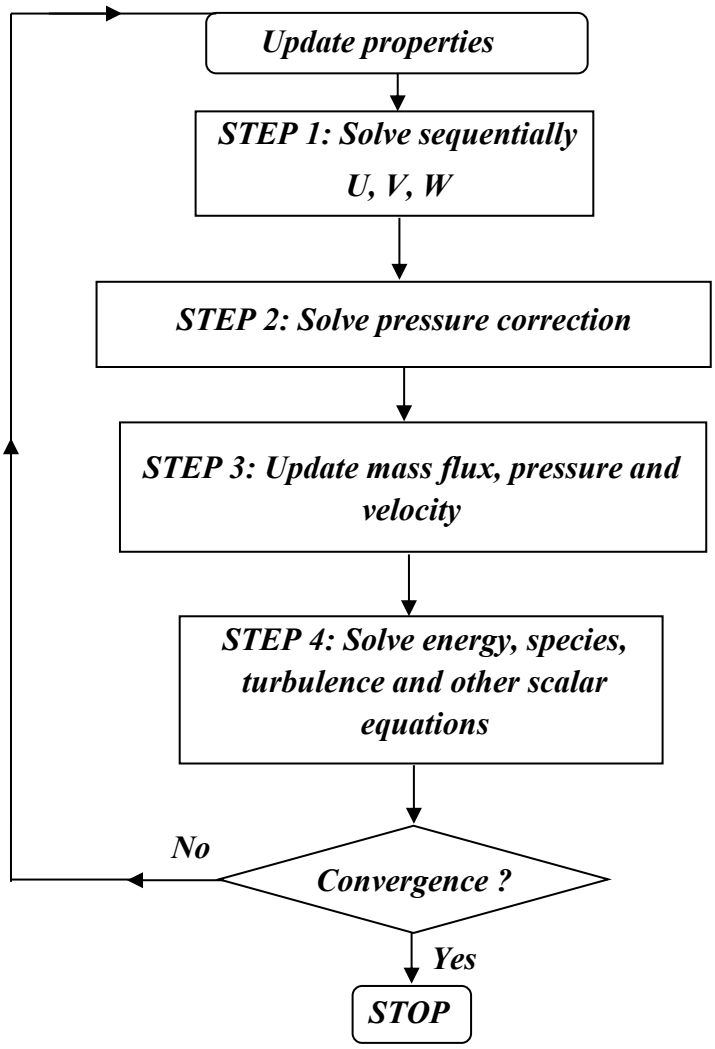


**Figure III-4:** Steps of the segregated SIMPLE algorithm (Pressure-Based Solution Methods)

**Table III-1:** Solution control parameters (under-relaxation factors)

| Variables | Under-relaxation factors |
|---|---|
| Pressure | 0.3 |
| Density | 1 |
| Body forces | 1 |
| Momentum | 0.7 |
| Turbulant kinitic energy | 0.8 |
| Turbulant dispation rate | 0.8 |
| Turbulant viscosity | 1 |
| Energy | 1 |

The residuals for the convergence of the solution are selected as $10^{-6}$ for the energy equation and $10^{-5}$ each for the equations of continuity, velocity, turbulence dissipation and turbulence kinetic energy as presented in Figures III-5 and III-6. The calculations involved in our simulations were performed on an HP Z420 Workstation machine with an Intel (R) Xeon (R) Silver 4114 CPU @ 2.20 GHz and 24.0 GB of RAM.

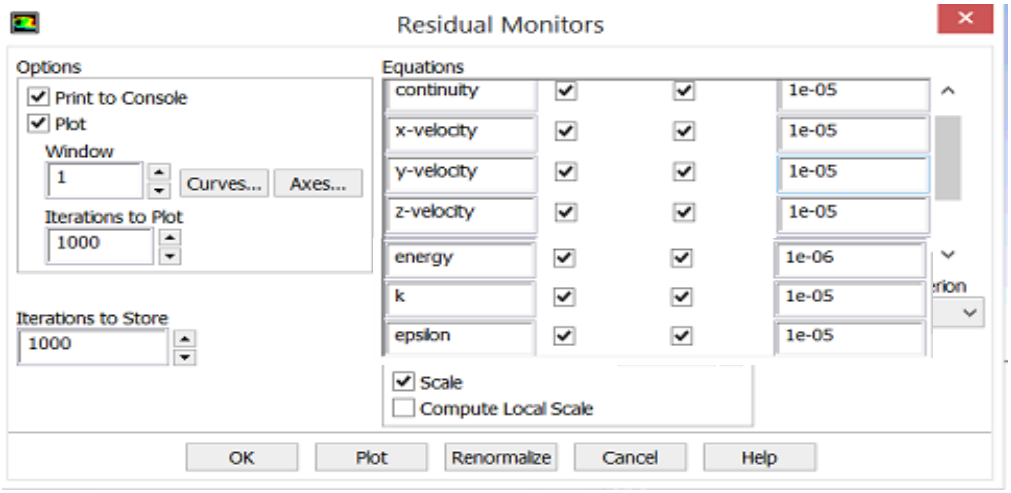


**Figure III-5:** Convergence criteria

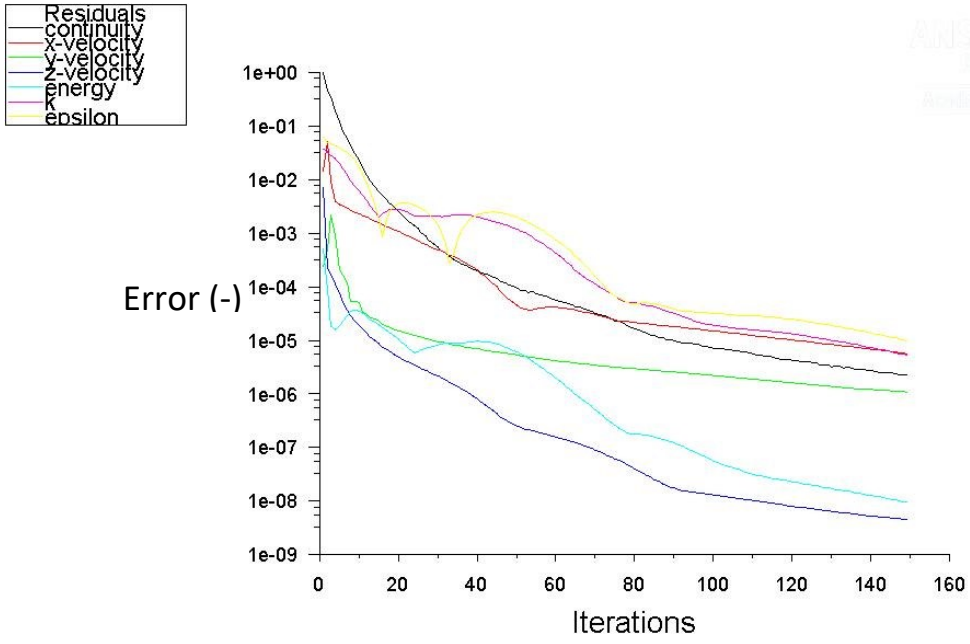


**Figure III-6:** Curves of the convergence solution

### III.2.4. Turbulence models

The literature survey reveals that the solar air heaters are thermo-hydraulically more efficient if system operates at Reynolds numbers ranges from 3000 to 19,000. Reynolds number inside the rectangular duct of solar air heater shows that the flow is turbulent.

One of the great challenges in the design of a solar air heater using CFD approach is the selection of appropriate turbulence model. When CFD simulations of a flow through a solar air heater are concerned, we often wonder, whether the simulation produces a precise image of the real flow. The question is not answered easily, as the quality of the obtained result depends on many parameters of the computer model.

Modern CFD programs offer their users many possible parameters of the mathematical model. However, if various turbulence models are available, the user may wonder which of them is the best suited for a solar air heater system. A turbulence model is a computational procedure to close the system of mean flow equations. Turbulence models allow the calculation of the mean flow without first calculating the full time-dependent flow field. Modern CFD programs offer a large range of methods and models to simulate turbulence. The methods include[84]:

- Reynolds-average simulation (RAS)/Reynolds-averaged Navier–Stokes (RANS): The governing equations are solved in ensemble averaged form, including appropriate models for the effect of turbulence.
- Large eddy simulation (LES): Large turbulent structures in the flow are resolved by the governing equations, while the effect of the sub-grid scales (SGS) are modeled. The scale separation is obtained by applying a filter to the governing equations which also influences the form of the SGS models.
- Detached eddy simulation (DES): Hybrid method that treats near-wall regions with a RAS approach and the bulk flow with an LES approach.
- Direct numerical simulation (DNS): Resolves all scales of turbulence by solving the Navier–Stokes equations numerically without any turbulence modeling.

There are several turbulence model included in the commercial CFD software ANSYS FLUENT 15.0. The following turbulence models, available in ANSYS FLUENT 15.0, are tested: Standard k-ε, Realizable k-ε, Renormalization-group RNG k-ε, Standard k-ω, and Shear Stress Transport (SST) k-ω [84].

#### III.2.4.1. Standard k-ε model

Two-equation turbulence models allow the determination of both, a turbulent length and time scale by solving two separate transport equations. The standard k-ε model in ANSYS Fluent falls within this class of models and has become the workhorse of practical engineering flow calculations in the time since it was

proposed by Launder and Spalding [85]. Robustness, economy, and reasonable accuracy for a wide range of turbulent flows explain its popularity in industrial flow and heat transfer simulations. It is a semi-empirical model, and the derivation of the model equations relies on phenomenological considerations and empiricism.

The standard k-ε model [85] is a model based on model transport equations for the turbulence kinetic energy (k) and its dissipation rate (ε). The model transport equation for k is derived from the exact equation, while the model transport equation for ε was obtained using physical reasoning and bears little resemblance to its mathematically exact counterpart.

In the derivation of the k-ε model, the assumption is that the flow is fully turbulent, and the effects of molecular viscosity are negligible. The standard k-ε model is therefore valid only for fully turbulent flows. As the strengths and weaknesses of the standard k-ε model have become known, modifications have been introduced to improve its performance.

#### III.2.4.2.Realizable k-ε

The realizable k-ε model [86] differs from the standard k-ε model in two important ways:

- The realizable k-ε model contains an alternative formulation for the turbulent viscosity.
- A modified transport equation for the dissipation rate, ε, has been derived from an exact equation for the transport of the mean-square vorticity fluctuation.

The term “realizable” means that the model satisfies certain mathematical constraints on the Reynolds stresses, consistent with the physics of turbulent flows. Neither the standard k-ε model or the RNG k-ε model is realizable. Both the realizable and RNG k-ε models have shown substantial improvements over the standard k-ε model where the flow features include strong streamline curvature, vortices, and rotation. Since the model is still relatively new, it is not clear in exactly which instances the realizable k-ε model consistently outperforms the RNG model. However, initial studies have shown that the realizable model provides the best performance of all the k-ε model versions for several validations of separated flows and flows with complex secondary flow features.

One of the weaknesses of the standard k-ε model or other traditional k-ε models lies with the modeled equation for the dissipation rate (ε). The well-known round-jet anomaly (named based on the finding that the spreading rate in planar jets is predicted reasonably well, but prediction of the spreading rate for axisymmetric jets is unexpectedly poor) is considered to be mainly due to the modeled dissipation equation.

**III.2.4.3.Renormalization-group RNG k-ε**

The RNG k-ε model was derived using a statistical technique called renormalization group theory. It is similar in form to the standard k-ε model, but includes the following refinements:

• The RNG model has an additional term in its -equation that improves the accuracy for rapidly strained flows.

• The effect of swirl on turbulence is included in the RNG model, enhancing accuracy for swirling flows.

• The RNG theory provides an analytical formula for turbulent Prandtl numbers, while the standard k-ε model uses user-specified, constant values.

• While the standard k-ε model is a high-Reynolds number model, the RNG theory provides an analytically derived differential formula for effective viscosity that accounts for low-Reynolds number effects. Effective use of this feature does, however, depend on an appropriate treatment of the near-wall region.

These features make the RNG k-ε model more accurate and reliable for a wider class of flows than the standard k-ε model. The RNG-based k-ε turbulence model is derived from the instantaneous Navier-Stokes equations, using a mathematical technique called “renormalization group” (RNG) methods.

The analytical derivation results in a model with constants different from those in the standard k-ε model, and additional terms and functions in the transport equations for k and ε. A more comprehensive description of RNG theory and its application to turbulence can be found in [87].

When the renormalization-group RNG k-ε model used to perform CFD simulation, the transport equations for turbulent kinetic energy k and its rate of dissipation ε used in the RNG k-ε model are as follows:

$$\frac{\partial(\rho k u_i)}{\partial x_i} = \frac{\partial}{\partial x_j}\left[\alpha_k \mu_{eff} \frac{\partial k}{\partial x_j}\right] + G_k + G_b - \rho\varepsilon \qquad \text{(III.5)}$$

And

$$\frac{\partial(\rho \varepsilon u_i)}{\partial x_i} = \frac{\partial}{\partial x_j}\left[\alpha_\varepsilon \mu_{eff} \frac{\partial \varepsilon}{\partial x_j}\right] + G_{1\varepsilon}\frac{\varepsilon}{k}(G_k + C_{3\varepsilon}G_b) - C_{2\varepsilon}\rho\frac{\varepsilon}{k} - R_\varepsilon \qquad \text{(III.6)}$$

Where

$G_k$: Represents the generation of turbulence kinetic energy due to the mean velocity gradients.

$G_b$: Represents the generation of turbulence kinetic energy due to buoyancy.

The quantities $\alpha_k$ and $\alpha_\varepsilon$ are the inverse effective Prandtl numbers for k and ε, respectively.

$\alpha_k = \alpha_\varepsilon = 1.393.$

The main difference between the RNG and standard k-ε models lies in the additional term in the ε equation given by:

$$R_\varepsilon = \frac{C_\mu \rho \eta^3 (1-\eta/\eta_0)}{1+\beta\eta^3} \frac{\varepsilon^2}{k} \quad \text{(III.7)}$$

Where

$\eta = S\frac{k}{\varepsilon}$, $\eta_0 = 4.38$, $\beta = 0.012.$

The constants of this model are given as follow:

$G_{1\varepsilon} = 1.42$, $C_{2\varepsilon} = 1.68$, $C_{3\varepsilon} = 1.8$, $C_\mu = 0.0845.$

#### III.2.4.4. Standard k-ω

The standard k-ω model in ANSYS Fluent is based on the Wilcox k-ω model [88], which incorporates modifications for low-Reynolds number effects, compressibility, and shear flow spreading. One of the weak points of the Wilcox model is the sensitivity of the solutions to values for k and ω outside the shear layer (freestream sensitivity). While the new formulation implemented in ANSYS Fluent has reduced this dependency, it can still have a significant effect on the solution, especially for free shear flows [89].

The standard k-ω model is an empirical model based on model transport equations for the turbulence kinetic energy (k) and the specific dissipation rate (ω), which can also be thought of as the ratio of ε to k [88]. As the k-ω model has been modified over the years, production terms have been added to both the k and ω equations, which have improved the accuracy of the model for predicting free shear flows [88].

#### III.2.4.5. Shear Stress Transport (SST) k-ω

The shear-stress transport (SST) k-ω model was developed by Menter [88] to effectively blend the robust and accurate formulation of the k-ω model in the near-wall region with the freestream independence of the k- ε model in the far field. To achieve this, the k- ε model is converted into a k-ω formulation. The SST k-ω model is similar to the standard k-ω model, but includes the following refinements:

• The standard k-ω model and the transformed k- ε model are both multiplied by a blending function and both models are added together. The blending function is designed to be one in the near-wall region, which activates the standard k-ω model, and zero away from the surface, which activates the transformed k- ε model.

• The SST model incorporates a damped cross-diffusion derivative term in the ω equation.

• The definition of the turbulent viscosity is modified to account for the transport of the turbulent shear stress.

• The modeling constants are different.

These features make the SST k-ω model more accurate and reliable for a wider class of flows than the standard k-ω model [84].

### III.2.5. Boundary conditions

The boundary conditions applied to carry out the simulation were:

- At the inlet section (in X-direction), a mass flow rate condition ranging from 0.017 to 0.06 kg/s corresponding to the range of Reynolds numbers from 2370 to 8340 and $T_{inlet}$ = 300.15 K (see Table III-2).

Table III-2 shows the average surface temperatures taken from the experiments and used for validation purposes. In addition, the boundary conditions for turbulence parameters need to be specified as derived quantities at inlet locations such as turbulence intensity and hydraulic diameter. The turbulent intensity values ranged from 5.175 to 6.057, estimated according to the Reynolds number as [90,91]:

$$I=0.16\ (Re)^{-1/8} \qquad \text{(III.8)}$$

- The absorber plate, bottom plate and side walls conditions are shown in Table III-3.

The thermo-physical properties of the air and absorber plate, which have been assumed to remain constant at mean bulk temperature, are presented in Table III-4.

**Table III-2:** Boundary Conditions (BCs) for the validation process

| | $BC_1$ | $BC_2$ |
|---|---|---|
| Mass flow rate | 0.017 kg/s | 0.025 kg/s |
| Absorber Temperature | 351.4 K | 362.4 K |
| Bottom Temperature | 332.28 K | 339.61 K |
| Sides heat flux | Adiabatic Q= 0 W | Adiabatic Q= 0 W |

**Table III-3:** Boundary Conditions (BCs) for use of the model

| | $BC_3$ | $BC_4$ | $BC_5$ | $BC_6$ | $BC_7$ | $BC_8$ |
|---|---|---|---|---|---|---|
| Mass flow rate | 0.017 kg/s | 0.025 kg/s | 0.035 kg/s | 0.04 kg/s | 0.05 kg/s | 0.06 kg/s |
| Absorber heat flux | 1000 W/m$^2$ | 1000 W/m$^2$ | 1000 W/m$^2$ | 1000 W/m$^2$ | 1000 W/m$^2$ | 1000 W/m$^2$ |
| Bottom and Sides heat flux | Adiabatic Q= 0 W | Adiabatic Q= 0 W | Adiabatic Q= 0 W | Adiabatic Q= 0 W | Adiabatic Q= 0 W | Adiabatic Q= 0 W |

**Table III-4:** Thermo-physical properties of air and absorber plate for CFD analysis

| Proprieties | Fluid (air) | Absorber plate (aluminum) |
|---|---|---|
| Density, 'ρ' [kg/m$^3$] | 1.167 | 2719 |
| Viscosity, 'μ' [kg/ms] | 1.85 e-05 | - |
| Thermal conductivity, 'λ'[W/mK] | 0.0262 | 202.4 |
| Specific heat, '$C_p$' [J/kgK] | 1006 | 871 |

## III.2.6. Validation of the numerical model

### III.2.6.1. Grid sensitive analysis

The commercial mesh generator GAMBIT (version 2.4.6) was used to create the geometry of the solar air heater (SAH) and to generate the computational domain mesh. The mesh independency test was carried out for the case Re = 2354 by comparing seven different numbers of cells in order to eliminate the effect on the numerical computation results in terms of outlet air temperature and the average heat transfer coefficient.

The results of the mesh independency test are shown in Table III-5. To carry out the solutions, the number of cells was increased from 45,904 to 483,042. The additional cells changed the performance factor by more than 2% at the outlet temperature and more than 3% at the convective heat transfer coefficient. The number of cells selected was 432,432, based on the minimum percentage deviation of the $T_{out}$ and $h$.

**Table III-5:** Grid independence test

| Cells Number | $T_{out}$ $(K)$ | $h$ $(W/m^2K)$ | Percentage deviation of $T_{out}$ $(\%)$ | Percentage deviation of $h$ $(\%)$ |
|---|---|---|---|---|
| 45904 | 341.07 | 6.37 | - | - |
| 81204 | 341.49 | 6.38 | 0.61 | 0.06 |
| 158130 | 342.27 | 6.26 | 1.11 | 1.90 |
| 272706 | 344.24 | 6.45 | 2.77 | 3.02 |
| 384622 | 345.37 | 6.55 | 1.56 | 1.51 |
| **432432** | 345.39 | 6.55 | 0.03 | 0.01 |
| 483042 | 345.42 | 6.55 | 0.04 | 0.007 |

### III.2.6.2.Turbulence models validation

Roughened channels were used for heat transfer enhancement by increasing the turbulence level in the fluid flow. Furthermore, to ensure the accuracy of the numerical results, the suitability of different turbulence models for the present numerical problem was evaluated. The five known classical turbulence k-ε models including standard k-ε, RNG k-ε, realizable k-ε and k-ω models were used in this evaluation. The accuracy of the selected model was tested by comparing its results with those in the literature.

The Nusselt number (*Nu*) and friction factor (*f*) values are obtained from a numerical model with different turbulence models and compared with the standard correlations of Dittus-Boelter [92](Eqt. (III.9)) and Modified Blasius [93](Eqt. (III.10)).

$$Nu = 0.023Re^{0.8}Pr^{0.4} \quad \text{(III.9)}$$

$$f = 0.791Re^{-0.25} \quad \text{(III.10)}$$

The results of the numerical simulations of *Nu* and f were validated with Eqs. (III.9) and (III.10) for Reynolds numbers ranging from 2370 to 8340. The comparison of predicted and calculated (from correlation) *Nu* and *f* values is shown in Figures III-7 and III-8, respectively.

The comparison shows the best approximation for the RNG k-ε model. The average percentage deviation of the Nusselt number and the friction factor predicted by the RNG k-ε model are ±4.35% and ±3.08% from the values calculated from the above correlations for the same Reynolds number range.

In addition, Tables III-6 and III-7 are show the deviations of all the models for each point. It can be noted that the RNG k-ε turbulence model has also been used in earlier numerical studies into roughened SAHs, reported by [94–102]. The RNG k-ε model was selected for this CFD analysis.

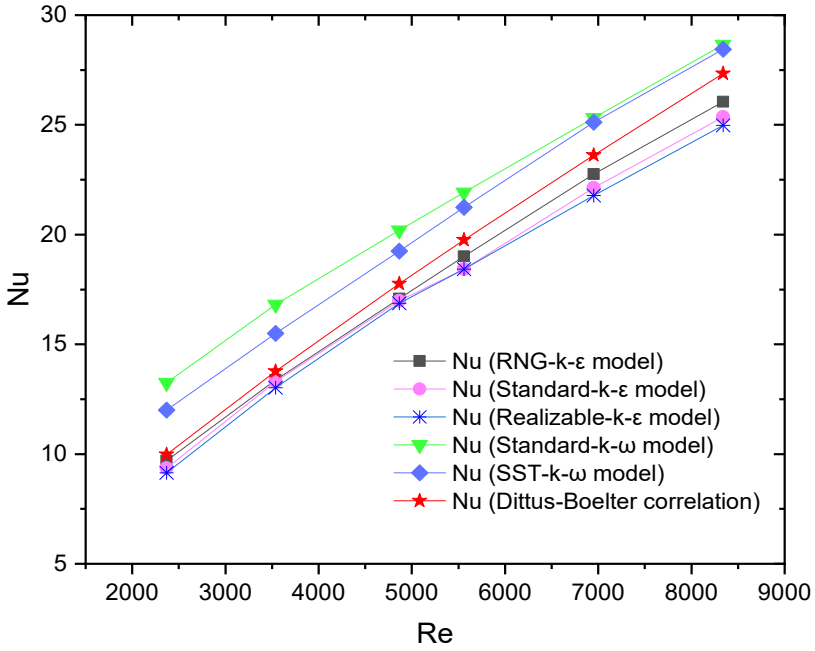


**Figure III-7:** Comparison of predicted Nusselt Number values for different turbulence models with Dittus-Boelter correlations [92]

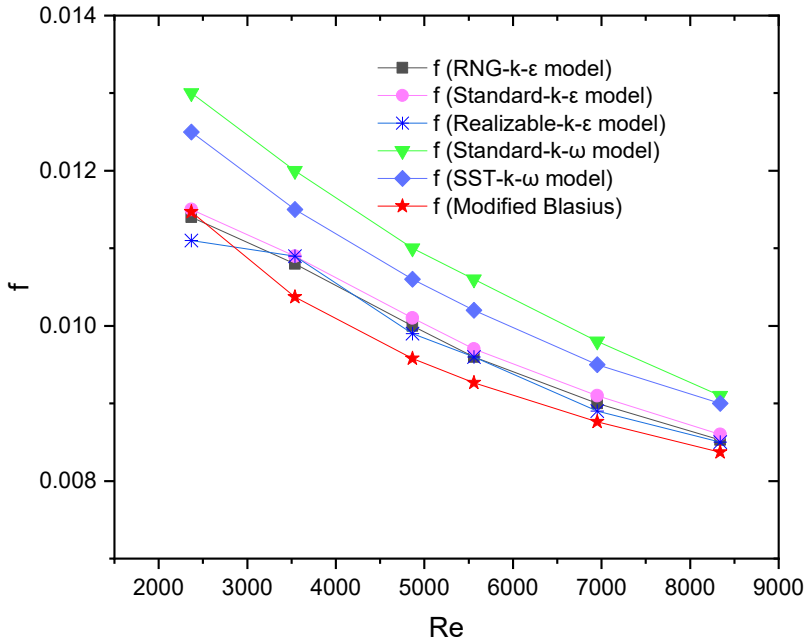


**Figure III-8:** Comparison of predicted friction factor values for different turbulence models with Modified Blasius correlation [93]

**Table III-6:** Nusselt number deviation

| RNG-k-ε model | Stand-k-ε model | Realizable-k-ε model | Stand-k-ω model | SST-k-ω model |
|---|---|---|---|---|
| 2.87% | 6.27% | 8.38% | 32.67% | 20.15% |
| 2.87% | 3.31% | 5.41% | 22.11% | 12.59% |
| 3.82% | 4.38% | 5.00% | 13.74% | 8.39% |
| 3.85% | 6.73% | 6.78% | 10.92% | 7.48% |
| 3.69% | 6.32% | 7.80% | 7.17% | 6.33% |
| 4.69% | 7.22% | 8.61% | 4.81% | 4.04% |

**Table III-7:** Friction factor deviation

| RNG-k-ε model | Stand-k-ε model | Realizable-k-ε model | Stand-k-ω model | SST-k-ω model |
|---|---|---|---|---|
| 0.58% | 0.28% | 3.19% | 13.37% | 9.00% |
| 4.11% | 5.08% | 5.08% | 15.68% | 10.86% |
| 4.39% | 5.43% | 3.35% | 14.83% | 10.65% |
| 3.62% | 4.70% | 3.62% | 14.41% | 10.09% |
| 2.71% | 3.85% | 1.57% | 11.84% | 8.42% |
| 1.89% | 2.73% | 1.53% | 8.70% | 7.50% |

## III.3. CONCLUSION

In this chapter, we have described clearly the numerical methodology step by step. The CFD simulations have been performed by ANSYS FLUENT 15.0 based on the geometry of the experimental test model, the studied geometry has been created and meshed by GAMBIT 4.2.6. The solving steps have been described under defined assumptions and boundary conditions known. The mesh independency test was carried out. The validation of five known classical turbulence models including standard k-ε, RNG k-ε, realizable k-ε and k-ω has been done.

# *CHAPTER IV*

# *RESULTS AND DISCUSSION*

## IV.1. INTRODUCTION

In this chapter, after the proposed CFD methodology validation and the selection of RNG k-ε as the best turbulence model for this CFD analysis. The comparison of the numerical results with the current experimental results has been done. The CFD investigation was carried out for the same parameters used in the experimental study. The study based on CFD the analysis of systems involving fluid flow is performed to predict and present the heat transfer and hydraulic characteristics of five different cases of solar air heaters.

The effects of the placement of baffles and the Reynolds number on heat transfer and hydraulics are obtained in terms of the Nusselt number, local heat transfer coefficient and friction factor for the flow duct. The reference parameter on the effectiveness of each case with baffles in different positions has been defined by Webb and Eckert [80]. This is the parameter to evaluate heat transfer and hydraulic performance and is defined as the thermo-hydraulic performance factor (THPF). The THPF shows the ratio of heat transfer and fluid dynamic performance (Eq. I-6). Based on the CFD results, the thermal efficiency is estimated.

## IV.2. COMPARISON OF NUMERICAL RESULTS AND EXPERIMENTAL DATA

For the validation of the proposed CFD methodology, the results for case 1 (Figure II-4(B)) were determined using the proposed CFD methodology and compared with the current experimental results. The CFD investigation was carried out for the same parameters used in the experimental study at mass flow rates of 0.017 kg/s and 0.025 kg/s, and a solar radiation of 670 W/m$^2$ and 982 W/m$^2$, respectively.

Figure IV-1 presents the comparison of the air temperature along the x-direction in the air channel of the solar air heater obtained by the proposed CFD method with the results determined experimentally. The trends of the CFD results are seen to be in line with the outcomes of the experimental tests. The maximum and minimum absolute deviations of the CFD results from the experimental ones are 4.4% and 0.61%, respectively.

Thus, a good agreement has been achieved between the CFD simulation and the experimental data and the proposed CFD methodology can be used to predict the experimental results with reasonable accuracy and can therefore be used to analyze the other cases.

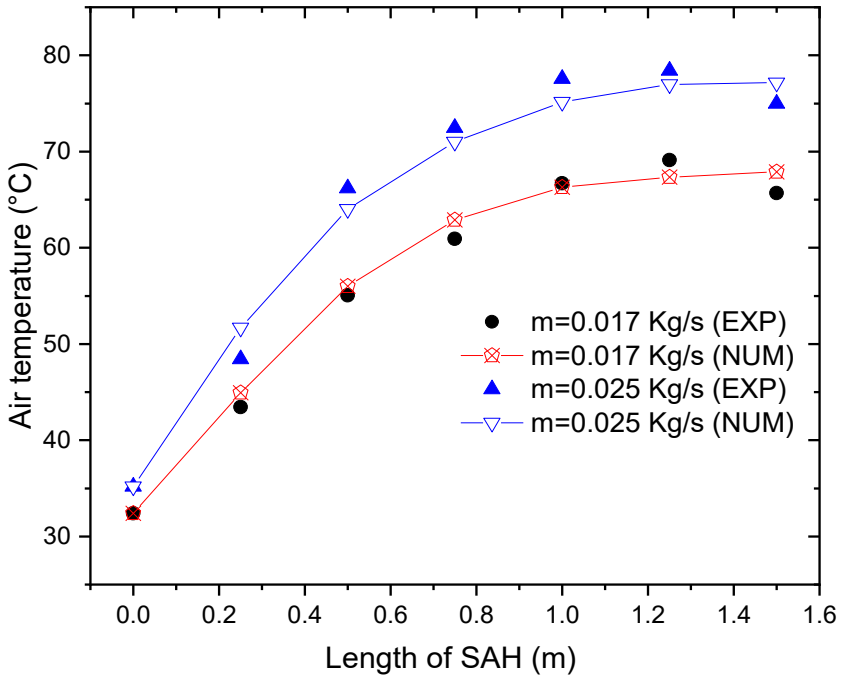


**Figure IV-1:** Comparison of the CFD results and the experimental data

## IV.3. ASSESSMENT OF HEAT TRANSFER COEFFICIENTS

The average Nusselt number versus Reynolds number for a conventional case (smooth) and different positions of baffles corresponding to the five studied cases are shown in Figure IV-2. An increase in the Nusselt number with rises in the Reynolds number was evident in all the investigated cases. The increase in the Reynolds number values leads to a reduction in the thickness of the laminar sub-layers with regard to the conventional duct (smooth).

The Nusselt number values for roughened cases are significantly higher than those for a smooth duct for a given Reynolds number due to the flow mixing induced by the vorticity from the main flow, which can also break the thermal boundary layer. The highest values of the average Nusselt number among the roughened cases is case 4, corresponding to the baffles positioned throughout the air channel (“100%”).

In this case there are fewer dead zones than in the others and high mixing, which contributes to removing the heat from the heated absorber plate and transferring it to the fluid (air). Meanwhile, the lowest Nusselt number values correspond to case 1, in which the baffles were positioned in the second half of the air channel (“50% Up”), where there are more dead zones compared with other cases.

The highest Nusselt number value was Nu= 70.8 at Re= 8340 in case 4, then Nu= 56.72 at Re= 8340 and Nu= 49.76 and Nu= 45.51 for case 3 and case 1, respectively, at the same Reynolds number.

The lowest Nusselt number corresponds to the conventional channel (smooth) (Nu= 25.48; Re= 8340). The predicted results of Nusselt number are compared with the experimental data of Lanjewar et al [28] for a smooth case.

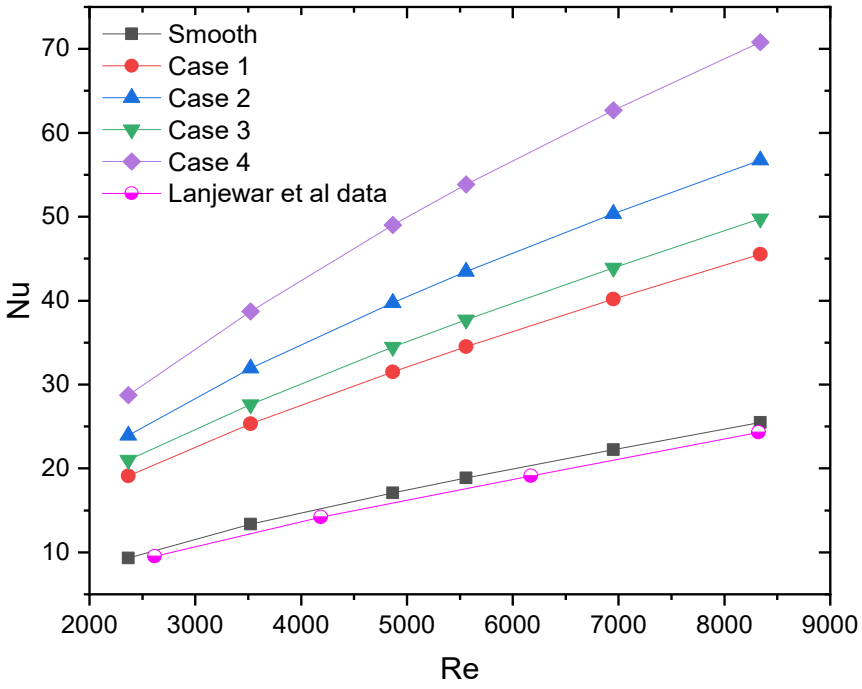


**Figure IV-2:** Variation in Nusselt number with Reynolds number for all cases

The longitudinal local distribution of the convective heat transfer coefficient ($h_x$) of roughened (cases 1-4) and smooth ducts at the absorber plate have been represented in Figures IV-3 to IV-9, shown as a function of the channel length (X(m)) at different Reynolds number ranges from 2370 to 8340 for 4 values. As observed, the local convective heat transfer coefficient curves monotonically increase with the increases in the Reynolds number in all the cases studied.

Figure IV-3 clearly shows that the local convective heat transfer coefficient for the smooth duct at each Reynolds number increases at the beginning of the air channel (0 - 0.15 m). Consequently, the initial vortex brings the colder fluid within the air duct, decreasing the local wall temperature and thus increasing the heat transfer coefficient in that place.

In addition, the length of the transition region is seen to decrease with the increase in Re due to the transition from a laminar to turbulent regime. The local convective heat transfer coefficient then decreases slowly until the outlet section. This behavior is well known and has been reported in the heat transfer literature [103].

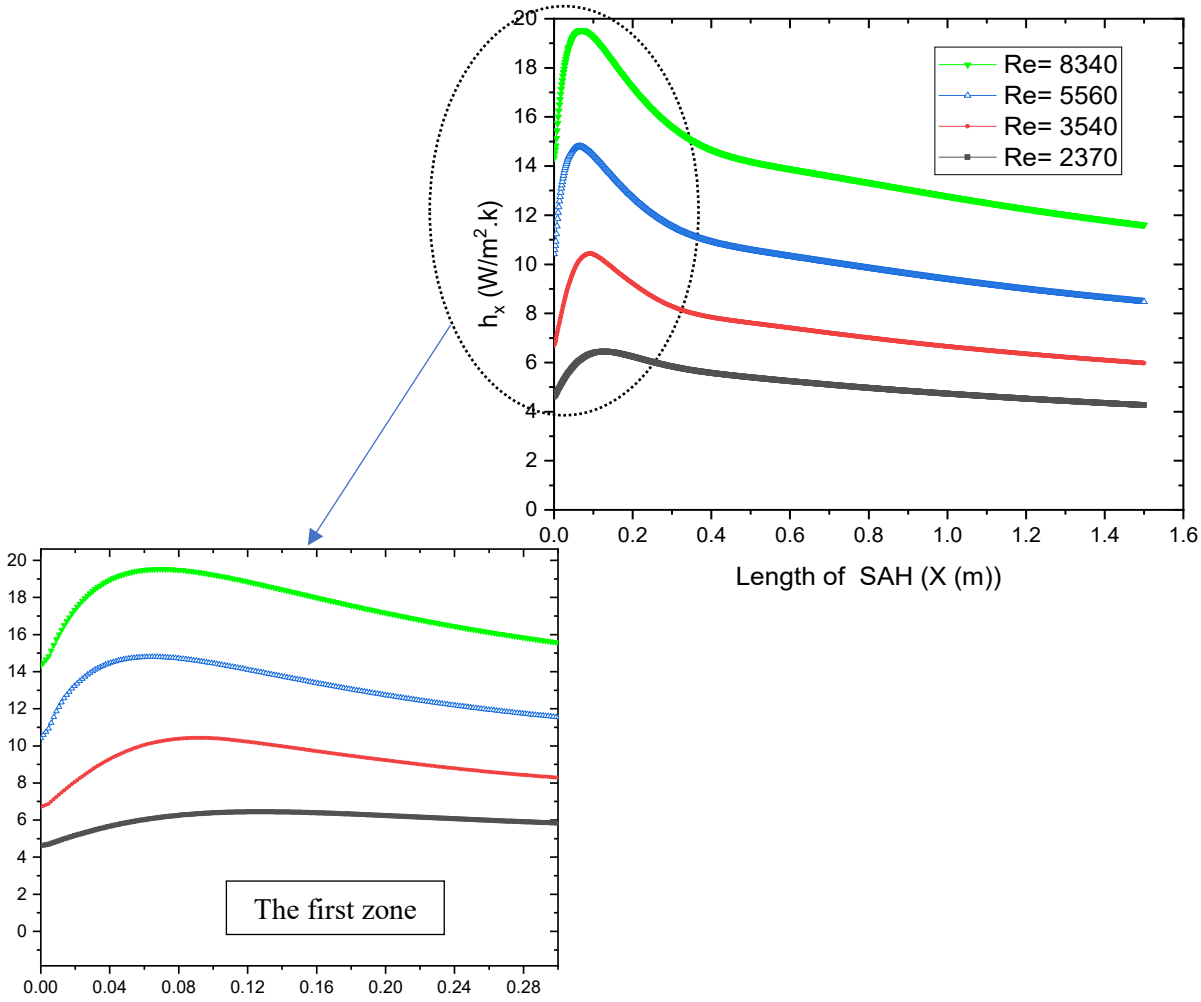


**Figure IV-3:** The local convective heat transfer coefficient versus the length of SAH for the smooth duct at different Reynolds numbers

The effect of the Reynolds number on the local convective heat transfer coefficient is shown in Figures IV-4 to IV-7 for all the baffled cases. The curve of local convective heat transfer coefficient vs SAH length of case 1, the baffles positioned at the second half of the air channel "50% Up" has been presented in Figure IV-4.

The $h_x$ is low in the first smooth part and increases rapidly at the start of the roughened region exactly where the baffles are located, and then decreases rapidly until the edge of this region. Figure IV-4 shows that the highest $h_x$ is in the second half of the air channel. The same behavior is observed in case 2 but the location of the highest $h_x$ changes to the first half of the air channel (50% Down) because of the position of the baffles (Figure IV-5).

Figure IV-6 displays the $h_x$ of case 3 corresponding to the baffles positioned in the middle of the air channel (50% Middle). The curve reaches a minimum in the region after the first baffle and a maximum in the baffled region, then suddenly decreases at the end of this region.

Figure IV-7 represents the local convective heat transfer coefficient ($h_x$) for case 4 (100%). As expected, this case has a higher $h_x$ than the other cases because of the position of the baffles; the $h_x$ increases at the first baffle and decreases slowly to the end of the duct in regular peaks.

All the curves from Figures IV-4 to IV-6 have a part (A) and part (B) corresponding to the smooth and baffled regions, respectively. Part (A) presents peaks with a small amplitude due to two reasons. The first reason is a small perturbation due to the flow regime which corresponds to the turbulence regime as shown at the end of the air duct in part (A) in Figures IV-5 and IV-6, the second is the blockage of the first baffle as shown at part (A) in Figures IV-4 and IV-6, while these perturbations increase a little with the increase in the Reynolds number. The first and second reasons are both evident in Figure IV-6.

The small peaks in the first smooth part depend on the two reasons mentioned above and the small peaks in the second smooth part are a consequence of the first reason only. Furthermore, these peaks increase a little with the increase in the Reynolds number.

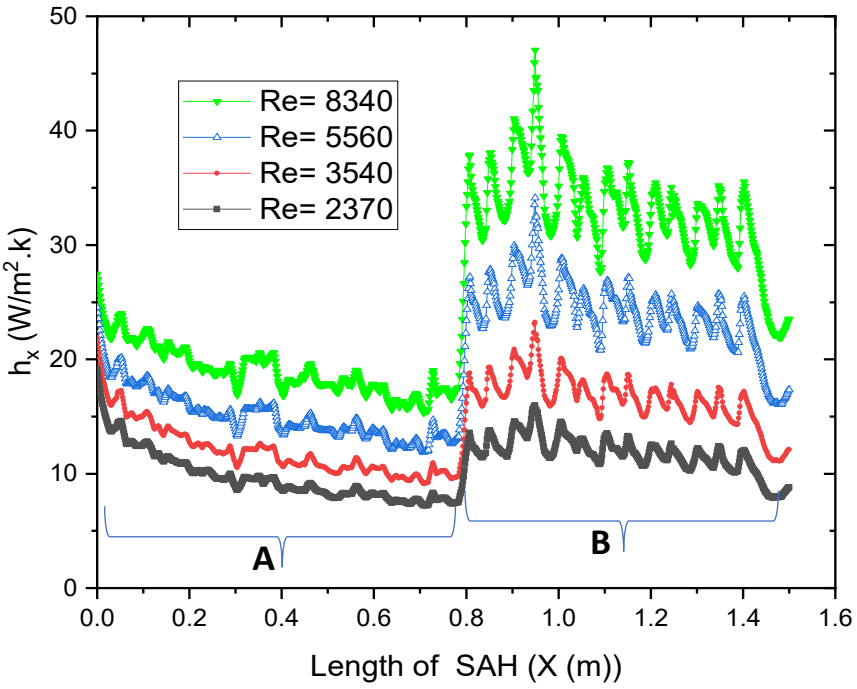


**Figure IV-4:** The local convective heat transfer coefficient versus the length of SAH for Case 1 at different Reynolds numbers

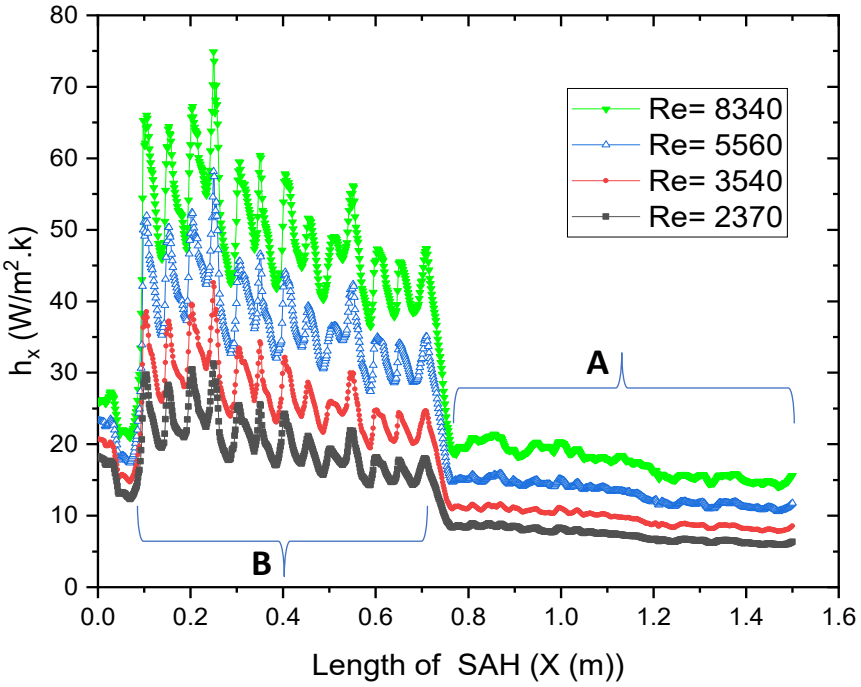


**Figure IV-5:** The local convective heat transfer coefficient versus the length of SAH for Case 2 at different Reynolds numbers

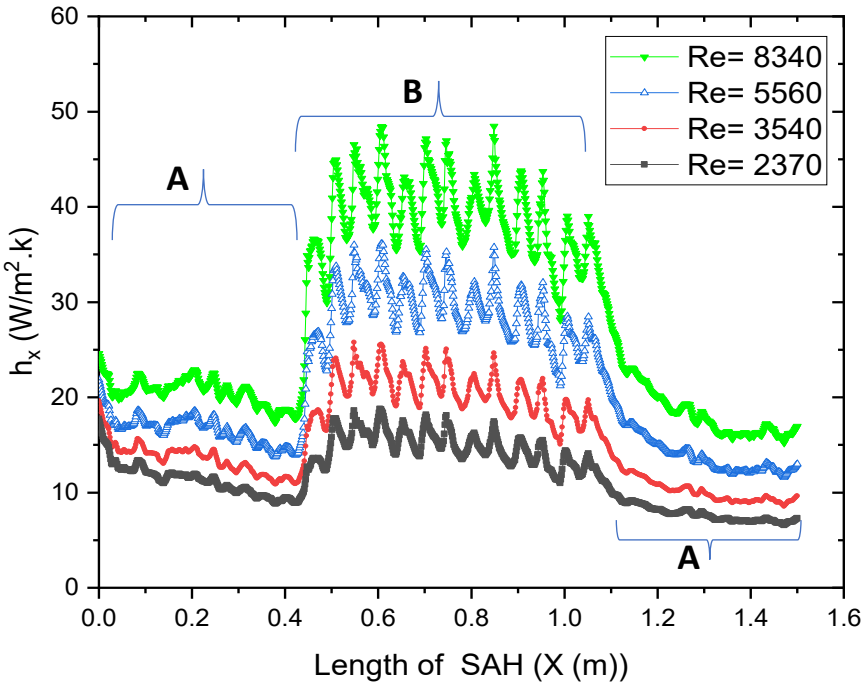


**Figure IV-6:** The local convective heat transfer coefficient versus the length of SAH for Case 3 at different Reynolds numbers

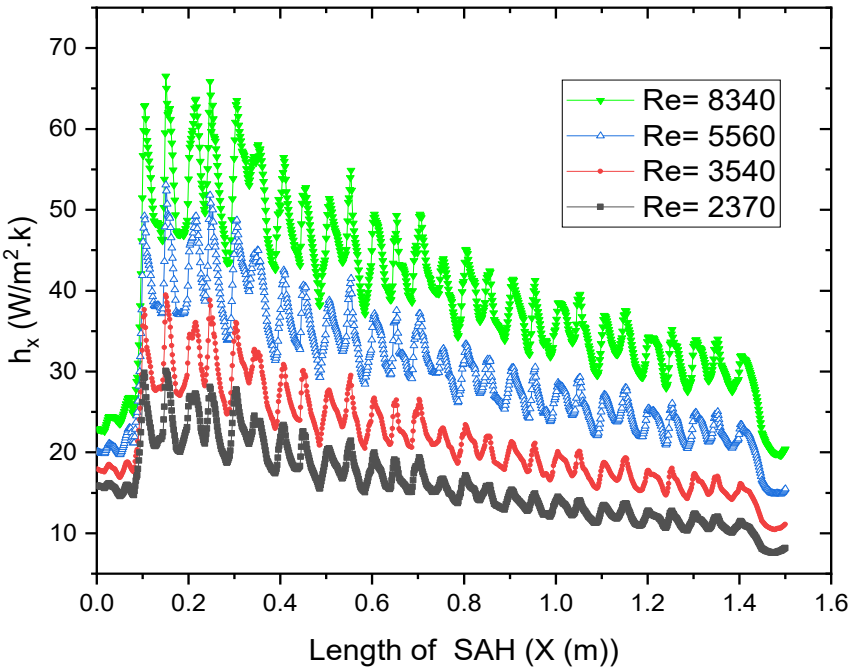


**Figure IV-7:** The local convective heat transfer coefficient versus the length of SAH for Case 4 at different Reynolds numbers

The part (B) in Figures IV-4, IV-5 and IV-6 displays the peaks of the local convective heat transfer coefficient in the baffled region, the peaks presenting a large amplitude due to inter-baffle fluid recirculation. Significantly, the heat transfer enhancement is a result of the reattachment and separation of the flow between consecutive baffles.

Menasria et al. [57] and Sparrow et al. [104] confirmed that the local convective heat transfer coefficient peaks are located downstream of each baffle. The comparison of the local convective heat transfer coefficient of the different investigated cases for Re= 2370 and 8340 are shown in Figures IV-8 and IV-9. The maximal value for the local convective heat transfer coefficient $h_x$= 32 W/m$^2$K was obtained from case 2 (50%Down) for Re =2370, as shown in Figure IV-8.

Figures IV-9 shows that case 2 also has the maximal local heat transfer coefficient value ($h_x$= 75 W/m$^2$K for Re = 8340). In each case, the highest local convection heat transfer coefficients correspond to the location of baffles.

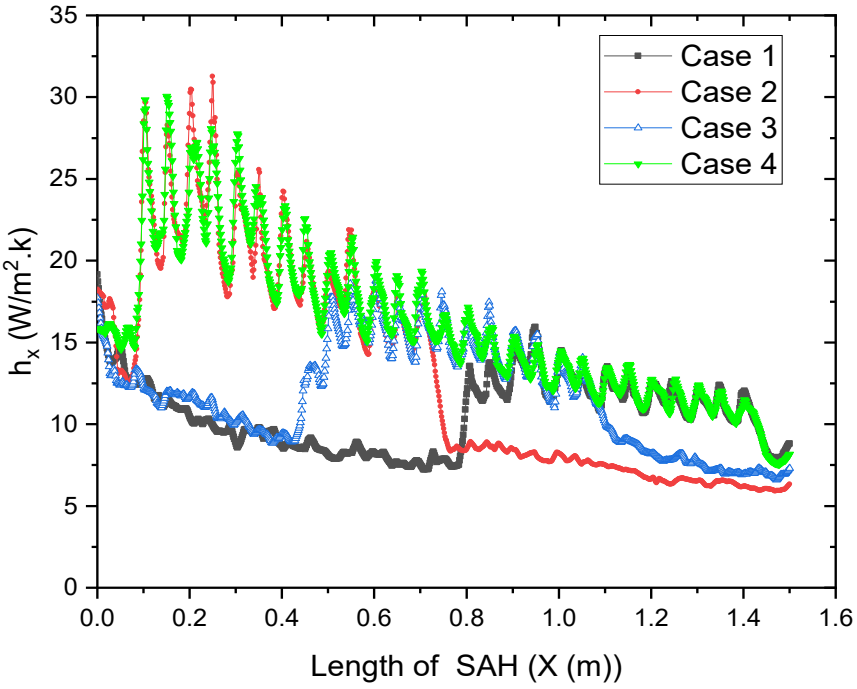


**Figure IV-8:** The local convective heat transfer coefficient versus the length of SAH for all baffled cases at Re=2370

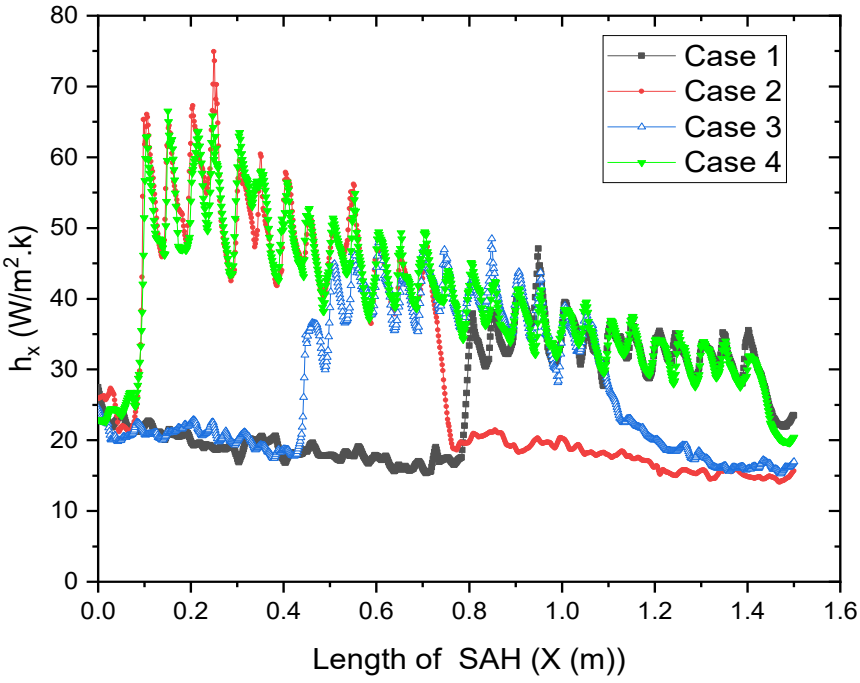


**Figure IV-9:** The local convective heat transfer coefficient versus the length of SAH for all baffled cases at Re=8340

## IV.4. ASSESSMENT OF THERMAL EFFICIENCY

In these simulations, heat flow has been imposed as a boundary condition on the upper surface, the absorber of the SAH. The heat flux on this surface is due, on the one hand, to absorbed solar radiation, and on the other, to heat losses by convection with the outside air and long-wave radiant exchange with the sky.

Regarding the lower surface of the SAH, the boundary condition assumes that the insulation material is such that heat losses are negligible. Therefore, the model used in the CFD simulations only considers heat losses on the upper surface. Based on the CFD results, thermal efficiency can be estimated from the following equations:

$$Q_{upper}+Q_{bottom}=\dot{m}C_p(T_{out}-T_{in}) \quad \text{(IV-1)}$$

$$Q_{upper}=I_T A_{abs}-Q_{losses} \quad \text{(IV-2)}$$

Where

$Q_{upper}$ and $Q_{bottom}$ are the net heat fluxes that go into the air in the chamber from the upper and bottom surfaces, respectively. These net values are considered for the calculation purpose of thermal efficiency as $Q_{bottom}=0\ W$, and $Q_{upper}=1000\ {}^{W}/_{m^2}\,.A_{abs}$.

These assumptions are based on typical values for summer midday solar irradiation in Biskra, for the upper heat flux, and considering that the bottom surface is well insulated.

An alternative expression for the thermal efficiency of the collector is calculated by the equation:

$$\eta_{th}=\frac{\dot{m}C_p(T_{out}-T_{in})}{I_T A_{abs}} \quad \text{(IV-3)}$$

The heat losses by convection to the outdoor air and the heat losses by long wave radiation to the sky can be calculated with the following expressions:

$$Q_{losses}=Q_{losses}^{convection}+Q_{losses}^{radiation} \quad \text{(IV-4)}$$

$$Q_{losses}^{convection}=A_{abs}\cdot h_c\left(T_{absorber}^{outer\ surface}-T_{air}^{outdoor}\right) \quad \text{(IV-5)}$$

$$Q_{losses}^{radiation}=A_{abs}\cdot h_r\left(T_{absorber}^{outer\ surface}-T_{sky}\right) \quad \text{(IV-6)}$$

Where $h_c$ is the average outdoor convective film coefficient and $h_r$ is the average outdoor radiative film coefficient. Typical values for these coefficients are [105]: $h_c=20\ {}^{W}/_{m^2K}$ and $h_r=5\ {}^{W}/_{m^2K}$.

In order to use the above expression, heat losses must be estimated previously. Figure IV-10 shows the electric equivalent model used for estimating heat losses.

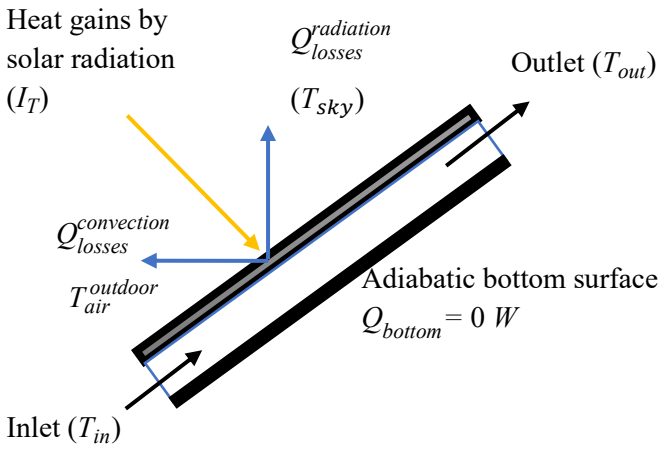


**Figure IV-10:** Schematic view for the estimation with heat gains and heat losses

On the other hand, the outdoor air temperature is equal to the inlet air temperature ($T_{air}^{outdoor}=T_{in}$) and the sky temperature can be estimated as a function of the outdoor air temperature using the following expression obtained by [106]:

$$T_{sky} = 0.0552 \cdot (T_{air}^{outdoor})^{1.5} \quad \text{(IV-7)}$$

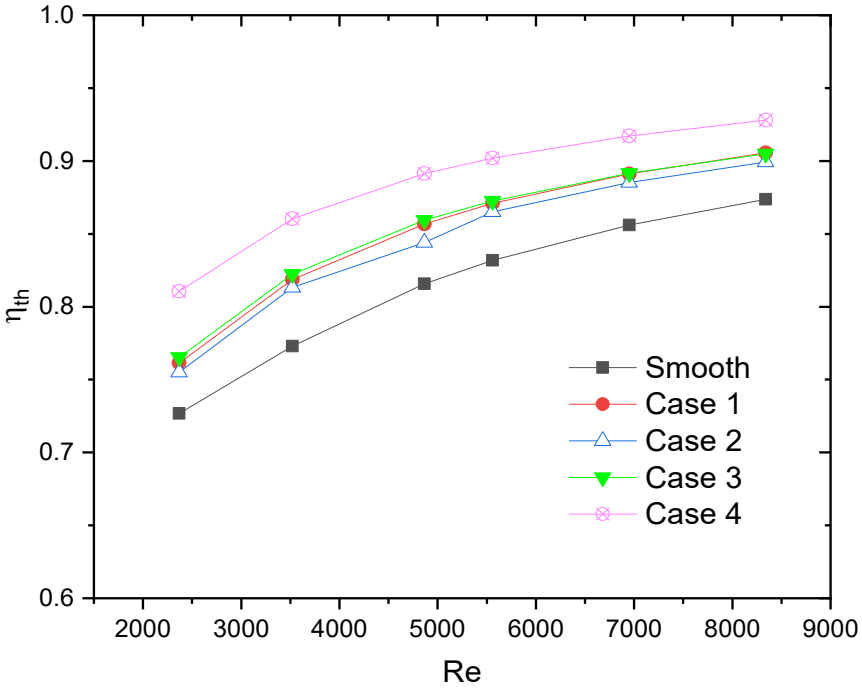


**Figure IV-11:** The estimated thermal efficiency versus the Reynolds number for each configuration

Figure IV-11 shows the thermal efficiency versus the Reynolds number for all the SAH cases. In each case, the thermal efficiency is higher for a larger Reynolds number. From this study, it can be concluded that thermal efficiency increases with the presence of baffles, especially for case 4 (100%). This is followed by case 1 (50%Up), case 3 (50%Middle), and case 2 (50%Down), consecutively, while the worst results correspond to the smooth configuration. This is a consequence of heat losses being higher for a higher surface temperature of the absorber.

## IV.5. ASSESSMENT OF FRICTION FACTOR

Figure IV-12 shows the variation of f versus Re for all the cases studied. The friction factor is seen to decrease with the increase in the Reynolds number, so they have an inverse relationship. Based on the graph, the curves tend slowly to a constant value.

The maximum friction factor was obtained for case 4 (100%), followed by the cases 1, 2 and 3 (50% Up, 50% Down and 50% Middle, respectively), which are almost identical, while the smooth channel has the minimum. This is due to the baffles and their position interfering with the fluid flow and giving rise to a higher pressure drop and hence friction factor. The predicted results of friction factor are compared with the experimental data of Lanjewar et al [28] for a smooth case.

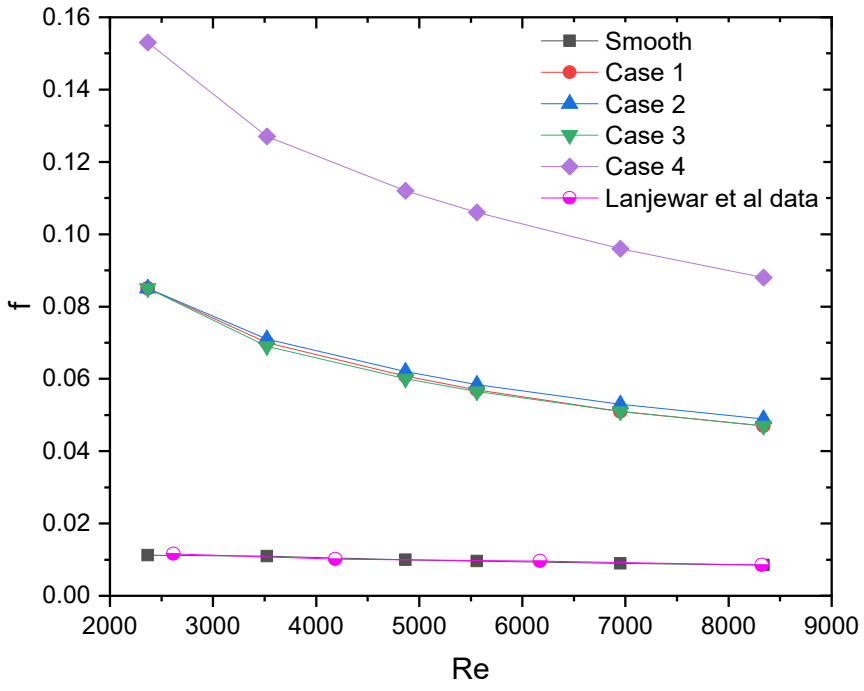


**Figure IV-12:** Variation of friction factor with Reynolds number for all cases

## IV.6. ASSESSMENT OF THE THERMO-HYDRAULIC PERFORMANCE FACTOR

The thermo-hydraulic performance is an essential factor to evaluate to determine the case that will result in the maximum enhancement in heat transfer and minimum increase in friction factor.

Figure IV-13 illustrates the thermo-hydraulic performance factor (THPF) for all the baffled cases. For case 1 (50%Up), THPF varies from 0.48 to 0.60, the highest value at the Reynolds number of 2370. Meanwhile, for case 2 (50% Down), THPF changes from 0.60 to 0.75, the highest value being at Re= 2370. The THPF of case 3 (50% Middle) ranges from 0.53 to 0.66, then in case 4 (100%) the THPF is between 0.59 and 0.70.

The graphic presentation shows that the results predicted by CFD are within the practical domain [57]. The thermo-hydraulic performance factors are less than unity for all studied cases, as shown in Figure IV-13. This is due to the increase in the friction factor outweighing that of heat transfer. Case 2 (50%Down) has the biggest thermo-hydraulic performance factor values, the maximum value being 0.75 at the Reynolds number value of 2370.

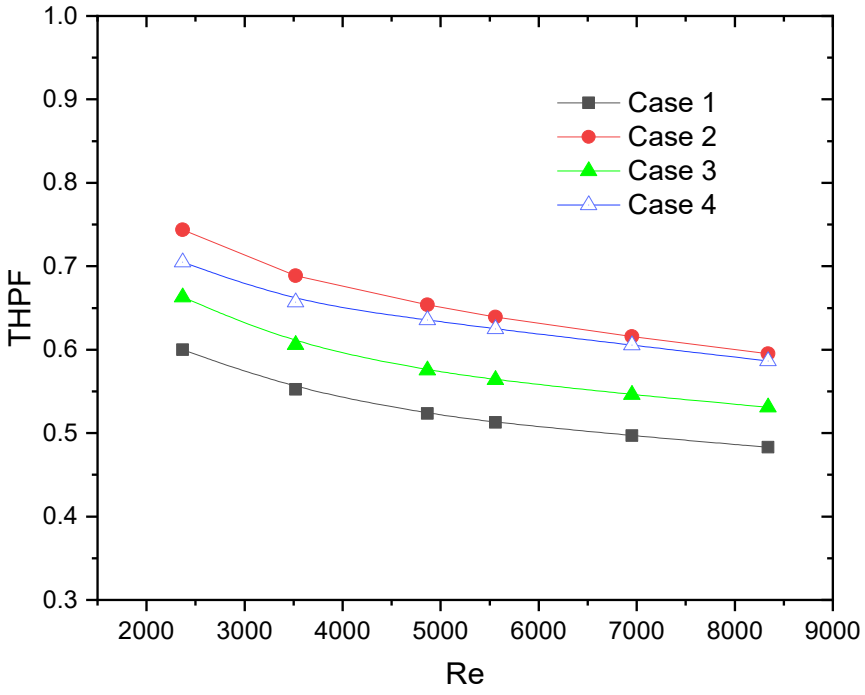


**Figure IV-13:** Thermo-hydraulic performance factor variation with Reynolds number for all the studied cases

## IV.7. CONCLUSION

An experimental campaign was used to validate the numerical CFD simulation. Then, new CFD simulations were carried out to determine the best configuration in terms of thermal and hydraulic performance. The effect of different baffle placements on local convective heat transfer coefficient, Nusselt number and friction factor has been evaluated. The current study aims to compare different baffle positions on the bottom plate of solar air heaters, the comparison has been done in addition to the conventional channel (smooth) for four different cases with baffles : 50%Up, 50%Down, 50%Middle and 100%. So, from current results we can conclude the following points:

- The maximum Nusselt number was obtained from case 4 (100% baffled case).
- The local convective heat transfer coefficient for a smooth channel at each Reynolds number increases at the beginning of the air channel; then, the initial vortex brings colder fluid into the air duct and it decreases slowly until the end.
- Thermal efficiency can be estimated based on heat losses by convection with the outside air and long-wave radiant exchange with the sky.
- The minimum friction factor value was obtained in cases 1, 2 and 3, these being almost equal.
- Case 2 (50%Down) has been selected as the best configuration and an effective baffle position from the point of view of thermo-hydraulic performance.

# *GENERAL CONCLUSION*

# GENERAL CONCLUSION

Based on the review of research into the optimization of the performance of solar air heaters, the major categories of the artificial roughness to improve the solar air heaters performances are the ribs and the baffles where each category has many classifications based on the shapes, sizes, orientations and arrangements. Judging from previous studies, it is evident that insufficient research has been performed into the placement of baffles on the bottom plate within the air channel of solar air heaters.

The current research study includes a 3D numerical simulation based an experimental validation to evaluate the performance of cases with different baffle positions, the examened cases are five cases including conventional case (smooth), Case 1 "baffles positioned in the second half of the air channel (50% Up)", Case 2 "baffles positioned in the first half of the air channel (50% Down)", Case 3" baffles positioned in the middle of the air channel (50% Middle)", Case 4" baffles positioned in all the air channel (100%)" and the baffles type construction and fabrication have been presented.

In the experimental part, the test device was a solar air heater (SAH) with a single pass designed and manufactured from locally available materials at the technological hall in Mohamed Khider University of Biskra, Algeria, whose latitude is 34°48'N and longitude 5°44'E. The experiments were performed during the period from 29/05/18 to 09/06/18 where the readings were made on very sunny days with sometimes cloudy periods, the test data of the SAHs were recorded every 30 min, the tests starting at 9 am and ending at 3 pm.

The CFD simulation has been prepared in the Laboratory of Mechanical Engineering (LGM), University Mohamed Khider of Biskra, Biskra, Algeria, and it has been done in the Department of Thermal Machines and Engines, University of Cadiz, Puerto Real, Spain. The CFD simulations were carried out to determine the best configuration in terms of thermal and hydraulic performance, where the creation of the the solar air heater (SAH) geometry and the mesh generation of the computational domain mesh have been done by GAMBIT 2.4.6. The mesh independency test was carried out for the case Re = 2354 by comparing seven different numbers of cells in order to eliminate the effect on the numerical computation results in terms of outlet air temperature and the average heat transfer coefficient.

The CFD simulations have been performed by ANSYS FLUENT 15.0 to assess the influence of different positions of the baffles on the thermo-hydraulic performance under assumptions and different boundary conditions were used the heat flux imposed on the absorber plate, inlet air temperature and adiabatic conditions at the bottom plate and side walls. The five known classical turbulence k-ε models including standard k-ε, RNG k-ε, realizable k-ε and k-ω models have been used in this evaluation, where

based on the CFD analysis, the RNG k-ε turbulence model was chosen for the reason of qualitative agreement and a good concordance with Dittus-Boelter and Modified Blasius correlations.

The air temperature along the x-direction in the air channel of the solar air heater obtained by the proposed CFD method and the results determined experimentally have been compered, thus, a good agreement has been achieved between each other. The effect of different baffle placements on local convective heat transfer coefficient, Nusselt number and friction factor has been evaluated, we can summarize the conclusions in the following points:

- The maximum Nusselt number was obtained from case 4 (100% baffled case).
- The local convective heat transfer coefficient for a smooth channel at each Reynolds number increases at the beginning of the air channel; then, the initial vortex brings colder fluid into the air duct and it decreases slowly until the end.
- The local convective heat transfer coefficient has three different behaviours in the case of the baffled air channel: first, upstream of the baffled section, peaks can be seen with a small amplitude corresponding to a low local convective heat transfer coefficient due to the reversed flow of the first baffle and the flow regime; second, peaks with a large amplitude in the baffled part corresponding to a huge local convective heat transfer coefficient due to the great vortexes; lastly, downstream of the baffled section, peaks are observed with a smaller amplitude than upstream due to the flow regime.
- The minimum friction factor value was obtained in cases 1, 2 and 3, these being almost equal.
- Decreases in the friction factor with increases in the Reynolds number was observed in all the cases studied.
- Although the highest Nusselt number value obtained was 70 in case 4 (Re = 8340), it produces a great pressure drop, while the lowest friction factor values were found to be 0.05 for cases 1, 2 and 3, with nearly identical values (Re = 8340).

Thermal efficiency has been estimated based on heat losses by convection with the outside air and long-wave radiant exchange with the sky, it is higher for a larger Reynolds number, leading to the conclusion that efficiency increases with the presence of baffles, as expected in case 4 (100% baffled case).

The thermo-hydraulic performance is an essential factor to evaluate to determine the case that will result in the maximum enhancement in heat transfer and minimum increase in friction factor, from the point of view of thermo-hydraulic performance, Case 2 (50%Down) has been selected as the best configuration and an effective baffle position from the point of view of thermo-hydraulic performance.

In future research, we intend to use a new baffles configuration in the selected case by change of the size, shape, orientation and attached the baffles on the absorber surface in the selected position of current study as well, that to determine the most suitable parameters.

# *REFERENCES*

# REFERENCES


[1] J.W. Twldell, W.B. Gillett, JS Hsieh. Solar Energy Engineering. Prentice-Hall, Inc. Englewood Cliffs, New Jersey (1986). ISBN 0-I 3-822446-3 A comprehensive introductory text to solar, (n.d.).

[2] J.A. Duffie, W.A. Beckman, Solar engineering of thermal processes, Fourth Edi, John Wiley & Sons, New York, 2013.

[3] S.P. Sukhatme, J.K. Nayak, Solar energy, McGraw-Hill Education, 2017.

[4] H.P. Garg, Solar energy: fundamentals and applications, Tata McGraw-Hill Education, 2000.

[5] D.J. Close, Solar air heaters for low and moderate temperature applications, Solar Energy. 7 (1963) 117–124.

[6] S.A. Kalogirou, Solar thermal collectors and applications, Progress in Energy and Combustion Science. 30 (2004) 231–295.

[7] K. Bin Sopian, M. Sohif, M. Alghoul, Output air temperature prediction in a solar air heater integrated with phase change material, European Journal of Scientific Research. 27 (2009) 334–341.

[8] A. Gupta, M. Uniyal, Review of heat transfer augmentation through different passive intensifier methods, IOSR Journal of Mechanical and Civil Engineering (IOSRJMCE) ISSN. (2012) 1684–2278.

[9] A.E. Bergles, ExHFT for fourth generation heat transfer technology, Experimental Thermal and Fluid Science. 26 (2002) 335–344.

[10] M.O. Garg, H. Nautiyal, S. Khurana, M.K. Shukla, Heat transfer augmentation using twisted tape inserts: A review, Renewable and Sustainable Energy Reviews. 63 (2016) 193–225.

[11] J.P. Joule, On the surface-condensation of steam, Journal of the Franklin Institute. 73 (1862) 113–114.

[12] B.N. Prasad, J.S. Saini, Optimal thermohydraulic performance of artificially roughened solar air heaters, Solar Energy. 47 (1991) 91–96.

[13] K. Prasad, S.C. Mullick, Heat transfer characteristics of a solar air heater used for drying purposes, Applied Energy. 13 (1983) 83–93. doi:10.1016/0306-2619(83)90001-6.

[14] B.N. Prasad, J.S. Saini, Effect of artificial roughness on heat transfer and friction factor in a solar air heater, Solar Energy. 41 (1988) 555–560. doi:10.1016/0038-092X(88)90058-8.

[15] D. Gupta, S.C. Solanki, J.S. Saini, Heat and fluid flow in rectangular solar air heater ducts having transverse rib roughness on absorber plates, Solar Energy. 51 (1993) 31–37.

[16] S.K. Verma, B.N. Prasad, Investigation for the optimal thermohydraulic performance of artificially roughened solar air heaters, Renewable Energy. 20 (2000) 19–36. doi:10.1016/S0960-1481(99)00081-6.

[17] M.M. Sahu, J.L. Bhagoria, Augmentation of heat transfer coefficient by using 90° broken transverse ribs on absorber plate of solar air heater, Renewable Energy. 30 (2005) 2057–2073. doi:10.1016/j.renene.2004.10.016.

# REFERENCES


[18] D. Gupta, S.C. Solanki, J.S. Saini, Thermohydraulic performance of solar air heaters with roughened absorber plates, Solar Energy. 61 (1997) 33–42.

[19] K.R. Aharwal, B.K. Gandhi, J.S. Saini, Experimental investigation on heat-transfer enhancement due to a gap in an inclined continuous rib arrangement in a rectangular duct of solar air heater, Renewable Energy. 33 (2008) 585–596.

[20] R.P. Saini, J.S. Saini, Heat transfer and friction factor correlations for artificially roughened ducts with expanded metal mesh as roughness element, International Journal of Heat and Mass Transfer. 40 (1997) 973–986.

[21] S. V. Karmare, A.N. Tikekar, Heat transfer and friction factor correlation for artificially roughened duct with metal grit ribs, International Journal of Heat and Mass Transfer. 50 (2007) 4342–4351. doi:10.1016/j.ijheatmasstransfer.2007.01.065.

[22] A.-M.E. Momin, J.S. Saini, S.C. Solanki, Heat transfer and friction in solar air heater duct with V-shaped rib roughness on absorber plate, International Journal of Heat and Mass Transfer. 45 (2002) 3383–3396.

[23] R. Karwa, B.K. Maheshwari, N. Karwa, Experimental study of heat transfer enhancement in an asymmetrically heated rectangular duct with perforated baffles, International Communications in Heat and Mass Transfer. 32 (2005) 275–284. doi:10.1016/j.icheatmasstransfer.2004.10.002.

[24] R. Karwa, Experimental studies of augmented heat transfer and friction in asymmetrically heated rectangular ducts with ribs on the heated wall in transverse, inclined, v-continuous and v-discrete pattern, International Communications in Heat and Mass Transfer. 30 (2003) 241–250.

[25] V.S. Hans, R.P. Saini, J.S. Saini, Heat transfer and friction factor correlations for a solar air heater duct roughened artificially with multiple v-ribs, Solar Energy. 84 (2010) 898–911.

[26] A. Kumar, R.P. Saini, J.S. Saini, Experimental investigation on heat transfer and fluid flow characteristics of air flow in a rectangular duct with Multi v-shaped rib with gap roughness on the heated plate, Solar Energy. 86 (2012) 1733–1749. doi:10.1016/j.solener.2012.03.014.

[27] A.M. Lanjewar, J.L. Bhagoria, R.M. Sarviya, Performance analysis of W-shaped rib roughened solar air heater, Journal of Renewable and Sustainable Energy. 3 (2011) 43110.

[28] A. Lanjewar, J.L. Bhagoria, R.M. Sarviya, Heat transfer and friction in solar air heater duct with W-shaped rib roughness on absorber plate, Energy. 36 (2011) 4531–4541. doi:10.1016/j.energy.2011.03.054.

[29] A. Lanjewar, J.L. Bhagoria, R.M. Sarviya, Experimental study of augmented heat transfer and friction in solar air heater with different orientations of W-Rib roughness, Experimental Thermal and Fluid Science. 35 (2011) 986–995. doi:10.1016/j.expthermflusci.2011.01.019.

[30] A. Kumar, J.L. Bhagoria, R.M. Sarviya, Heat transfer and friction correlations for artificially roughened solar air heater duct with discrete W-shaped ribs, Energy

Conversion and Management. 50 (2009) 2106–2117. doi:10.1016/j.enconman.2009.01.025.

[31] S.K. Saini, R.P. Saini, Development of correlations for Nusselt number and friction factor for solar air heater with roughened duct having arc-shaped wire as artificial roughness, Solar Energy. 82 (2008) 1118–1130. doi:10.1016/j.solener.2008.05.010.

[32] S. Kumar, R.P. Saini, CFD based performance analysis of a solar air heater duct provided with artificial roughness, Renewable Energy. 34 (2009) 1285–1291. doi:10.1016/j.renene.2008.09.015.

[33] A.P. Singh, Heat transfer and friction factor correlations for multiple arc shape roughness elements on the absorber plate used in solar air heaters, Experimental Thermal and Fluid Science. 54 (2014) 117–126.

[34] A.P. Singh, Effect of artificial roughness on heat transfer and friction characteristics having multiple arc shaped roughness element on the absorber plate, Solar Energy. 105 (2014) 479–493.

[35] M.K. Sahu, R.K. Prasad, Exergy based performance evaluation of solar air heater with arc-shaped wire roughened absorber plate, Renewable Energy. 96 (2016) 233–243. doi:10.1016/J.RENENE.2016.04.083.

[36] N.K. Pandey, V.K. Bajpai, Experimental investigation of heat transfer and friction characteristics of arc-shaped roughness elements having central gaps on the absorber plate of solar air heater, Journal of Solar Energy Engineering. 138 (2016).

[37] R.S. Gill, V.S. Hans, J.S. Saini, S. Singh, Investigation on performance enhancement due to staggered piece in a broken arc rib roughened solar air heater duct, Renewable Energy. 104 (2017) 148–162.

[38] R.S. Gill, V.S. Hans, S. Singh, Investigations on thermo-hydraulic performance of broken arc rib in a rectangular duct of solar air heater, International Communications in Heat and Mass Transfer. 88 (2017) 20–27.

[39] R. Karwa, S.C. Solanki, J.S. Saini, Heat transfer coefficient and friction factor correlations for the transitional flow regime in rib-roughened rectangular ducts, International Journal of Heat and Mass Transfer. 42 (1999) 1597–1615.

[40] J.L. Bhagoria, J.S. Saini, S.C. Solanki, Heat transfer coefficient and friction factor correlations for rectangular solar air heater duct having transverse wedge shaped rib roughness on the absorber plate, Renewable Energy. 25 (2002) 341–369.

[41] R.P. Saini, J. Verma, Heat transfer and friction factor correlations for a duct having dimple-shape artificial roughness for solar air heaters, Energy. 33 (2008) 1277–1287. doi:10.1016/j.energy.2008.02.017.

[42] J.-M. Buchlin, Convective heat transfer in a channel with perforated ribs, International Journal of Thermal Sciences. 41 (2002) 332–340.

[43] C. Nuntadusit, M. Wae-hayee, A. Bunyajitradulya, S. Eiamsa-ard, Thermal visualization on surface with transverse perforated ribs, International Communications in Heat and Mass Transfer. 39 (2012) 634–639. doi:10.1016/j.icheatmasstransfer.2012.03.001.

# REFERENCES


[44] A.R. Jaurker, J.S. Saini, B.K. Gandhi, Heat transfer and friction characteristics of rectangular solar air heater duct using rib-grooved artificial roughness, Solar Energy. 80 (2006) 895–907.

[45] A. Layek, J.S. Saini, S.C. Solanki, Heat transfer and friction characteristics for artificially roughened ducts with compound turbulators, International Journal of Heat and Mass Transfer. 50 (2007) 4845–4854.

[46] Varun, R.P. Saini, S.K. Singal, Investigation of thermal performance of solar air heater having roughness elements as a combination of inclined and transverse ribs on the absorber plate, Renewable Energy. 33 (2008) 1398–1405. doi:10.1016/j.renene.2007.07.013.

[47] A.K. Patil, J.S. Saini, K. Kumar, Effect of gap position in broken V-rib roughness combined with staggered rib on thermohydraulic performance of solar air heater, Green. 1 (2011) 329–338.

[48] M. Sethi, N.S. Thakur, Varun, Heat transfer and friction characteristics of dimple-shaped roughness element arranged in angular fashion (arc) on the absorber plate of solar air heater, Journal of Renewable and Sustainable Energy. 4 (2012) 23112.

[49] M. Sethi, Varun, N.S. Thakur, Correlations for solar air heater duct with dimpled shape roughness elements on absorber plate, Solar Energy. 86 (2012) 2852–2861. doi:10.1016/j.solener.2012.06.024.

[50] A.K. Patil, J.S. Saini, K. Kumar, Nusselt number and friction factor correlations for solar air heater duct with broken V-down ribs combined with staggered rib roughness, Journal of Renewable and Sustainable Energy. 4 (2012) 33122.

[51] S. Yadav, M. Kaushal, Nusselt number and friction factor correlations for solar air heater duct having protrusions as roughness elements on absorber plate, Experimental Thermal and Fluid Science. 44 (2013) 34–41.

[52] S. Yadav, M. Kaushal, Exergetic performance evaluation of solar air heater having arc shape oriented protrusions as roughness element, Solar Energy. 105 (2014) 181–189.

[53] P. Biondi, L. Cicala, G. Farina, Performance analysis of solar air heaters of conventional design, Solar Energy. 41 (1988) 101–107.

[54] N. Moummi, S. Youcef-Ali, A. Moummi, J.Y. Desmons, Energy analysis of a solar air collector with rows of fins, Renewable Energy. 29 (2004) 2053–2064. doi:10.1016/j.renene.2003.11.006.

[55] P. Promvonge, W. Jedsadaratanachai, S. Kwankaomeng, Numerical study of laminar flow and heat transfer in square channel with 30 inline angled baffle turbulators, Applied Thermal Engineering. 30 (2010) 1292–1303.

[56] K. Aoues, N. Moummi, M. Zellouf, A. Benchabane, Thermal performance improvement of solar air flat plate collector: a theoretical analysis and an experimental study in Biskra, Algeria, International Journal of Ambient Energy. 32 (2011) 95–102.

[57] F. Menasria, M. Zedairia, A. Moummi, Numerical study of thermohydraulic performance of solar air heater duct equipped with novel continuous rectangular baffles with high

aspect ratio, Energy. 133 (2017) 593–608. doi:10.1016/j.energy.2017.05.002.

[58] A.L. Antony, S.P. Shetty, N. Madhwesh, N.Y. Sharma, K.V. Karanth, Influence of stepped cylindrical turbulence generators on the thermal enhancement factor of a flat plate solar air heater, Solar Energy. 198 (2020) 295–310.

[59] P. Promvonge, Heat transfer and pressure drop in a channel with multiple 60 V-baffles, International Communications in Heat and Mass Transfer. 37 (2010) 835–840.

[60] P. Promvonge, S. Kwankaomeng, Periodic laminar flow and heat transfer in a channel with 45° staggered V-baffles, International Communications in Heat and Mass Transfer. 37 (2010) 841–849. doi:10.1016/j.icheatmasstransfer.2010.04.002.

[61] P. Promvonge, W. Jedsadaratanachai, S. Kwankaomeng, C. Thianpong, 3D simulation of laminar flow and heat transfer in V-baffled square channel, International Communications in Heat and Mass Transfer. 39 (2012) 85–93.

[62] P. Sriromreun, C. Thianpong, P. Promvonge, Experimental and numerical study on heat transfer enhancement in a channel with Z-shaped baffles, International Communications in Heat and Mass Transfer. 39 (2012) 945–952. doi:10.1016/j.icheatmasstransfer.2012.05.016.

[63] Y.-T. Yang, C.-Z. Hwang, Calculation of turbulent flow and heat transfer in a porous-baffled channel, International Journal of Heat and Mass Transfer. 46 (2003) 771–780.

[64] R. Karwa, B.K. Maheshwari, Heat transfer and friction in an asymmetrically heated rectangular duct with half and fully perforated baffles at different pitches, International Communications in Heat and Mass Transfer. 36 (2009) 264–268.

[65] D. Sahel, H. Ameur, R. Benzeguir, Y. Kamla, Enhancement of heat transfer in a rectangular channel with perforated baffles, Applied Thermal Engineering. 101 (2016) 156–164.

[66] K. Yakut, B. Sahin, C. Celik, N. Alemdaroglu, A. Kurnuc, Effects of tapes with double-sided delta-winglets on heat and vortex characteristics, Applied Energy. 80 (2005) 77–95.

[67] I. Kotcioglu, S. Caliskan, A. Cansiz, S. Baskaya, Second law analysis and heat transfer in a cross-flow heat exchanger with a new winglet-type vortex generator, Energy. 35 (2010) 3686–3695.

[68] S. Sripattanapipat, P. Promvonge, Numerical analysis of laminar heat transfer in a channel with diamond-shaped baffles, International Communications in Heat and Mass Transfer. 36 (2009) 32–38. doi:10.1016/j.icheatmasstransfer.2008.09.008.

[69] A. Labed, N. Moummi, A. Benchabane, K.A.M. Zellouf, Performances thermiques et pertes de charges de différentes configurations de capteurs solaires plans à air Etude expérimentale dans la région de Biskra , Algérie, 18 (2015) 209–216.

[70] A. Abene, V. Dubois, M. Le Ray, A. Ouagued, Study of a solar air flat plate collector: use of obstacles and application for the drying of grape, Journal of Food Engineering. 65 (2004) 15–22.

[71] M.T. Baissi, A. Brima, K. Aoues, R. Khanniche, N. Moummi, Thermal behavior in a solar air heater channel roughened with delta-shaped vortex generators, Applied Thermal

Engineering. (2019). doi:10.1016/J.APPLTHERMALENG.2019.03.134.

[72] Y. Ho-Ming, C. Wen-Hsen, Efficiency of solar air heaters with baffles, Energy. 16 (1991) 983–987.

[73] H.-M. Yeh, C.-D. Ho, C.-Y. Lin, The influence of collector aspect ratio on the collector efficiency of baffled solar air heaters, Energy. 23 (1998) 11–16. doi:10.1016/S0360-5442(97)00054-6.

[74] C.-D. Ho, H. Chang, R.-C. Wang, C.-S. Lin, Performance improvement of a double-pass solar air heater with fins and baffles under recycling operation, Applied Energy. 100 (2012) 155–163.

[75] E.K. Akpinar, F. Koçyiğit, Experimental investigation of thermal performance of solar air heater having different obstacles on absorber plates, International Communications in Heat and Mass Transfer. 37 (2010) 416–421.

[76] J. Hu, G. Zhang, Performance improvement of solar air collector based on airflow reorganization: A review, Applied Thermal Engineering. 155 (2019) 592–611. doi:10.1016/J.APPLTHERMALENG.2019.04.021.

[77] H. Hottel, A. Whillier, Evaluation of flat-plate solar collector performance, in: Trans. Conf. Use of Solar Energy;(), 1955.

[78] R.W. Bliss Jr, The derivations of several "plate-efficiency factors" useful in the design of flat-plate solar heat collectors, Solar Energy. 3 (1959) 55–64.

[79] K. Frank, S.B. Mark, Principles of heat transfer Thomson Learning Inc, (2001).

[80] R.L. Webb, E.R.G. Eckert, Application of rough surfaces to heat exchanger design, International Journal of Heat and Mass Transfer. 15 (1972) 1647–1658.

[81] A. Standard, 93-77,"Methods of testing to determine the thermal performance of solar collectors," New York. (1977).

[82] H.K. Versteeg, W. Malalasekera, An introduction to computational fluid dynamics: the finite volume method, Pearson education, 2007.

[83] S. V Patankar, Numerical Heat Transfer and Fluid Flow (Series in Computational Methods in Mechanics and Thermal Sciences)(New York: Hemisphere/McGraw-Hill), (1980).

[84] A. Fluent, Ansys fluent theory guide, ANSYS Inc., USA. 15317 (2011) 724–746.

[85] B.E. Launder, D.B. Spalding, Mathematical models of turbulence, Academic press, 1972.

[86] T.-H. Shih, W.W. Liou, A. Shabbir, Z. Yang, J. Zhu, A new k-ϵ eddy viscosity model for high reynolds number turbulent flows, Computers & Fluids. 24 (1995) 227–238.

[87] S.A. Orszag, Renormalisation group modelling and turbulence simulations, Near-Wall Turbulent Flows. (1993).

[88] D.C. Wilcox, Turbulence modeling for CFD, DCW industries La Canada, CA, 1998.

[89] J. Wilcox, On the path to elucidating the speciation of mercury in the flue gases of coal combustion, (2004).

# REFERENCES


[90] N. Safer, M. Woloszyn, J.J. Roux, Three-dimensional simulation with a CFD tool of the airflow phenomena in single floor double-skin facade equipped with a venetian blind, Solar Energy. 79 (2005) 193–203.

[91] A. Singh Yadav, J.L. Bhagoria, Numerical investigation of flow through an artificially roughened solar air heater, International Journal of Ambient Energy. 36 (2015) 87–100. doi:10.1080/01430750.2013.823107.

[92] H. Transmission, by WH McAdams, McGraw-Hill Book Co., New York. 214 (1942).

[93] R.W. Fox, A.T. McDonald, P.J. Pritchard, Introduction to fluid mechanics. 5th, (2010).

[94] A.S. Yadav, J.L. Bhagoria, A CFD (computational fluid dynamics) based heat transfer and fluid flow analysis of a solar air heater provided with circular transverse wire rib roughness on the absorber plate, Energy. 55 (2013) 1127–1142. doi:10.1016/j.energy.2013.03.066.

[95] A.S. Yadav, J.L. Bhagoria, Heat transfer and fluid flow analysis of solar air heater: A review of CFD approach, Renewable and Sustainable Energy Reviews. 23 (2013) 60–79. doi:10.1016/J.RSER.2013.02.035.

[96] A.S. Yadav, J.L. Bhagoria, A numerical investigation of square sectioned transverse rib roughened solar air heater, International Journal of Thermal Sciences. 79 (2014) 111–131.

[97] A.S. Yadav, J.L. Bhagoria, A CFD based thermo-hydraulic performance analysis of an artificially roughened solar air heater having equilateral triangular sectioned rib roughness on the absorber plate, International Journal of Heat and Mass Transfer. 70 (2014) 1016–1039.

[98] A. Kumar, M.-H. Kim, CFD Analysis on the Thermal Hydraulic Performance of an SAH Duct with Multi V-Shape Roughened Ribs, Energies. 9 (2016) 415. doi:10.3390/en9060415.

[99] D. Jin, M. Zhang, P. Wang, S. Xu, Numerical investigation of heat transfer and fluid flow in a solar air heater duct with multi V-shaped ribs on the absorber plate, Energy. 89 (2015) 178–190.

[100] S. V. Karmare, A.N. Tikekar, Analysis of fluid flow and heat transfer in a rib grit roughened surface solar air heater using CFD, Solar Energy. 84 (2010) 409–417. doi:10.1016/j.solener.2009.12.011.

[101] V.B. Gawande, A.S. Dhoble, D.B. Zodpe, S. Chamoli, A review of CFD methodology used in literature for predicting thermo-hydraulic performance of a roughened solar air heater, Renewable and Sustainable Energy Reviews. (2016). doi:10.1016/j.rser.2015.10.025.

[102] V.B. Gawande, A.S. Dhoble, D.B. Zodpe, S. Chamoli, Experimental and CFD investigation of convection heat transfer in solar air heater with reverse L-shaped ribs, Solar Energy. (2016). doi:10.1016/j.solener.2016.02.040.

[103] F.P. Incropera, A.S. Lavine, T.L. Bergman, D.P. DeWitt, Fundamentals of heat and mass transfer, Wiley, 2007.

[104] A. Cortés, R. Piacentini, Improvement of the efficiency of a bare solar collector by means

of turbulence promoters, Applied Energy. 36 (1990) 253–261. doi:10.1016/0306-2619(90)90001-T.

[105] E.C. for Standardization, EN ISO 6946-2007, Building Components and Building Elements, Thermal Resistance and Thermal Transmittance, Calculation Method: December 2007, European Committee for Standardization, 2007.

[106] W.C. Swinbank, Long-wave radiation from clear skies, Quarterly Journal of the Royal Meteorological Society. 89 (1963) 339–348.

# APPENDICES

Renewable Energy 155 (2020) 1231–1244

Contents lists available at ScienceDirect

Renewable Energy

journal homepage: www.elsevier.com/locate/renene

# Numerical and experimental study of the heat transfer and hydraulic performance of solar air heaters with different baffle positions

Charaf-Eddine Bensaci [a, b, *], Abdelhafid Moummi [a, b], Francisco J. Sanchez de la Flor [c], Enrique A. Rodriguez Jara [c], Alejandro Rincon-Casado [d], Alvaro Ruiz-Pardo [c]

[a] Laboratory of Mechanical Engineering (LGM), University Mohamed Khider of Biskra, B.P. 145, RP 07000, Biskra, Algeria
[b] Laboratory of Civil Engineering, Hydraulics, Sustainable Development and Environment (LAR-GHYDE), University Mohamed Khider of Biskra, B.P. 145, R.P. 07000, Biskra, Algeria
[c] Department of Thermal Machines and Engines, University of Cadiz, 11519, Puerto Real, Spain
[d] Department of Mechanical Engineering and Industrial Design, University of Cadiz, 11519, Puerto Real, Spain

ARTICLE INFO

*Article history:*
Received 24 November 2019
Received in revised form
20 March 2020
Accepted 2 April 2020
Available online 14 April 2020

*Keywords:*
Solar air heater
Baffles
CFD simulation
Thermo-hydraulic performance
Local convective heat transfer coefficient

ABSTRACT

This study presents the results of a numerical and experimental study of the position of the baffles in a solar air heater in order to improve its thermal and hydraulic performance. The numerical study was performed on four cases corresponding to different placements of baffles with Reynolds numbers ranging from 2370 to 8340. The experimental model of the solar air heater was designed, manufactured and used for the validation of the numerical model. The new baffle placements show that effective thermo-hydraulic performance is not just a function of the shape or changes in the geometric parameters of the baffles. The correct placement of baffles dramatically improves the thermo-hydraulic performance of solar air heaters. The effect of baffle positions on local convective heat transfer coefficients has been discussed. The optimum thermo-hydraulic performance factor is achieved in the case where the baffles are located in the first part of air channel which occupies 50% of the solar air heater.



## 1. Introduction

The basic ingredient for sustaining life and development is energy in its different forms. Solar energy is a clean, eco-friendly source of energy that is freely available in the long term. The most efficient and simplest way to benefit from solar energy, with no negative effects, is for collectors to convert it into thermal energy for a variety of applications [1,2]. There is a wide scope for using the available solar energy for thermal applications such as solar drying, crop drying, water heating, building heating and solar cooking [3–5]. Solar air collectors (SAC) are the most common type of collector due to their enhanced capacity to absorb both diffuse and direct radiation simultaneously, in addition to being easy to maintain, reliable and easy to install in buildings. However, the efficiency of this system is low because of the low convective heat transfer coefficient between the absorber plate and the flowing air. However, there are many ways to increase this, such as by using air impinging jets, replacing the single duct with double-pass or multipass ones and incorporating baffles, which has been reported and proposed in the literature. Prasad and Mullick [6] first introduced the concept of artificial roughness to improve the thermal performance of SACs for drying purposes. The later studies of Prasad and Saini [7] confirmed that artificially roughened SACs present an enhanced rate of heat transfer compared with smooth SACs under the same operating conditions of mass flow rate and intensity of solar radiation. Burgess et al. [8] conducted an experimental study to investigate the effects of dimple depth (e) on heat transfer enhancement, finding increases in the local Nusselt number as the dimple depth increased. Saini and Verma [9] carried out experimental research into the fluid flow and heat transfer characteristics of SAC ducts having dimple-shaped artificial roughness. Furthermore, a lot of experimental studies have been performed into the thermal-hydraulic performance of solar air heater (SAH) ducts with different levels of artificial roughness [10–14]. In recent years, research has been performed into the effect on convective heat transfer of baffled systems, which improve thermal performance. Patankar et al. [15] reported the first numerical study of forced-convection heat transfer in periodically varying cross-

* Corresponding author. Laboratory of Mechanical Engineering (LGM), University Mohamed Khider of Biskra, B.P. 145, RP 07000, Biskra, Algeria.
*E-mail address:* charafbensaci@gmail.com (C.-E. Bensaci).

https://doi.org/10.1016/j.renene.2020.04.017
0960-1481/